Three-dimensional Device Structures for Photovoltaic Applications

Henning Urban

A thesis submitted in partial fulfillment of the requirements for
the degree of Doctor of Philosophy at the University of Oxford.

Clarendon Laboratory
Department of Physics
University of Oxford

Oxford, Trinity Term 2012

Three-dimensional Device Structures for Photovoltaic Applications

Henning Urban

University College, Oxford, Trinity Term 2012

Thesis submitted for the degree of Doctor of Philosophy at the University of Oxford.

Abstract

Harnessing solar energy has become a promising clean and renewable energy source alternative to fossil fuels since the development of low-cost dye sensitized solar cells (DSSC) and organic photovoltaic solar cell devices. Their power-conversion efficiencies, below 13% and 9% respectively, still limit the economic viability of these technologies. The geometry and optical properties of photonic crystals can be used to improve the absorption and charge collection efficiencies of these devices. This thesis describes the fabrication of TiO_2 DSSC and ZnO-polymer solar cell devices based on a three-dimensional photonic crystal structure. Photonic crystal polymer structures were produced by holographic lithography and thermally stabilized in order to be used as templates for atomic layer deposition (ALD) of various metal oxides. For this purpose, an ALD apparatus was built and ALD processes for the growth of TiO_2, ZnO, Al_2O_3, ZnO:Al, and Zr_3N_4 were established and deposited on photonic crystal templates. After ALD, the template was removed by calcination at 500°C, at which ZnO:Al films lost their conductivity of 250 S/cm preventing their use as transparent conducting oxide (TCO) electrodes. The produced 90 nm TiO_2 photonic crystal shell DSSC and TiO_2 inverse replica devices based on the dye N-719 and I^-/I_3^- electrolyte provided power-conversion efficiencies of 0.9% and 0.49% respectively and their diffusion lengths were 2× and 3× longer than that of a nanocrystalline reference device respectively. ZnO-polymer devices, comprising a P3HT layer as absorber and PEDOT:PSS film as hole-transporter, were also investigated.

Contents

1 Introduction

The total annual world power demand of human civilization is currently 16 TW [1], of which 81% is provided by fossil fuels [2]. Neglecting the continuous growth of global power demand, fossil fuel reserves would be sufficient to meet only 54, 64, and 112 years of global production of oil, natural gas, and coal respectively [1]. Thus, in order to progress, our civilization requires renewable energy sources.

The sun provides earth with as much energy every hour as civilization uses each year [3]. Solar energy is perpetual and non-polluting, and consequently an attractive, alternative energy source to fossil fuels. Technologies such as concentrating solar thermal power and solar photovoltaics have been developed in order to exploit solar energy by transforming it into heat and electrical energy respectively. However, the present global power capacity of both technologies, 1.8 and 70 GW respectively [2], is still far from meeting global energy demand. This is mainly because of their incapability of competing with the the cost of conventional grid electricity [3]. Solar photovoltaic cell devices in particular offer great prospects to become economically viable due to their potential for decentralized energy generation and low-cost manufacture by processes such as high-throughput roll-to-roll processing. The feasibility of this type of processing results from the use of soluble molecules and conjugated polymers in the device. Despite the processability and low cost of these materials, their large band-gaps, limited charge carrier mobilities, and indirect conduction pathways still limit device performance. As a consequence, in order to reach their full potential these low-cost solar cell technologies need to become more efficient in converting sunlight to electricity by increasing their absorption and charge collection efficiencies. These factors can be controlled either by material design, optimizing the device geometry, or by moulding the flow of light in the device.

The aim of this thesis is to develop a solar cell device, with a new geometry that provides direct conduction pathways, using existing photovoltaic materials that allow high-throughput manufacture. The proposed device geometry has the form of a three-dimensional photonic crystal structure. Photonic crystals are composite materials embodying a periodically modulated refractive index distribution with a periodicity comparable to the wavelength of light [4]. The refractive index distribution of photonic crystals determines their optical properties including transmission, reflection, diffraction, group velocity, and localization of the incident light. Hence photonic crystals have the potential to control the light distribution in a solar cell device in order to increase light-matter interactions and thus increase effective optical absorption path lengths. The proposed photonic crystal geometry can potentially increase the power-conversion efficiency of a solar cell device by reducing the lengths of its conduction pathways and simultaneously improving its absorption by photonic design. However, even though the device targeted in this thesis is named a photonic crystal solar cell, its photonic properties have not been optimized to increase the absorption or power-conversion efficiency as outlined above. Instead this work intends to show the feasibility of the technique holographic lithography to create such a device on an industrial scale. This thesis shall therefore lay the groundwork for a photonic crystal solar cell device that can potentially be designed with an increased optical path length or minimized radiative recombination losses.

The thesis is structured as follows. The following chapter introduces the optical properties and possible applications of photonic crystals, the basic designs and limitations of existing types of solar cell devices, and different strategies for increasing the power-conversion efficiency of solar cell devices using photonic crystals (Chapter 2). The chapter concludes with a scheme of the proposed solar cell device and a plan to realize it. The project plan involves the fabrication of photonic crystal polymer structures by holographic lithography and their use as templates for the growth of metal oxide films by atomic layer deposition (ALD). For this purpose the holographic lithography technique was modified to produce more uniform and thermally stable polymer templates (Chapter 3). Chapter 4 demonstrates the construction of an ALD apparatus, the completion and characterization of the necessary ALD processes, and use for deposition on photonic crystal polymer templates. The resulting metal oxide photonic crystal structures were implemented in solar cell devices. The fabrication processes and characterization of these photonic crystal solar cell devices are described in Chapter 5. The last chapter summarizes the produced solar cell devices and their characteristics, explains the deviations from the proposed device, and presents ideas for future work (Chapter 6).

2 Photonic Crystal Solar Cells

2.1 Solar Cells

In 1839, nineteen year old Edmund Becquerel immersed a silver coated platinum electrode in an electrolyte under illumination with visible light and detected an electric current—he discovered the photovoltaic effect [5]. The same effect occurs in a solar cell which is a photovoltaic semiconductor device that converts light energy (from the sun) into electrical energy. For this purpose the device absorbs photons and produces electrons and holes. In order to perform work in an electrical load the charge carriers need to be separated and driven out of the device along different paths to separate terminals by an internal force. The general mechanism of a solar cell device will be explained in the following section, then different established device structures will be introduced and their limitations discussed.

2.1.1 General Mechanism of a Solar Cell Device

A solar cell device is a structure in which illumination produces an electrical current of electrons and holes, along with an electrical voltage at its terminals [6; 7]. Its mechanism is best illustrated on a heterojunction that comprises an absorbing material sandwiched between an n-type semiconductor (left) and a p-type semiconductor (right) with larger energy band-gaps (E_{g}) and electron affinities (χ_{e}) (see Figure 2.1 a on the following page). The absorber produces electron-hole pairs under illumination which are separated by the n-conductor and p-conductor. The reason that n-type and p-type conductors are permeable to majority carriers but impermeable to minority carriers is

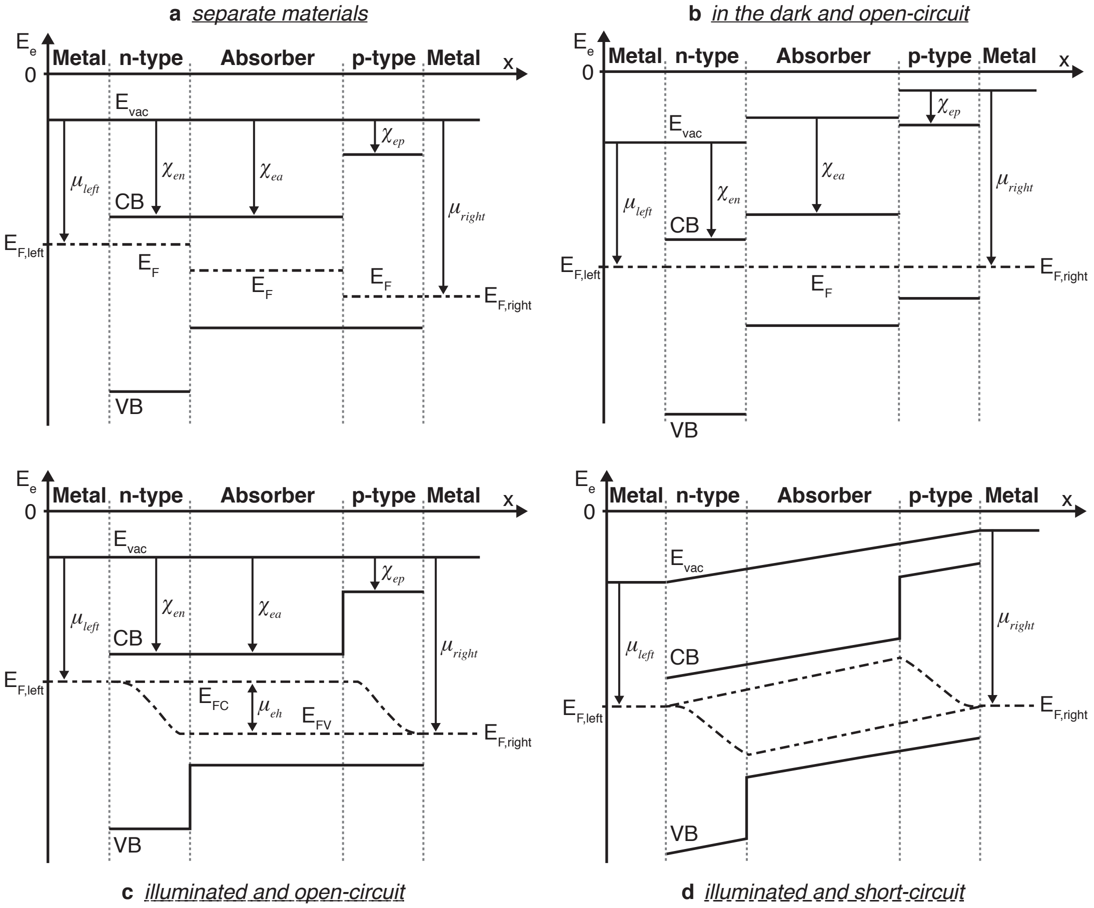

a *separate materials*

b *in the dark and open-circuit*

c *illuminated and open-circuit*

d *illuminated and short-circuit*

Figure 2.1: Conduction bands (CB), valence bands (VB), Fermi levels (E_F), and vacuum energy ($E_\mathrm{vac} = -e\phi$, where ϕ electrical potential) of absorbing, n-type, and p-type semiconductors used in a heterojunction solar cell device (**a**). Electron affinities (χ_e) and band-gaps of n and p-conductors are different from the absorber. Metal contacts with Fermi levels $E_\mathrm{F,left}$ and $E_\mathrm{F,right}$ and work functions μ_left and μ_right serve as terminals. Band diagram of the same device disconnected from an external load (open-circuit) in the dark where Fermi levels merge at E_F (**b**). Under illumination (assuming homogeneous intensity distribution in absorber) the Fermi energies of electrons (E_FC) and holes (E_FV) emerge (**c**). The resulting chemical energy per electron-hole pair $\mu_\mathrm{eh} = E_\mathrm{FC} - E_\mathrm{FV}$ is the maximum energy that the device can utilize per absorbed photon in order to perform electrical work in the external load. (**d**) shows band diagram of the illuminated solar cell device but at short-circuit condition $E_\mathrm{F,left} = E_\mathrm{F,right}$.

that they provide a large conductivity for majority carriers and a small conductivity for minority carriers. The larger band-gap of n and p-conductor compared with the absorber ensures that photons can reach the absorber and that the conductivity of minority carriers is further reduced. In the dark the magnitude of the electro-chemical potential for electrons in a semiconductor, $\eta_\mathrm{e} = \mu_\mathrm{e} - e\phi$, equals the electro-chemical potential for holes, $\eta_\mathrm{h} = \mu_\mathrm{h} + e\phi$, where μ_i, ϕ, and $\pm e\phi$ are the chemical potential, electrical potential, and vacuum energy for electrons and holes. The Fermi energies ($E_\mathrm{F} = \eta_\mathrm{e} = -\eta_\mathrm{h}$) for the conduction and valence bands of the n-type and p-type materials merge into the Fermi energy of the absorber and the metal terminals, $E_\mathrm{F,left}$ and $E_\mathrm{F,right}$ (Figure 2.1 b).

Illuminated Solar Cell Device

Under illumination and provided that the light energy is larger than the band-gap of the absorber, the electro-chemical potentials of electrons is raised and of holes lowered. The distribution function of electrons in the conduction band and holes in the valence band become quasi-Femi distributions with Fermi energies $E_\mathrm{FC} = \eta_\mathrm{e}$ and $E_\mathrm{FV} = -\eta_\mathrm{h}$ respectively (Figure 2.1 c, d). The difference between these Fermi energies

$$\mu_\mathrm{eh} \equiv E_\mathrm{FC} - E_\mathrm{FV} = \eta_\mathrm{e} + \eta_\mathrm{h} = \mu_\mathrm{e} + \mu_\mathrm{h} \tag{2.1}$$

is the chemical energy per electron hole pair gained by the absorbed photon [7]. As a result a voltage V develops from the difference of the Fermi energies at the left and right terminal [7]

$$eV = E_\mathrm{F,left} - E_\mathrm{F,right}. \tag{2.2}$$

Two forces act on the photo-generated electrons and holes simultaneously. One force is the electric field, $E = -\mathrm{grad}(\phi)$, acting on the charge, $q = z_i e$ ($z_\mathrm{e} = -1$ for electrons and $z_\mathrm{h} = 1$ for holes), and the other force is the gradient of the chemical potential, $\mathrm{grad}(\mu_i)$, acting on the charge carrier concentration n_i. The net force of both forces is the gradient of the electrochemical potential, $\mathrm{grad}(\eta_i)$, that drives the electrical current of each charge carrier

$$j_i = -\frac{\sigma_i}{q}\{\mathrm{grad}(\mu_i) + \mathrm{grad}(q\phi)\} = -\frac{\sigma_i}{q}\mathrm{grad}(\eta_i)\ , \tag{2.3}$$

where $\sigma_i = en_ib_i$ is the conductivity, which depends on the density and mobility b_i of the charge carrier [7]. The total photo-generated current in the device is

$$j_Q = j_\mathrm{e} + j_\mathrm{h} = \frac{\sigma_\mathrm{e}}{e}\mathrm{grad}(E_\mathrm{FC}) + \frac{\sigma_\mathrm{h}}{e}\mathrm{grad}(E_\mathrm{FV})\ . \tag{2.4}$$

If the device is disconnected from a load ($R_\mathrm{load} = \infty$) no charge current can flow, $j_Q = 0$. In this open-circuit condition the voltage at the terminals reaches its maximum, i.e. the open-circuit voltage $V = V_\mathrm{oc}$ (Figure 2.1 c). By connecting a circuit with a resistive load ($R_\mathrm{load} < \infty$), the voltage between the terminals is reduced ($V < V_\mathrm{oc}$). The onset of the driving forces $\mathrm{grad}(E_\mathrm{FC})$ and $\mathrm{grad}(E_\mathrm{FV})$ on the majority carriers in the n-type and p-type semiconductors respectively results in an electric current, $j_Q > 0$ (Equation 2.4), flowing into the external circuit [7]. If both terminals of the device are shorted ($R_\mathrm{load} = 0$ and $V = 0$) the produced charge current is referred to as short-circuit current j_sc or more conveniently as short-circuit current density J_sc (current per unit area) (Figure 2.1 d).

In the case the electric field is small compared to the chemical potential gradient, $-\mathrm{grad}(\phi) < \mathrm{grad}(\mu_i)$, charge carriers rely primarily on Brownian motion in order to reach the n-type or p-type material and become separated. Hence it is practical to specify a mean path length for the diffusion of a charge carrier during its lifetime τ_e. For a Brownian charge particle with diffusion coefficient D_e this path length is the diffusion length [7]

$$L_\mathrm{e} = \sqrt{D_\mathrm{e}\tau_\mathrm{e}}\ . \tag{2.5}$$

If the path of a charge carrier to the charge-separating n-type or p-type material is larger than L_e then an electron-hole pair will be lost by recombination before it can be separated.

Energy Delivery to a Load

The maximum energy delivered to an external load by a number of δN_e electrons and δN_h holes flowing in and out of the device is given by the Free energies

$$\delta F_\mathrm{e} = \eta_\mathrm{e} \delta N_\mathrm{e} \qquad \text{and} \qquad \delta F_\mathrm{h} = \eta_\mathrm{h} \delta N_\mathrm{h} \ . \tag{2.6}$$

With the flow of an electric current an equal number of electrons and holes are removed or added, i.e. $\delta N = \delta N_\mathrm{e} = \delta N_\mathrm{h}$. Thus the maximum chemical energy of δN generated electron-hole pairs is the total Free energy

$$\delta F = \delta F_\mathrm{e} + \delta F_\mathrm{h} = (\eta_\mathrm{e} + \eta_\mathrm{h}) \delta N = \mu_\mathrm{eh} \delta N \tag{2.7}$$

that an ideal solar cell device (for which $eV_\mathrm{oc} = \mu_\mathrm{eh}$) can utilize in order to perform electrical work in the external load [7].

In order to use the full Free energy δF the device needs to provide a maximum energy current density $J_\mathrm{max} V_\mathrm{max}$ (power output density) that is close to $\approx J_\mathrm{sc} V_\mathrm{oc}$. Thus, a measurable efficiency for how much of the Free energy is delivered to a load is conveniently expressed by the Fill Factor

$$\mathrm{FF} = \frac{J_\mathrm{max} V_\mathrm{max}}{J_\mathrm{sc} V_\mathrm{oc}} \ . \tag{2.8}$$

In real devices, losses occur in form of radiative and non-radiative recombination losses, resistive losses, and current leakage so that $V_\mathrm{max} < V_\mathrm{oc}$ and $J_\mathrm{max} < J_\mathrm{sc}$, and consequently $\mathrm{FF} < 1$. These losses can be reduced by material design and the geometry of the solar cell device, which will be discussed in the remaining part of Section 2.1 and Section 2.2.

2.1.2 Design Requirements and Efficiency Limit of a Solar Cell

The challenge for reducing losses in a solar cell device is to find suitable materials that lead to maximum conversion of light energy into chemical energy and to simultaneously assemble these materials in a design that enables efficient charge separation and transport to the load.

Requirements for the Solar Cell Design

The requirements for a solar cell design with minimal energy-conversion losses can be summarized as follows. First, the solar cell needs to absorb all incident light with energy larger than the band-gap of the absorbing semiconductor and generate electron-hole pairs. Second, all generated charge carriers need to reach the heterojunction during their lifetime. Third, all electron-hole pairs need to be separated at the heterojunction. Fourth, all separated charge carriers need to be collected at the terminals and transported to the load.

Losses occurring in a solar cell device with respect to each of these four conditions are conveniently addressed by the quantum efficiency (QE), often called internal quantum efficiency. The QE states the fraction of charge carriers that the solar cell device delivers to the external load as a function of energy of the incident photons (E),

$$\mathrm{QE}(E) = (1 - R(E))A(E)\,\eta_{\mathrm{trans}}(E)\,\eta_{\mathrm{sep}}(E)\,\eta_{\mathrm{col}}(E)\ , \tag{2.9}$$

where $R(E)$, $A(E)$, and the efficiencies $\eta_{\mathrm{trans}}(E)$, $\eta_{\mathrm{sep}}(E)$, and $\eta_{\mathrm{col}}(E)$ correspond to the probability of photon reflection at the device, photon absorption, charge carrier transfer to the heterojunction, charge separation, and charge collection at the terminals respectively [6; 8]. In a solar cell design each of these efficiencies need to be considered—a reduction of one of them due to device limitations or losses results in an overall reduction in the QE. For measurements (as described in Section 5.2.2), it is convenient to define the external quantum efficiency

$$\mathrm{EQE}(E) = \frac{\mathrm{QE}(E)}{(1 - R(E))}\ . \tag{2.10}$$

Theoretical Limit of Energy Conversion Efficiency

The efficiency of how much of the power density of the incident light, P_s, is maximally converted into electrical power density, P_max, by the solar cell device is given by its power-conversion efficiency

$$\eta = \frac{P_\mathrm{max}}{P_\mathrm{s}} = \frac{J_\mathrm{max}V_\mathrm{max}}{P_\mathrm{s}} = \frac{J_\mathrm{sc}V_\mathrm{oc}\mathrm{FF}}{P_\mathrm{s}} \ . \tag{2.11}$$

The theoretical limit of the obtainable power-conversion efficiency of a solar cell is determined by the detailed balance limit, first established by Shockley and Queisser in 1961 [9]. The detailed balance limit states that the spectral solar photon flux $f_\mathrm{s}(E)$ through a solid angle $\Omega(\theta_\mathrm{in})$ into the solar cell device is balanced by the spectral spontaneous-emission photon flux,

$$f_\mathrm{v}(E, T_\mathrm{a}, V) = \frac{2n_\mathrm{med}^2 E^2}{h^3c^2 \exp\left(\frac{E-eV}{k_\mathrm{B}T_\mathrm{a}}\right) - 1} \ ,$$

through the solid angle $\Omega(\theta_\mathrm{out})$ out of the device into its surroundings, where n_med, θ_in, and θ_out are the refractive index of the incident medium and the acceptance angles (half of the apex angle) of the incident and emitted light cone respectively [10]. The detailed balance limit also assumes complete absorption of incident light,

$$\mathrm{QE}(E) = A(E) = \begin{cases} 1 & \text{if } E \geq E_\mathrm{g} \\ 0 & \text{if } E < E_\mathrm{g} \ , \end{cases}$$

and that the solar cell is in thermal equilibrium with the ambient, radiating like a black body at ambient temperature T_a with a spectral photon flux, determined by Plank's radiation law,

$$f(E, T_\mathrm{a}) = \frac{2n_\mathrm{med}^2 E^2}{h^3c^2 \exp\left(\frac{E}{k_\mathrm{B}T_\mathrm{a}}\right) - 1}$$

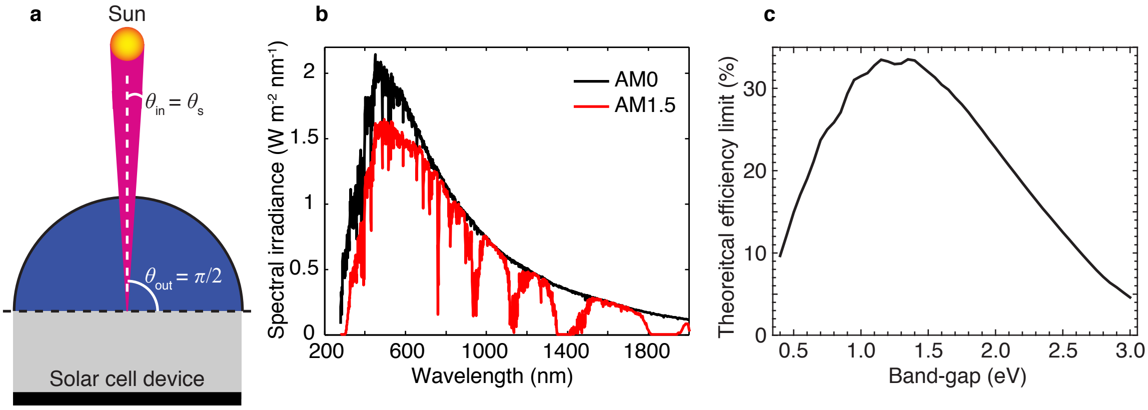

Figure 2.2: (**a**) Diagram of the acceptance angles of the incident (θ_{in}) solar light cone ($\theta_{\text{s}} = 0.26°$) and emitted ($\theta_{\text{out}}$) radiation cone for a solar cell device. (**b**) Spectral irradiance of the sun measured at sea level with a solar zenith angle of 48.2° (AM1.5) and at an extraterrestrial position (AM0) for comparison (Data from ref. [11]). (**c**) Theoretical limit for energy conversion efficiency of a single band-gap solar cell under AM1.5 sunlight plotted against band-gap of the absorber (Adapted from ref. [12]).

[6]. The balance of the photon flux in and out of the device results in a net current density generated by the device

$$\begin{aligned} J(V) = & e \int_0^{\theta_{\text{in}}} \int_{E_{\text{g}}}^{\infty} A(E)[f_{\text{s}}(E) - f(E, T_{\text{a}})] \cos\theta \, \mathrm{d}\Omega \, \mathrm{d}E \\ & - e \int_0^{\theta_{\text{out}}} \int_{E_{\text{g}}}^{\infty} A(E)[f_{\text{v}}(E, T_{\text{a}}, V) - f(E, T_{\text{a}})] \cos\theta \, \mathrm{d}\Omega \, \mathrm{d}E \end{aligned} \tag{2.12}$$

where the first and second integral describe the contributions from the net absorption and the net emission (or radiative recombination) current densities in excess to that at thermal equilibrium, respectively [10]. The theoretical limit for η (in Equation 2.11) results from calculating $P_{\text{s}} = \int_0^{\infty} E f_{\text{s}}(E) \, \mathrm{d}E$ and $P_{\max} = J(V_{\max})V_{\max}$, where $V_{\max}$ is obtained from the relation $0 = \mathrm{d}P/\mathrm{d}V = J(V_{\max}) + V_{\max}[\mathrm{d}J/\mathrm{d}V]_{\max}$ [10].

For the acceptance angle of the incident solar light cone ($\theta_{\text{in}} = 0.26°$), emission into the hemisphere ($\theta_{\text{out}} = \pi/2$), and the spectral irradiance $E f_{\text{s}}(E)$ of AM 1.5 sunlight, the theoretical limit of the energy-conversion efficiency of a single absorber solar cell device is ≈33%, at an optimum band-gap $E_{\text{g}} \approx 1.4\,\text{eV}$ of the absorbing semiconductor [6] (Figure 2.2). A method to further increase this η limit is to reduce radiative recombination losses by matching the acceptance angles $\theta_{\mathrm{in}} = \theta_{\mathrm{out}}$. This can be illustrated by rearranging the integrals in Equation (2.12) so that

$$\begin{aligned} J(V) =& e \int_{0}^{\theta_{\mathrm{in}}} \int_{E_{\mathrm{g}}}^{\infty} A(E)[f_{\mathrm{s}}(E) - f_{\mathrm{v}}(E, T_{\mathrm{a}}, V)] \cos\theta \, \mathrm{d}\Omega \, \mathrm{d}E \\ & - e \int_{\theta_{\mathrm{in}}}^{\theta_{\mathrm{out}}} \int_{E_{\mathrm{g}}}^{\infty} A(E)[f_{\mathrm{v}}(E, T_{\mathrm{a}}, V) - f(E, T_{\mathrm{a}})] \cos\theta \, \mathrm{d}\Omega \, \mathrm{d}E \; . \end{aligned} \tag{2.13}$$

If $\theta_{\mathrm{in}} = \theta_{\mathrm{out}}$ then the second integral vanishes and $J(V)$ is maximized, leading to η above 40% [10]. If charge-carrier thermalization losses would be reduced in e.g. tandem devices with multiple band-gaps or hot-carrier solar cells, which have lower cooling times of charge-carriers, the theoretical limit of the power-conversion efficiency could be even further raised above 86% by using $\theta_{\mathrm{in}} = \theta_{\mathrm{out}}$ [10; 13; 14].

As Figure 2.2 c shows, the theoretical limit of the device efficiency sets the requirement for the optimum band-gap of the absorbing material. State of the art materials that provide a band-gap close to the optimum of 1.4 eV are scarce. Inorganic materials include e.g. gallium arsenide (GaAs, $E_{\mathrm{g}} = 1.42\,\mathrm{eV}$), indium phosphide (InP, $E_{\mathrm{g}} = 1.35\,\mathrm{eV}$), cadmium telluride (CdTe, $E_{\mathrm{g}} = 1.44\,\mathrm{eV}$), copper indium gallium diselenide ($\mathrm{CuInGaSe_2}$, $E_{\mathrm{g}} = (1.0\text{–}1.7)\,\mathrm{eV}$), and silicon (Si, $E_{\mathrm{g}} = 1.1\,\mathrm{eV}$) [6]. Organic materials with band-gaps close to the optimum are even scarcer, band-gaps are usually above 1.9 eV. But this class of materials has the advantage of being chemically designed so that their band-gap can be tuned (more details on organic materials in Section 2.1.4 on page 16).

2.1.3 Inorganic Solar Cells

From 1876 the first solid state photovoltaic devices were developed when William Adams and Richard Day measured a photocurrent between two heated platinum contacts on a sample of selenium [6]. More solid thin-film devices followed that were

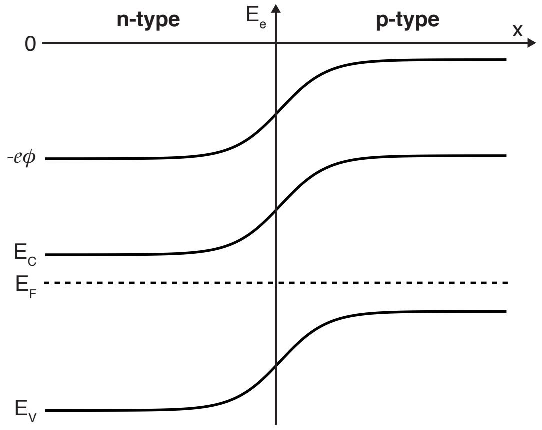

Figure 2.3: Band diagram of a p-n junction.

based on semiconductor-metal (Schottky) barrier contacts (not further discussed here). However the power produced of these structures was insignificantly low.

Crystalline Devices

Not until the 1950s were potentially useful quantities of power produced by photovoltaic devices in crystalline silicon [6]. In 1954 Chapin, Fuller, and Pearson developed the first silicon solar cell device that converted sunlight energy at 4.5% efficiency [15]. This device was based on a homojunction between phosphorous doped (n-type) and boron doped (p-type) silicon, called p-n junction, which produced much better rectifying action than the previous Schottky barriers (see Figure 2.3). Since then the solar cell industry has been dominated by inorganic solid-state devices, mainly based on crystalline silicon.

The highest energy conversion efficiency to date of a silicon solar cell device with a single p-n junction is nearly 25% under un-concentrated sunlight [16; 17]—already close to the theoretical limit of 29% for Si [6]. Such a silicon p-n junction consists of a ≈300 μm thick moderately doped p-type absorber (acceptor concentration $10^{15} < n_\mathrm{A} < 10^{16}\,\mathrm{cm}^{-3}$) that is sandwiched between a less then 1 μm thick, highly n-doped ($n_\mathrm{D} \approx 10^{19}\,\mathrm{cm}^{-3}$), electron collecting layer on the illuminated side and a micrometer thin, highly p-doped, hole collecting layer on the rear side [7].

However silicon is an indirect semiconductor which requires a phonon for the absorption transition between the valence and conduction bands under illumination due to the requirement for conservation of momentum. As a result, the absorption length of silicon is 100 µm. Hence the diffusion length of photogenerated charge carriers has to be at least 200 µm or at least twice the silicon thickness so that the charges can reach the p-n junction. But grain boundaries in the material possess defect states in the forbidden energy gap and reduce minority carrier lifetimes and therefore their diffusion lengths. Hence the grain size needs to exceed the device thickness so that the effect on the diffusion length remains small. For that reason crystalline silicon solar cell devices are used which typically suffer from energy-consuming fabrication and high production costs [18; 19].

Gallium arsenide (GaAs) is another material that is used for p-n homojunction solar cell devices. Alta-devices fabricated a crystalline device with 28.3% efficiency—the highest efficiency to date for a single junction device exposed to 1 sun [20]. The n-type region of GaAs can be doped with silicon or tin and the p-region with carbon or beryllium [6]. Because GaAs is a direct semiconductor the absorption length of GaAs is two orders of magnitude smaller compared to silicon so that devices can be made a few micrometers thin. The disadvantage is that production of high purity GaAs cells is 5–10 times more expensive than pure silicon cells [6]. The solution for the reduction of device production costs is to use materials from an ample supply without the requirement of long and demanding fabrication processes.

Poly-crystalline and Amorphous Thin-Film Devices

The mechanism of a thin-film solar cell device is based on a heterojunction between an absorber, n-type and p-type materials (similar to Figure 2.1 on page 5). In order to compete with crystalline silicon (c-Si) devices the absorbing material of thin-film devices requires direct transitions between the valence and conduction bands, which results in absorption lengths (L_A) of a few µm (Table 2.1). This length scale relaxes the demands of the diffusion length L_e of generated charge carriers so that defects, impurities, or grain boundaries may exist to a higher degree compared to the above crystalline devices.

n-type	p-type	L_{A} (µm)	α (cm^{-1})	η_{PCE} (%)	References	Year
CdS	CdTe	10	10^3	17.3	[21; 22]	2011
CdS	CIGS	0.1	10^5	20.3	[22; 23]	2011
GaAs	GaAs	1	10^4	18.4	[22; 24]	1996
nc-Si:H	a-Si:H	20	500	12.5	[20; 22]	2007

Table 2.1: Efficiency (η_{PCE}), absorption coefficient (α) at 1.5 eV, and absorption length ($L_{\mathrm{A}} = \alpha^{-1}$) of most efficient poly-crystalline thin-film solar cells based on the materials: Cadmium sulfide (CdS), cadmium telluride (CdTe), copper indium gallium diselenide ($\mathrm{CuIn_xGa_{1\text{-}x}Se_2}$; CIGS), gallium arsenide (GaAs), and hydrogenated nano-crystalline Si (nc-Si:H) and amorphous silicon (a-Si:H).

In contrast to c-Si, amorphous silicon (a-Si) is a direct semiconductor and was successfully used in combination with nano-crystalline silicon (nc-Si) in thin-film devices with efficiencies above 12% [20]. However in a-Si dangling bonds of the silicon atoms lead to energy states for electrons and holes that are not confined to bands and fill the entire forbidden gap, resulting in recombination centers for minority carriers. In order to dope a-Si and nc-Si to produce a p-n junction in these devices, the dangling bonds are saturated by the inclusion of about 10% hydrogen. But the defect density of the hydrogenated amorphous (a-Si:H) and nanocrystalline (nc-Si:H) silicon increases with light exposure resulting in a (10–30)% efficiency drop during the first six months of device operation [6].

Unfortunately many other direct semiconductors with favorable energy gaps cannot be doped equally well n-type and p-type, which demands the construction of a heterojunction [7]. The most efficient poly-crystalline thin-film devices to date that are based on poly-crystalline direct semiconductors with power-conversion efficiencies up to 20% are summarized in Table 2.1. Thin-film solar cell devices are based on poly-crystalline materials with less stringent purity demands compared to crystalline solar cells and make large scale productions feasible [25; 26]. However, material and manufacturing costs of these inorganic material devices are still too high for wide acceptance [26].

2.1.4 Organic Solar Cells

Organic solar cell devices are based on carbon-based molecules with semiconducting properties. These organic semiconductors owe their properties to electron delocalization along their conjugated backbones that mainly consist of alternating C−C and C=C bonds [8]. In contrast to most of their inorganic counterparts organic materials provide large absorption coefficients $\alpha \gtrapprox 10^5\,\mathrm{cm}^{-1}$ in the visible, i.e. absorption lengths ($L_\mathrm{A} = \alpha^{-1}$) on the 100 nm length scale, and allow adjustment of their band-gap by molecular design [27]. Due to inexpensive synthesis and solution processability in a roll-to-roll fashion with high throughput, these organic materials potentially fulfill the technological criterion for low-cost photovoltaic devices that can compete with current grid electricity.

However, the highest reported power-conversion efficiency of organic solar cell devices to date still remains below 9% [28].[1] This is a large difference from the theoretical Shockley-Queisser limit (in Section 2.1.2) as a result of recombination losses inherent in organic solar cells. One reason for these losses is that charge carrier mobilities in organic semiconductors are generally in the range of $(10^{-7}\text{–}10^{-3})\,\mathrm{cm}^2/\,\mathrm{V\,s}$ [27], which is many orders of magnitude less than in inorganic solar cells [30; 31]. The other reason for recombination losses in organic solar cells is that electron-hole pairs experience higher Coulomb attraction than in inorganic solar cells, which can be explained as follows. If an absorbed photon excites an electron from the highest occupied molecular orbital (HOMO) to the lowest unoccupied molecular orbital (LUMO) of an organic semiconductor, it generates a bound electron-hole pair (exciton) instead of free charge carriers (Figure 2.4 a,b). The exciton binding energy is between (0.1–1.4) eV in contrast to a few millielectron volts in inorganic semiconductors [27]. The larger binding energy arises from the fact that electrons and holes in organic semiconductors are localized and the low dielectric constant (usually $\varepsilon_\mathrm{r} \approx 3\text{–}4$) enhances the Coulomb attraction between them [32; 33]. Thus the organic solar cell device requires a mechanism to

---

[1] This applies to organic solar cells with a single heterojunction. A tandem solar cell with multiple heterojunctions reached more than 10% recently, as reported in ref. [29] and later on page 22.

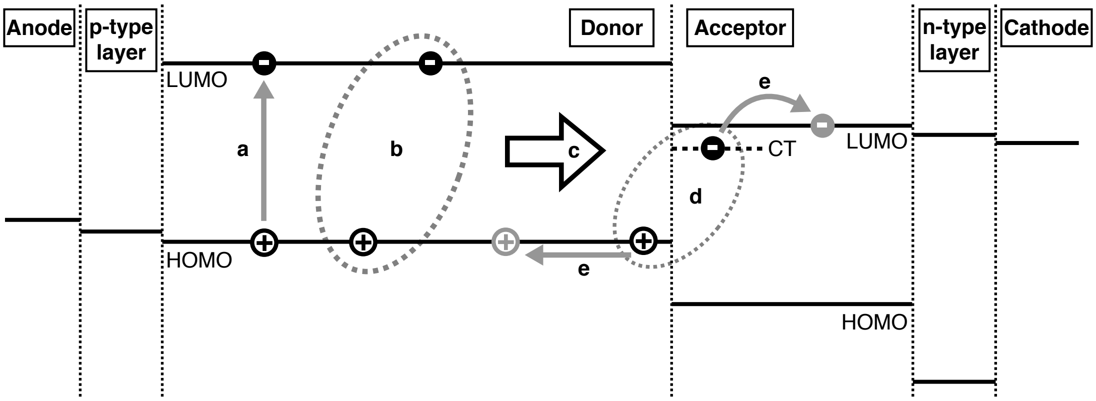

Figure 2.4: Energy level diagram illustrating charge separation in organic solar cells. Photon absorption excites an electron into the LUMO level of the donor (**a**) and forms a bound electron-hole pair (exciton) with the hole in the HOMO level (**b**). Excitons that manage to diffuse (**c**) to the donor-acceptor interface before they decay then form a localized interfacial electron-hole pair (**d**). The energy of the formed charge-transfer state (CT) illustrates the mutual Coulomb attraction of electron and hole. This Coulomb attraction must be overcome by the chemical potential gradient at the donor and acceptor interface so that the interfacial electron-hole pair can dissociate (**e**) in its lifetime.

dissociate generated excitons into free charge carriers before they undergo radiative or non-radiative decay, i.e. before electron-hole pairs recombine.

Mechanism of Organic Solar Cells

Organic solar cells involve a heterojunction between n-type and p-type organic semiconductors with different electron affinities, which serve as electron acceptor and electron donor material respectively and can both take the function of an absorber (Figure 2.4). Electron donor and acceptor materials are in contact with two charge collecting electrodes, anode and cathode respectively. Each electrode can be supplied with an additional semipermeable p-type and n-type interface layer, which selectively conducts holes and electrons to the anode and cathode respectively (Figure 2.4).

The dissociation of photo-generated excitons in the donor and acceptor material requires that excitons diffuse to the donor-acceptor interface before they decay (Figure 2.4 c). Once arrived at the interface, excitons tend to remain localized in a charge-transfer state because the ≈(0.5–1) nm wide separation of adjacent donor and acceptor molecules leads to a Coulomb attraction between localized electron and hole (Figure 2.4 d) [32]. The magnitude of the Coulomb attraction is in the range (0.1–0.5) eV and exceeds the thermal energy (0.025 eV) of both charges [32]. Hence the chemical potential gradient at the donor-acceptor interface must be sufficient to drive the charge carrier separation before the geminate electron-hole pairs recombine at the interface (Figure 2.4 e). Dissociated electrons and holes then need to travel through acceptor and donor respectively so that they can be collected at the electrodes before they recombine.

Planar Bilayer Organic Solar Cell

The first organic solar cell device was patented in 1979 [34] and developed in 1986 [35] by Ching W. Tang in form of a planar bilayer heterojunction with 1% power-conversion efficiency. The bilayer was produced by thermal evaporation of a p-type copper phthalocyanine molecule and a n-type perylene tetracarboxylic derivative under low pressure on the transparent conducting oxide indium doped tin oxide (ITO). Not until 1992 a 50–100 fs fast electron transfer between a buckminsterfullerene (C_{60}) derivative and the conjugated polymers poly(3-hexylthiophene) (P3HT) [36] and poly-[2-methoxy,5-(2'-ethyl-hexyloxy)-p-phenylene vinylene] (MEH-PPV) Sariciftci et al. [37] was demonstrated and led to the first solution processed polymer based solar cell device, reported by Sariciftci et al. [38] (structural formulas in Figure 2.5). This polymer solar cell device had a power-conversion efficiency of only 0.04% and its heterojunction was based on a planar bilayer morphology like the small molecule device from Tang. The reason for the modest power-conversion efficiency of planar organic solar cells is that the absorption length of organic semiconductors is about two orders of magnitude longer than their exciton diffusion length, which is usually in the range ≈(3–10) nm [27] (Figure 2.6 a). Consequently only a small fraction of the absorbed light generates excitons that can reach the interface of the heterojunction and dissociate. Thus the effective thickness of the absorbing material in the planar heterojunction is limited to the exciton diffusion length.

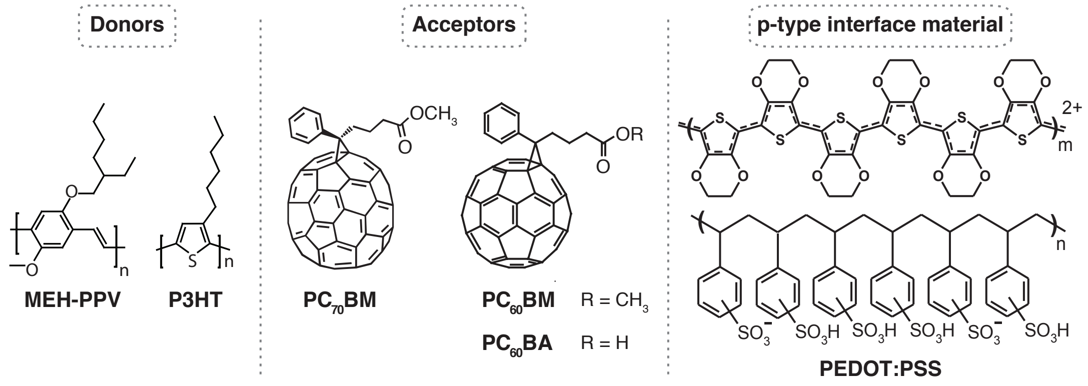

Figure 2.5: Structural formulas of common materials used as donors, acceptors, and interface layer in organic solar cell devices [8; 39–41]. Abbreviations are listed in Appendix A on page 112.

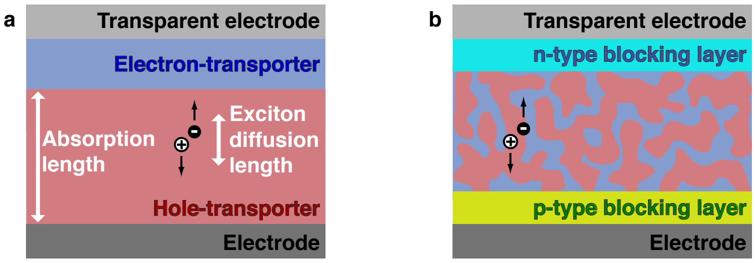

Figure 2.6: Heterojunctions in organic solar cell devices. The limited performance of devices based on a planar bilayer heterojunction (**a**) results from the short exciton diffusion (3–10 nm) compared to the absorption length. The bulk-heterojunction of blended donor and acceptor materials (**b**) results in better device performance. Device performance is further enhanced by the use of additional electron (p-type) and hole (n-type) blocking layers.

Organic Bulk-Heterojunction Solar Cell

A solution to the limitation of a planar heterojunction is to introduce a bulk-heterojunction which consists of donor and acceptor domains where excitons are generated in the proximity of the charge separating junction. Hiramoto et al. [42] first realized this concept through co-evaporation of donor and acceptor molecules at low pressures. Inspired by the established research on organic LEDs, the concept of a bulk-heterojunction was independently introduced in form of the solution processed polymer-polymer blend of MEH-PPV:CN-PPV [43] and fullerene-polymer blend of PC$_{60}$BM:MEH-PPV [44]. The organic blends in these devices consist of an interpenetrating network, formed from a phase-segregated mixture of the donor polymer and acceptor polymer or fullerene,

	p-type	Donor	Acceptor	n-type	Cathode	η_{PCE}	Year	Ref.
a	PEDOT:PSS	MDMO-PPV	$PC_{70}BM$	LiF	Al	3.0%	2003	[51]
b	–	MDMO-PPV	$PC_{60}BM$	LiF	Au	3.3%	2002	[52]
c	PEDOT:PSS	P3HT	$PC_{60}BM$	–	Al	5.0%	2005	[53]
d	PEDOT:PSS	PCPDTBT	$PC_{70}BM$	–	Al	5.5%	2007	[54]
e	PEDOT:PSS	PCDTBT	$PC_{70}BM$	TiO_x	Al	6.1%	2009	[55]
f	PEDOT:PSS	PTB7	$PC_{70}BM$	–	Ca Al	7.4%	2010	[56]

Table 2.2: Highest efficiencies (η_{PCE}) and materials used for cathodes, electron donor, electron acceptor, and n-type p-type interface layers of most efficient organic bulk-heterojunction solar cells. All devices had indium tin oxide (ITO) as transparent anode in common. Please find abbreviations of materials in Appendix A.

which forms the bulk-heterojunction. Compared with a planar heterojunction, the internal surface area of these bulk-heterojunctions was greatly increased (Figure 2.6 b), resulting in a larger photo-induced current density of the solar cell device. In particular heterojunctions based on $PC_{60}BM$:polymer blends have been intensively studied to date. The phase-segregation of these blends was shown to be in the range of (10–100) nm [43; 45–49]. Moreover, experiments on $PC_{60}BM$:polymer devices demonstrated that better device performance resulted from a higher exciton dissociation rate at the donor-acceptor interface and enhanced electron mobilities in the $PC_{60}BM$ domains [49; 50].

The relatively low hole mobility and narrow light absorption range of poly(p-phenylene vinylene) derivatives (PPV) limited further improvement of PPV-based solar cell devices to $\eta_{\mathrm{PCE}} \approx 3\%$ [8] (Table 2.2 a,b). This led to a number of different polymer-fullerene blends, such as $PC_{60}BM$:P3HT [40]. Optimizations of this blend led to great improvements in power-conversion efficiency, in the range of (4–5)% [8; 53] (Table 2.2 c). These optimizations were largely based on annealing the $PC_{60}BM$:P3HT blend, which further improved crystallinity and phase-segregtion of the blended domains [53].

Researchers found also in other $PC_{60}BM$:polymer blends that an improved morphology and crystallinity of the blended donor-acceptor domains lead to higher photo-induced charge generation and higher power-conversion efficiency [32]. The resulting increase in device performance was attributed to larger charge mobilities in the higher ordered domains and optimized domain size, which in turn enables excitons to diffuse to the donor-acceptor interface more efficiently. However studies on polymer:polymer [57] and PC_{60}BM:P3HT blends [58] showed that a too small domain size (<16 nm) leads to higher recombination rates of the electron-hole pair at the donor-acceptor interface. This suggested that the optimal domain size of (10–20) nm in a donor-acceptor blend is established by a balance of two requirements which are, first, efficient exciton dissociation and, second, exciton diffusion to the donor-acceptor interface [32].

Apart from optimizing the morphology and crystallinity of blended bulk-heterojunction solar cells, the efficiency of these devices was additionally improved by adding n-type and p-type layers in between the photoactive film and the cathode and anode respectively (as depicted in Figures 2.4 and 2.6 b). These interface layers transport holes and electrons selectively from the donor and acceptor materials to the electrodes [39]. The most common material used as p-type interface layer is poly(3,4-ethylenedioxythiophene):polystyrene sulfonate (PEDOT:PSS) [structural formula in Figure 2.5; established in devices (a,c–f) in Table 2.2]. But PEDOT:PSS is acidic and deteriorates the electrode contact over time so that it is often replaced by transition metal oxides, such as nickel oxide (NiO), molybdenum oxide (MoO_3), vanadium oxide (V_2O_5), and tungsten oxide (WO_3) [39]. Typical n-type interface layers, that can be grown by sol-gel methods, consist of titanium oxide (TiO_x) [55; 59] and zinc oxide (ZnO) [60; 61] layers, or lithium fluoride (LiF) [51; 52], from thermal evaporation (Table 2.2 a,b,e). If these interface layers are thick enough they additionally enhance the light intensity distribution in the photoactive film [62] (e.g. Table 2.2 e). Park et al. [55] reported an 70% increase in power-conversion efficiency by the use of a TiO_x interface layer compared to the device that provided direct contact between photoactive film and metal electrode [63].

However most of the polymers used for organic solar cells have a band-gap larger than 1.9 eV [8]. As a result, the solar cell device suffers from transmitting a large fraction of the solar spectrum and, therefore, low photocurrent densities J_{sc}. This issue was addressed by the development of low band-gap polymers, such as

PCPDTBT [54; 64] and PTB7 [56; 65] with band-gaps of 1.46 eV and 1.6 eV respectively (see abbreviations in Appendix A). In addition $PC_{60}BM$ was replaced with $PC_{70}BM$ which features a broader absorption range [51]. Solar cell devices with optimized blends of PCPDTBT and PTB7 as donor polymer and the electron acceptor $PC_{70}BM$ resulted in a considerable improvement in power-conversion efficiency (Table 2.2 d,f) [56]. The performance of organic solar cells can be further improved by combining polymers with different band-gaps in one device. This was realized in a tandem solar cell where two bulk-heterojunctions with different absorption ranges are stacked on top of each other and connected in series [8; 66]. Recently power-conversion efficiencies of an organic tandem solar cell exceeded 10% [29].

However, the benefit of larger J_{sc} in a single junction solar cell by lowering the band-gap of polymers is at the expense of the open-circuit voltage, because V_{oc} depends on the offset between acceptor LUMO level ($E^{\mathrm{A}}_{\mathrm{LUMO}}$) and donor HOMO level ($E^{\mathrm{D}}_{\mathrm{HOMO}}$) [32; 67],

$$V_{\mathrm{oc}} \propto E^{\mathrm{A}}_{\mathrm{LUMO}} - E^{\mathrm{D}}_{\mathrm{HOMO}} \, . \tag{2.14}$$

Moreover, engineering the energy levels of organic semiconductors is not sufficient for attaining high J_{sc}. Parameters, such as intermolecular interactions, molecular chain packing, and carrier mobility, affect J_{sc} too [8]. All these parameters are correlated. Optimizing them all in a single polymer represent a significant challenge [8].

Up to now, the bulk-heterojunction based on organic donor-acceptor blends features the best performing organic solar cell devices. Despite their good performance, the main limitation of these devices is their vulnerability to charge recombination which is caused by the low charge carrier mobilities inherent in organic semiconductors and indirect conduction pathways to the electrode in each donor and acceptor domain [27; 32; 68]. Consequently these limitations are associated to a morphology issue. Unfortunately the domains in donor-acceptor blends form autonomously during solvent evaporation so that the morphology of these bulk-heterojunctions is difficult to control.

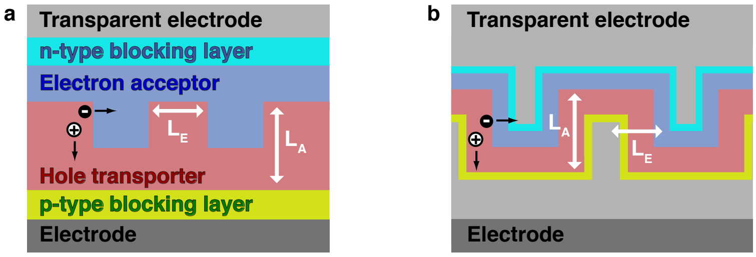

Figure 2.7: Schematic of a structured bulk-heterojunction illustrating exciton diffusion length L_E and absorption length L_A of the absorbing donor (**a**). By keeping donor and acceptor material thin (**b**), the conduction pathway to the electrode is further reduced, resulting in less recombination losses.

Structured Bulk-Heterojunction in Organic Solar Cells

The limitations of organic heterojunction blends can be addressed by systematically structuring their morphology (Figure 2.7). The requirements on the morphology of a structured bulk-heterojunction in organic solar cells are as follows.

(I) *Maximum absorption*: The thickness of the absorbing donor and acceptor material distributed throughout the bulk of the heterojunction should be on the order of the absorption length.

(II) *Charge separation*: The size of donor and acceptor domains should be on the order of the exciton diffusion length, i.e. typically ≈10 nm.

(III) *Charge transport*: Donor and acceptor domains should provide direct and continuous conduction pathways to the electrodes.

Attempts to meet these requirements include structured organic heterojunctions and organic-inorganic hybrid heterojunctions. Mainly these structured bulk-heterojunctions consist of rod or ridge-like features in the donor or acceptor that are vertically aligned to the substrate (Figure 2.7 a). But only a few of these heterojunctions were reported with a feature size comparable to the exciton diffusion length and a feature height comparable to the absorption length of the absorbing domain.

A suitable method to structure the bulk of organic heterojunctions involves the self-assembly of block copolymers, in which repeat units of donor and acceptor are covalently bound to each other via a linker unit [69]. Upon solvent evaporation these copolymers self-assemble and form highly ordered architectures. The morphology of these structures is controlled by the weight fractions of donor and acceptor oligomers and the size of the linker unit. Since this concept was applied to semiconducting copolymers by Sun [70] a variety of other donor and acceptor moieties were developed and implemented in heterojunctions. But efficiencies of these solar cell devices remains limited (η_{PCE}<1%) due to substantial recombination at covalent bonding sites at the polymer backbone [69; 71].

A more established technique for producing structured organic solar cells is nanoimprint lithography. This technique involves a mold which is used to imprint a structured pattern in the donor polymer of the heterojunction [72–75]. He et al. [76, 77] established nanoimprinted P3HT:$PC_{60}BM$, and other heterojunctions, with a feature size of 25 nm, which is closest to the exciton diffusion length produced by this technique so far. The power-conversion efficiency of the structured devices was fivefold larger than the planar control device and comparable to a polymer blend device. However only a fraction of the incident photons are harvested, because the thickness of the embossed polymer films was at maximum 80 nm, which is only a third of the absorption length of P3HT [31].

Inorganic materials provide the most flexible control on morphology and interface of structured bulk-heterojunctions. Metal oxide structures with pores [78–80], pillars [81], rods [82], and tubes [83–86] with diameters in the range of (10–100) nm were realized in organic-inorganic hybrid solar cell devices. An additional benefit of using metal oxides is that charge separation and open-circuit voltage in these structured hybrid devices can be increased by adjusting the chemical potential with various surface modifications. This was demonstrated on ZnO-P3HT heterojunctions by grafting carboxylated $PC_{60}BM$ ($PC_{60}BA$) on ZnO films [87], doping ZnO films with magnesium [88], or depositing thin TiO_2 films on ZnO nanorods (core-shell structure) [89].

Apart from influencing conduction pathways and charge separation at the donor-acceptor interface, the morphology of structured heterojunctions also affects the charge carrier mobility in conjugated polymers [31]. Coakley et al. [90] and Aryal et al. [91] showed that the polymer chains of P3HT aligned vertically in pores with a (75–80) nm diameter, resulting in a twentyfold enhancement of hole mobility compared to the coil conformation of P3HT in pores on the 10 nm length scale [79; 90]. But the hole mobility in P3HT and other conjugated polymers ($\lessapprox 10^{-4}\,\mathrm{cm}^2/\mathrm{V\,s}$) remains several orders of magnitude below that of inorganic materials such as metal oxides [90; 92].

In spite of the large electron mobilities, direct pathways in the structured metal oxides, and an improved performance compared to bilayer devices, the power-conversion efficiency of structured hybrid solar cell devices with a donor material (such as P3HT) remains below 1% [78; 81; 86–89]. Metal oxide structures used as electron transporter in combination with fullerene-polymer blends showed power-conversion efficiencies in the range of (2–4)% [82; 93]. This is still very low compared to the theoretically achievable efficiency. The reason for this is recombination losses. These losses occur because of the low hole mobility in the organic donor materials and long charge collection pathways. In the organic donor material holes need to travel a long way to the collecting electrode, on the order of several 100 nm, which makes them susceptible to recombination. An additional source of recombination losses is the difference in mobility of polymeric donor and metal oxide acceptor. As a result electrons are transported more quickly away from the junction than holes, which leads to the build-up of positive space charge in the donor [69; 90; 92]. This effect promotes recombination of charge carriers and saturation of the photocurrent of the device, referred to as space-charge limited current [92]. Consequently the structured solar cell devices to date suffer from significant recombination losses. A way to resolve this problem would be to make the donor material as thin as possible in order to facilitate fast collection of holes at the electrode or p-type interface layer (depicted in Figure 2.7 b).

2.1.5 Dye-sensitized Solar Cells

Different from the above solar cell designs, the dye-sensitized solar cell (DSSC) device is a photoelectrochemical system, pioneered by O'Regan and Grätzel in 1991 [94]. The DSSC comprises an inorganic n-type semiconductor, which acts as electron transporter and is sensitized with chemisorbed dye molecules. This sensitized n-conductor is surrounded by an electrolyte or p-type polymer that serves as hole transporter in form of a redox couple. The n-conductor and redox couple are in contact between two electrodes, usually a transparent conducting oxide (TCO) electrode and a platinum (Pt) counter electrode respectively. In comparison with the above inorganic solar cell devices, the main advantage of the DSSC heterojunction is the large choice of light absorber and charge transport materials, which can be applied by simple screen printing methods and do not rely on costly purification or doping processes.

The mechanism of the heterojunction is as follows (Figure 2.8). Absorption of a photon leads to excitation of the dye by promoting an electron from the ground state (D^0) to the excited state (D^*). The dye is then oxidized (state D^+) by injecting an electron into the n-type material where it diffuses to the TCO electrode. Subsequently the photo-oxidized dye is reduced by the reduced part of the redox couple. The formed oxidized redox species diffuses to the platinum counter electrode where it is reduced again. Because of the large charge density in the redox couple, the redox potential E_{redox} determines the electrochemical potential at the counter electrode in DSSCs. The redox couple also affects the electrochemical potential of the n-type semiconductor through the recombination kinetics between electrons in the n-conductor and oxidized redox species. Hence the redox couple is the key component of the DSSC setting the voltage between both electrodes of the device [95]. The open-circuit voltage in illuminated DSSCs is

$$V_{\mathrm{oc}} = \frac{1}{e}(E_{\mathrm{FC}} - E_{\mathrm{redox}}) \ , \tag{2.15}$$

where E_{FC} is the quasi-Fermi energy of the n-conductor that merges into the Fermi energy of the TCO electrode.

The energy conversion efficiency of a DSSC depends strongly on the kinetics of all involved reactions (1–7 in Figure 2.8 a). Charge separation can only occur if charge injection into the TiO_2 conduction band (1) is faster than the dye excited-state decay (2) to the ground state (D^0). Efficient hole transfer to the electrolyte requires the dye cation reduction by the redox couple (3) to be faster than recombination with injected electrons (4). Additionally efficient charge collection demands a faster charge transport

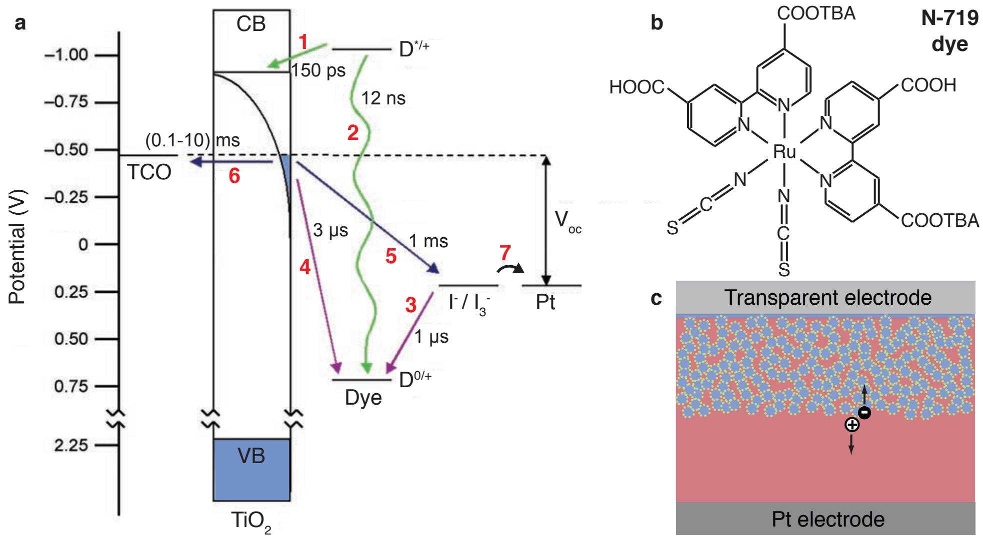

Figure 2.8: (**a**): Energy levels and kinetic processes of a dye-sensitized solar cell (DSSC). Possible transitions (1–7) with associated injection and recombination times are indicated for a DSSC comprising a nanocrystalline TiO_2 n-conductor, N-719 dye (**b**), I^-/I_3^- redox couple, and Pt counter electrode at open-circuit ($V_{oc} \approx 700\,\mathrm{mV}$). Adapted from refs. [96; 97]. (**c**): Schematic of nano-structured dye-sensitized solar cell consisting of n-type nano-particles (blue), dye molecules (green), hole transporter (red), and electrodes (grey).

to the working (6) and counter electrodes (7) than interception by the oxidized redox ion in the electrolyte (5).

Because of the moderate extinction of a dye molecule monolayer, the dye-sensitized n-conductor requires a bulk structure which provides a large interfacial area and allows chemisorption of a large density of dye molecules per projected area [98] (Figure 2.8 c). The surface area enhancement is represented by the roughness factor

$$\mathrm{RF} = \frac{A_{\mathrm{interfacial}}}{A_{\mathrm{projected}}} \tag{2.16}$$

which is the ratio of interfacial surface area of the heterojunction to the projected surface area.

DSSC devices that yield the highest power-conversion efficiencies to date above 11% consist of a nanocrystalline titania (TiO_2) n-conductor, with $\mathrm{RF} > 1000$, produced from a colloidal paste. Dye-sensitization of the resulting porous TiO_2 film with a ruthenium metal ligand complex and use of the liquid iodine-iodide (I^-/I_3^-) electrolyte as redox couple resulted in the highest device efficiencies up to 11.4% since the invention in 1991 [20; 94; 99; 100]. Only recently the use of two porphyrin dyes in combination with a new cobalt-tris(bipyridyl) redox electrolyte led to a DSSC record power-conversion efficiency of 12.3% [101]. This perfomance was mainly attributed to the broad absorption spectrum of the incorporated dyes and a retarded electron back-transfer from the TiO_2 to the oxidized cobalt species in the redox couple. However solvent based electrolyte devices are not practical for long-term applications due to concerns about corrosion and solvent-leakage [102]. Devices involving solid organic hole transporters, such as spiro-MeOTAD, or solvent-free ionic liquids—often referred to as quasi-solid redox couples—are more promising for practical applications. Their efficiencies however remain modest compared to liquid electrolyte devices and have been reported between 5–8% depending on the type of materials used [103–107].

Limitations of DSSCs

In the more efficient electrolyte DSSCs the primary recombination process is from electrons in the nanocrystalline n-conductor to the cation in the solution. In case of devices with I^-/I_3^- electrolyte, Law et al. [108] and Kuang et al. [109] identified this recombination process as reason for a thickness limitation of the colloidal n-type film. They showed that nanocrystalline films had an optimal thickness, above which the device efficiency and photo-induced charge current decreased, in spite of containing a larger amount of dyes. The reason for this is that the nanocrystalline material is prone to surface defects which lead to sub-band gap energy states [7]. If electrons are trapped in these states, they need to be thermally released in order to continue their path to the electrode. This trap and thermal release process between sub-band gap states is referred to as hopping and reduces the electron diffusion constant in nanocrystalline TiO_2 by three orders of magnitude in contrast to single-crystalline anatase [96]. Transient photocurrent decay measurements revealed a charge carrier mobility of $\approx 10^{-5}\,\mathrm{cm^2/V\,s}$ in nanocrystalline TiO_2 structures [110], which is six orders of magnitude smaller than in a single crystal of anatase [30]. Electron diffusion times in 10 μm thick nanocrystalline dye-sensitized films can be up to (1–10) ms [111] so that electrons become susceptible to a back-transfer to the dye or to the redox couple [96; 109; 112]. This is the main limitation of device performance with most redox couples in DSSCs [109]. The superior performance of devices with the I^-/I_3^- electrolyte is mainly because the recombination time between injected electrons and oxidized redox species I_3^- is ≈1 ms which is very long compared to other redox couples [95].

The Durrant group found that the device performance can be enhanced by passivating the surface defects of DSSCs with an insulating material layer (shell) between the n-conductor and the dye [113–115]. This shell increases the separation between the materials and thereby reduces the Coulomb attraction between charge carriers across the interface. Suitable insulators have been proposed in form of alkyl chains on the dye molecule [114]. Palomares et al. [113] followed a different route and deposited various insulating metal oxide layers onto the n-conductor which resulted in a 35% increase in power-conversion efficiency of the DSSC.

Haque et al. [116] introduced this concept in form of minimizing the kinetic redundancy between the rate of charge injection into the n-conductor (1) and the rate of the dye's excited-state decay (2) (in Figure 2.8 a on page 27). Since electrons need to tunnel through the insulator, the injection from the excited dye into the n-conductor is impeded, but simultaneously the back-transfer to the dye or to the redox couple is retarded. This means, if the charge separation kinetics are just fast enough to compete with the decay of the dye excited-state then a minimum kinetic redundancy is obtained and leads to minimal charge recombination losses and consequently to maximum electron injection yield and better device performance. However the device performance is still limited by the poor charge transport through the nanocrystalline n-conductor and the open-circuit voltage.

Structured Bulk Architecture

One way to enhance V_{oc} is to raise the quasi-Fermi level in the n-type semiconductor. Feng et al. [117] reported a larger open-circuit voltage due to an increase in the

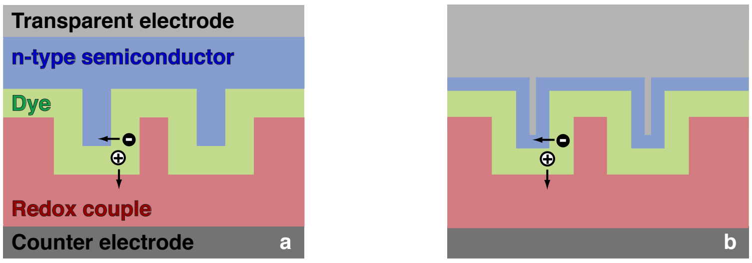

Figure 2.9: Structured DSSC provides direct conduction pathways and faster charge transport (**a**). By incorporating an electrode layer in the bulk of the structure, the conduction pathway is further reduced (**b**).

quasi-Fermi level of TiO_2 by doping TiO_2 with tantalum. Another way to increase V_{oc} is to find another redox couple with a lower redox potential E_{redox} [96]. But at the same time the new redox couple requires that rates of recombination, between redox cations and electrons in the n-conductor, match the (1–10) ms duration of electron transport to the electrode. A way to relax these requirements for new redox couples is to improve the charge transport through the n-conductor.

Analogously to organic solar cells, the charge transport in DSSCs is improved by structuring bulk-heterojunctions so that they provide direct conduction pathways from the dye to the electrode (Figure 2.9 a). Structured metal oxides were realized in DSSC heterojunctions in form of nanorods [118], nanowires [119], a nano-forest [120], nanotubes [84; 121–123], and mesoporous block-copolymer assembled networks [124–127]. Transmission electron micrographs [126] and transient photocurrent measurements [127] on mesoporous TiO_2 networks confirmed that a larger crystallite size and direct conduction pathways result in faster charge transport and higher power-conversion efficiency compared to conventional nanocrystalline DSSC devices. By comparing a nanocrystalline DSSC to a ZnO nanotube DSSC, researchers showed that the charge transport in the nanotube devices was two orders of magnitude faster as a result of direct conduction pathways [128].

A method to further reduce the conduction pathway for electrons to the collecting electrode is to incorporate a transparent electrode into the bulk of the n-type semiconductor structure (Figure 2.9 b). This reduces the diffusion path for electrons to the electrode without sacrificing interfacial surface area of the heterojunction. The most convenient way to include a transparent electrode layer in the bulk of a DSSC is to build this electrode and the n-type semiconductor on a template. Ideally this template possesses a roughness factor similar to the one of the above colloidal DSSCs, RF>1000. Martinson et al. [129] produced DSSC devices based on a template in form of a mesoporous membrane with 200 nm wide and 60 μm long wells (RF≈300). They made DSSC I^-/I_3^- electrolyte devices by incorporating a transparent electrode layer of indium tin oxide (ITO) into the template and adding a few nanometer thick titania layer onto the ITO electrode. In comparison to the same device without ITO film, the device including the electrode layer already enhanced the photo-induced charge current by more than an order of magnitude, which was attributed to more efficient charge collection [129]. These experiments demonstrate that the geometry of the DSSC can compensate for material properties that are disadvantageous for the device performance. The approach of depositing materials onto templates, such as the above tube framework, offers more freedom to choose the geometry for a heterojunction. The versatile deposition technique atomic layer deposition is particularly well suited for this purpose (see Chapter 4 on page 63). But compared to the colloidal based DSSC architectures above, the power-conversion efficiency of this template DSSC remains low. This is because of its low absorption efficiency (A) resulting from the low roughness factor (RF<1000) of the nanotube geometry. Thus a design with a larger roughness factor is required. Alternatively, A can be improved by photon management as indicated in Chapter 1. This means, instead of implementing a larger density of dye molecules in the device, the absorption efficiency is increased by controlling the light distribution in the bulk of the DSSC.

2.2 Combining Photonic Crystals and Solar Cells

There are different photonic concepts for increasing the absorption efficiency of a solar cell device without increasing the amount of absorbing material. One is based on light trapping in order to increase the matter-radiation interaction time and hence the optical path length in the device. Another aims to further increase the power conversion efficiency by reducing radiative recombination losses with the acceptance angles of the incident and emission light cones. The optical properties of photonic crystals are advantageous to achieve these goals. The light trapping concept and light trapping solar cell devices established to date will be introduced in Section 2.2.1. The method to change the acceptance angles will be presented in Section 2.2.2.

2.2.1 Light Trapping

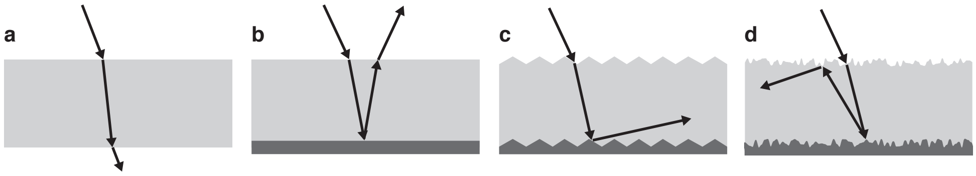

Figure 2.10: Absorption of a solar cell (**a**) can be improved by various light trapping concepts, such as a back-reflecting layer (**b**), structuring of front-surface and back-reflector (**c**), or randomly roughening of front-surface and back-reflector (**d**).

Various light trapping methods for increasing the optical path length in a solar cell device have been explored in the past (Figure 2.10). The simplest method is to include a back-reflector in form of a metal film or a Bragg stack [130; 131]: both increase the light path in the device by a factor of two (Figure 2.10 b). Structuring the front surface and back-reflector of the device [6], e.g. in the form of an array of pyramidal structures [132] (Figure 2.10 c), leads to reflection at angles larger than the critical angle for total internal reflection at the front surface and thus further increases the optical path length. Randomly roughened surfaces provide an even larger optical path length enhancement, limited to $4n^2$ [133] (Figure 2.10 d), i.e. $\approx 50\times$ for a silicon device with the refractive index of $n = 3.5$. But the best realized enhancement factor is about 10 times [6].

Periodic gratings at the front [134] or rear surface [135; 136] of a solar cell device can further increase the optical path length in the device (Figure 2.11 a). The upper limit of the optical path length enhancement is $91n$ (≈ 318 for silicon) at nearly normal angle diffractions [137]. But periodic gratings suffer from significant reflection losses. Zeng et al. [138] developed a structure that combines the high reflectivity of a

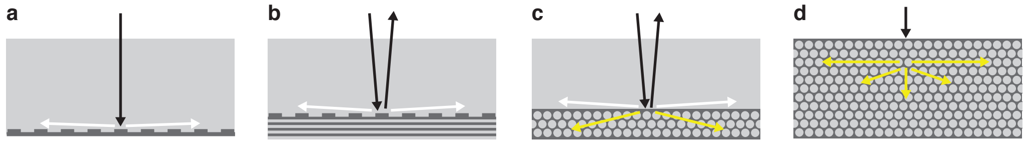

Figure 2.11: Absorption enhancement in a solar cell device due to reflection (black arrows) and diffraction (white arrows) at periodic gratings (**a**) or at a combination of a grating with a Bragg reflector (**b**). A photonic crystal can be utilized as a back-reflector (**c**) too or as a solar cell device itself (**d**) by providing in-plane and slow light Bloch modes (yellow arrows) to which incident light can couple.

Bragg-reflector with the diffraction properties of a grating and which is able to increase the EQE of a device more than tenfold over a spectral width of 100 nm (Figure 2.11 b). The narrow spectral widths of binary diffraction gratings can be further increased by designing more complex two-dimensional gratings [139; 140].

Another convenient structure, which allows complete control over reflectivity and diffraction properties is a three-dimensional photonic crystal. The first solar cell device with a three-dimensional photonic crystal was made by Nishimura et al. [141] who placed a titania inverse opal in contact with a nanocrystalline titania film of a DSSC (Figure 2.11 c), which led to a 26% increase in photo-current compared to a reference DSSC device. Mihi and Míguez [142] attributed this enhancement to optical coupling between the nanocrystalline titania layer and the photonic crystal, which resulted in standing waves in the absorbing nanocrystalline film, occurring in the spectral region of the opal structure's photonic band-gap [143]. Other nanocrystalline and inverse opal bi-layer DSSC devices followed [144–147], including designs that involved a stack of multiple inverse opals with different lattice constants in order to extend the spectral region of the resonant modes over the full absorption spectrum of the solar cell absorber [148; 149]. Up to 60% enhancement in absorption efficiency can be achieved this way [148].

In addition to utilizing the reflected and diffracted light of photonic crystals, refracted modes can be used for light localization within the photonic crystal structure itself [150] (Figure 2.11 d). The control over the photonic band-structure (see Section **??**) enables incident light to couple to in-plane modes within the photonic crystal film [151],

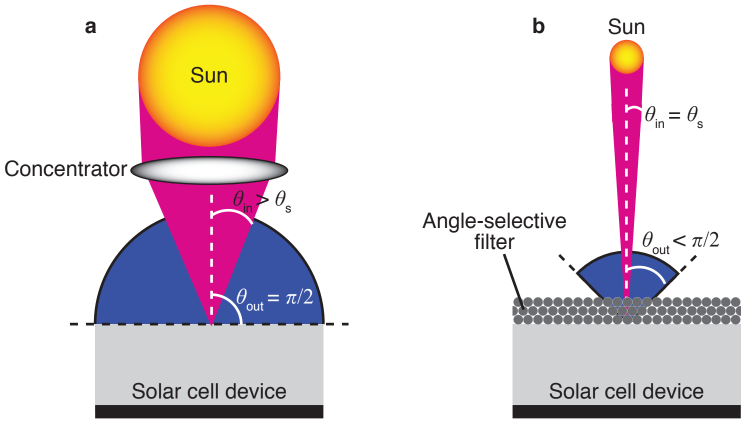

Figure 2.12: For a solar cell device, the acceptance angles of the incident (θ_{in}) solar light cone ($\theta_{\text{s}} = 0.26°$) and emitted ($\theta_{\text{out}}$) radiation cone can be adjusted with a concentrator (**a**) and an angle-selective filter (**b**) respectively.

including modes with a slow group velocity (slow light modes) resulting from a flat dispersion curve [152]. Duché et al. [153] proposed a two-dimensional photonic crystal slab of a P3HT:PC$_{60}$BM blend in which the incident light can couple to slow Bloch modes within the absorbing slab. They optimized the absorption enhancement of the structure to 36% in the spectral region of 600–700 nm where the absorption spectrum of P3HT tails off. The three-dimensional photonic crystal DSSC devices established so far are mainly based on titania inverse opals [154–158]. Only one group identified the EQE enhancement caused by the photonic crystal structure, which amounted to 8% in the spectral range of 550–650 nm and which was associated with optical coupling to slow group-velocity modes in the inverse opal DSSC device [156].

2.2.2 Concentration and Angular Confinement

Instead of increasing the optical path length in the device, a different method to enhance its power conversion efficiency is to concentrate the incident sunlight or angularly confine the emitted radiation. As demonstrated in Section 2.1.2, η is maximized if the acceptance angles of the incident (θ_{in}) and emitted (θ_{out}) light cones match.

There are two ways in order to achieve this. One is to use a concentrator that increases θ_{in} [159] (Figure 2.12 a). Concentrators were developed as nonimaging optics with refractive and reflective components such as lenses or mirrors [160–162]

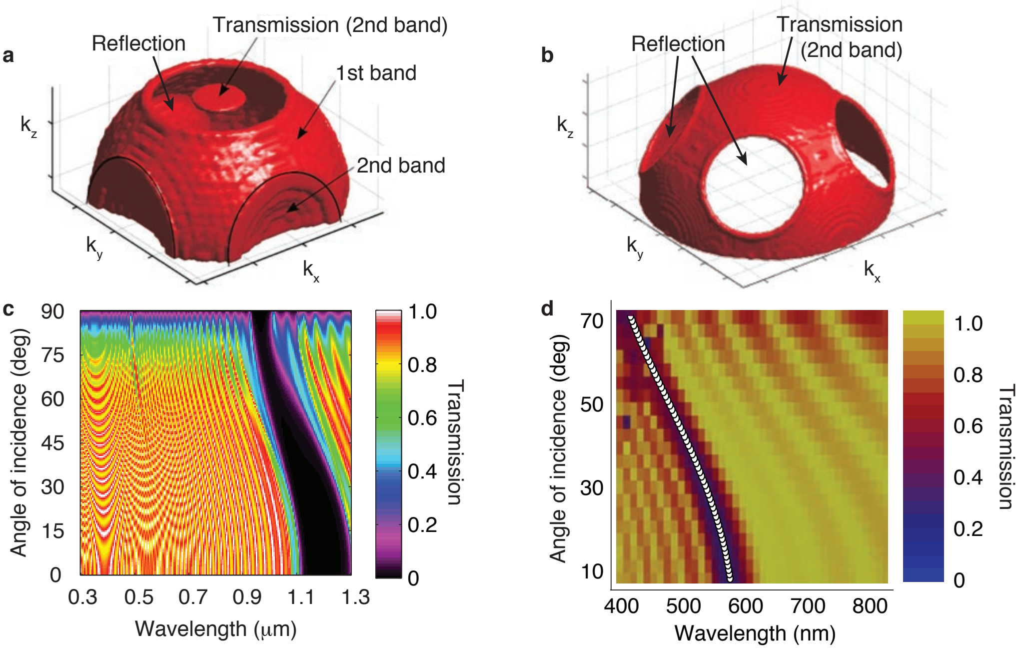

Figure 2.13: Isofrequency surfaces of a Rugate filter (**a**) and a three-dimensional (fcc) inverse opal (**b**) illustrate the angular confinement of modes that are able to transmit incident light from the hemisphere into a solar cell device and vice versa. Angle-resolved transmission spectra of such a Rugate filter (**c**) and inverse opal (**d**). The angular dependence of the center wavelength of the photonic band-gap according to Equation (2.17) holds for the inverse opal up to a 70° angle of incidence (white dotted line in **d**). Adapted from refs. [137; 167; 168].

that already can be integrated directly in the solar cell device in the form of microlenses [163–165]. The other method to use an angle-selective filter that confines θ_{out} [159] (Figure 2.12 b). For this purpose the angle-selective filter needs to be transmissive for $\theta \leq \theta_{\text{in}}$ and reflective for $\theta > \theta_{\text{in}}$ over the entire spectral absorption range of the absorber. Until now a structure that fulfills these requirements remains unknown [166]. However, these conditions are partially met by photonic crystals that have a photonic band-gap which depends on the angle θ of the incident light beam.

Two types of photonic structures have been considered as angle-selective filters to date. These are a Rugate filter [167] and an inverse opal [169]. Their isofrequency surfaces illustrate the transmitted and reflected modes [137] (Figure 2.13 a and b respectively). Like a Bragg stack, a Rugate filter consists of a periodic refractive index modulation in one dimension, but instead of a discrete modulation the refractive index profile is smooth and sinusoidal, which prevents higher order reflections [167]. The spectral position of the reflection peak of a Rugate filter (Figure 2.13 c) follows the angular dependence of a Bragg stack

$$\lambda_0 = 2d\sqrt{\tilde{n}^2 - \sin^2\theta} \tag{2.17}$$

where $\tilde{n}$ and d are the average refractive index and the periodicity of the refractive index modulation respectively [166–168]. Similar angular transmission characteristics apply to a three-dimensional photonic crystal such as an inverse opal [168] (Figure 2.13 d). Despite the frequency dependence and limited spectral range of the angular transmission confinement of photonic crystals, a model of a silicon solar cell device showed that if equipped with a Rugate filter or an inverse opal its gain in energy yield can be up to 4.7% or 7.5% respectively. In both cases the absorption efficiency was enlarged by placing the high energy edge of the photonic band-gap of each structure in the spectral region where the absorption spectrum of the absorber tails off [170].

2.3 Objective of this Thesis

As shown in the previous sections, photonic crystals facilitate a higher power-conversion efficiency of solar cell devices by increasing the absorption efficiency via optical path length enhancement or by reducing radiative recombination losses via tuning the acceptance light cones. An additional advantage of using photonic crystals in solar cell devices is that their structure can provide interconnectivity, ensuring direct conduction pathways for photo-generated charge carriers and minimizing recombination losses (described in Section 2.1.4 Figure 2.7 and Section 2.1.5 Figure 2.9). However fabricating solar cell devices based on photonic crystals on an industrial scale is a challenge.

A time-and cost-effective technique to fabricate photonic crystals on a large scale is holographic lithography which has the advantage that it offers flexible control over lattice constant and symmetry of the photonic crystal structure. This is not only beneficial for adjusting its optical properties but also for designing a three-dimensional photonic crystal solar cell device in which the heterojunction is incorporated into

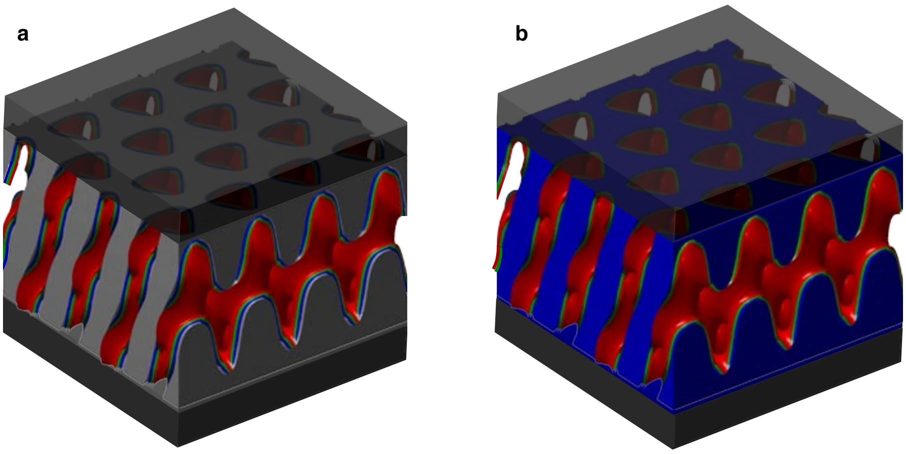

Figure 2.14: Scheme of solar cell device based on a metal oxide photonic crystal structure which serves as (**a**) a transparent conducting oxide electrode (gray) or as (**b**) an electron-transporter (blue). Multiple material films permeate the porous photonic crystal structure to form the heterojunction of the solar cell device. The layers function as electron-transporter (blue), absorber (green), and hole-transporter (red). Top and bottom layer of the heterojunction are each in contact with an electrode (dark gray).

the bulk of the photonic crystal and consists of multiple films functioning as light absorber and charge transporters (as depicted in Figure 2.14). In this case the thickness of an organic absorbing film such as P3HT can be reduced to its exciton diffusion length without sacrificing the total absorption of the device, which achieves efficient absorption by folding many absorbing layers into the thickness of the device. Hence the recombination losses in the organic absorber film can be conveniently diminished by controlling the geometry of the device. If the pore size of the photonic crystal is large enough, multiple heterojunctions with complementary absorbers can be implemented on top of each other in the bulk of the photonic crystal analogously to a tandem device. The larger spectral absorption range and higher output voltage would result in a larger power-conversion efficiency.

The aim of this thesis is to fabricate a solar cell device based on a metal oxide photonic crystal structure that serves as a transparent conducting oxide (TCO) electrode or as an electron-transporter of the device and which is coated with multiple material films that function as absorber and hole-transporter. For this purpose the plan is to produce a photonic crystal polymer template by holographic lithography (Scheme 1 a),

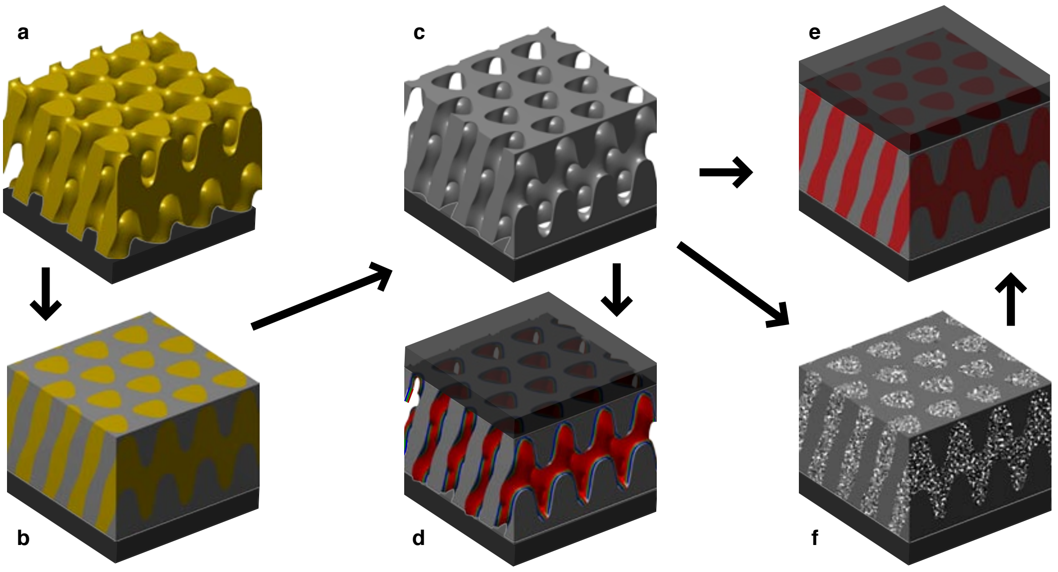

Scheme 1: Processes required to fabricate the planned solar cell devices: Photonic crystal polymer template produced by holographic lithography (**a**). Atomic layer deposition (ALD) of metal oxides (**b**). Removal of the template by etching and calcination (**c**). Incorporation of the photonic crystal structure into an organic-inorganic hybrid solar cell (**d**) or a DSSC device (**e**). In a different DSSC device the pores of the photonic crystal structure are filled with a nanocrystalline metal oxide (**f**) in order to increase the roughness factor of the electron-transporter.

coat it with the metal oxide by atomic layer deposition (ALD) (Scheme 1 b), remove the template by etching and calcination (Scheme 1 c), and to add the remaining materials that complete the heterojunction (Scheme 1 d–f). In Scheme 1 three different metal oxides are planned to be deposited. The transparent conducting oxide aluminum doped zinc oxide (ZnO:Al) serves as electrode material. Zinc oxide (ZnO) and titanium dioxide (TiO_2) are intended as electron-transporters for two different type of solar cell devices, an organic-inorganic hybrid solar cell (Scheme 1 d) and a DSSC (Scheme 1 e) respectively. The organic-inorganic hybrid device contains P3HT and PEDOT:PSS and the DSSC contains the dye N-719 and I^-/I_3^- electrolyte as absorber and hole-transporter respectively (see abbreviations in Section A).

An additional plan is to combine the advanced conduction properties of the above photonic crystal DSSC with the large roughness factor of a nanocrystalline DSSC by utilizing the TiO_2 photonic crystal structure as a container for TiO_2 nano-particles (Scheme 1 f) and by using this structure as an electron-transporter in the DSSC device.

This approach is different to the previously discussed inverse opal–nanocrystalline bi-layer DSSC device (Figure 2.11 c) where the photonic crystal structure acts as reflector and where electrons in the absorbing nanocrystalline material are susceptible to recombination. The advantage of putting the nanocrystalline material into the photonic crystal framework is that, without sacrificing much of the roughness factor, the longest path for electrons to reach the collecting photonic crystal structure is the pore size, on the order of hundred nanometers, compared to a few micrometers in a nanocrystalline DSSC.

In order to realize the solar cell devices according to Scheme 1 the following challenges were addressed.

(I) By using the established holographic lithography apparatus in our group the resulting photonic crystal templates were not uniform enough in order to be useful for a solar cell device so that the apparatus needed to be modified.

(II) The produced photonic crystal templates decomposed above 90°C, but the ALD processes for ZnO:Al, TiO_2, and ZnO take place above 100°C. Thus, the polymer template required thermal stabilization in order to withstand the ALD processing temperatures.

(III) During fabrication the template demanded a polymer layer at the substrate which prevented its delamination. However, this polymer layer needed to be permeabilized to the ALD precursors so that the resulting ALD film was in contact with the substrate.

(IV) An ALD apparatus was built.

(V) ALD processes for TiO_2, ZnO, Al_2O_3, ZnO:Al, and zirconium nitride Zr_3N_4 were established. The grown ALD films required characterization, which included measuring the growth per ALD cycle, composition, crystallinity and refractive index of each ALD film, and confirming conformal ALD in the bulk of the photonic crystal template. The conductivity of ZnO:Al films was measured and optimized by finding the optimum ALD temperature and ALD sequence of the Al_2O_3 dopant. Because of its high refractive index (larger than 3), Zr_3N_4 was used to test uniformity of film growth in the ALD reactor and in order to produce photonic crystals with high refractive index contrast.

(VI) A method in order to remove the photonic crystal polymer template from the ALD film was developed.

(VII) The metal oxide photonic crystal structures were implemented in a DSSC and an organic-inorganic hybrid solar cell device by applying solution processing techniques reported in the literature.

(VIII) A method for filling TiO_2 nano-particles into the TiO_2 photonic crystal framework and implementing this structure as an electron-transporter in a DSSC device was developed.

(IX) The power-conversion efficiency, EQE, and charge-carrier transport properties of the fabricated devices were characterized and compared with nano-crystalline DSSC and flat organic-inorganic reference devices.

These challenges will be addressed in the following three chapters: (I)–(III) in Chapter 3, (IV)–(VI) in Chapter 4, and (VII)–(IX) in Chapter 5.

3 Photonic Crystal Fabrication and Characterization

3.1 Introduction

As outlined in the last chapter, the aim of this thesis was to produce solar cells based on photonic crystal microstructure templates. This chapter introduces a technique called holographic lithography which is used to produce these photonic crystal templates (Section 3.2). The attachment of the photonic crystal template film to a substrate employs a thin polymer film (under-coat) which is described in Section 3.3. Section 3.4 illustrates the procedure for increasing uniformity of under-coats and and templates. A reinforcement method has been developed in order to make photonic crystal microstructures more suitable for use as templates for solar cell devices, which is discussed and summarized in Section 3.5.

3.2 Holographic Lithography

Holographic lithography is a very fast, controllable and potentially industrially scalable technique that is capable of producing photonic crystals with one, two [171; 172], or three-dimensional [173; 174] periodicity. Multiple interfering laser beams are used to create a one, two, or three-dimensionally periodic interference pattern, which is rendered into a solid material by exposing a film, of called photo-resist (Figure 3.1). The resulting photonic crystal structure percolates and possesses local connectivity, which is favorable for large photonic band-gap formation at low dielectric contrast [175; 176].

The translational symmetry of the crystal structure as well as the crystal basis can be controlled by tuning the intensity profile of the interference pattern. The intensity distribution of N interfering beams is given by

$$I(\boldsymbol{r}) = \sum_{n,m=0}^{N-1} S_{nm}\,\mathrm{e}^{-i\boldsymbol{G}_{nm}\cdot\boldsymbol{r}} \tag{3.1}$$

where the form factor, $S_{nm} = \boldsymbol{E}_n \cdot \boldsymbol{E}_m^*$, regulates the intensity distribution within each unit cell, i.e. the crystal basis, and is determined by the overlap of the polarization of the interfering beams. The wavevector differences of the interfering beams define the reciprocal lattice vector of the crystal structure, $\boldsymbol{G}_{nm} = \boldsymbol{k}_n - \boldsymbol{k}_m$. This turns holographic lithography into an extremely flexible technique for the production of high-quality photonic crystals. It offers total freedom to design the translational symmetry of a photonic crystal, and substantial flexibility in the design of the unit cell [177].

3.2.1 Holographic Exposures

In this thesis, three-dimensional photonic crystals were produced with a rhombohedral structure with face-centered cubic (fcc) translational symmetry. One reason for choosing this structure is that the laser beams for holographic exposures could be conveniently arranged from the same half-space of the photo-resist. The reciprocal lattice vectors $\boldsymbol{G}_{12} = 2\pi/a[\bar{1}11]$, $\boldsymbol{G}_{34} = 2\pi/a[1\bar{1}1]$, and $\boldsymbol{G}_{56} = 2\pi/a[11\bar{1}]$ with a lattice constant $a = 600\,\mathrm{nm}$ were chosen. This pattern can be either realized by a single exposure to four interfering laser beams [173; 179–182] or by three sequential exposures to two interfering laser beams [183; 184], each separated by a rotation of 120° around the optical axis [178] (as depicted in Figure 3.1). The lattice constant of the four-beam interference pattern, which is determined by the modulus $|\boldsymbol{G}_{nm}|$, has a fixed relationship to the laser wavelength λ_{beam}. For this reason three-by-two beam holographic lithography was used, because its advantage over the four-beam exposure is that the angle between the two laser beams, α, can be altered to adjust $|\boldsymbol{G}_{nm}|$ independently of λ_{beam} (Figure 3.2 a)—

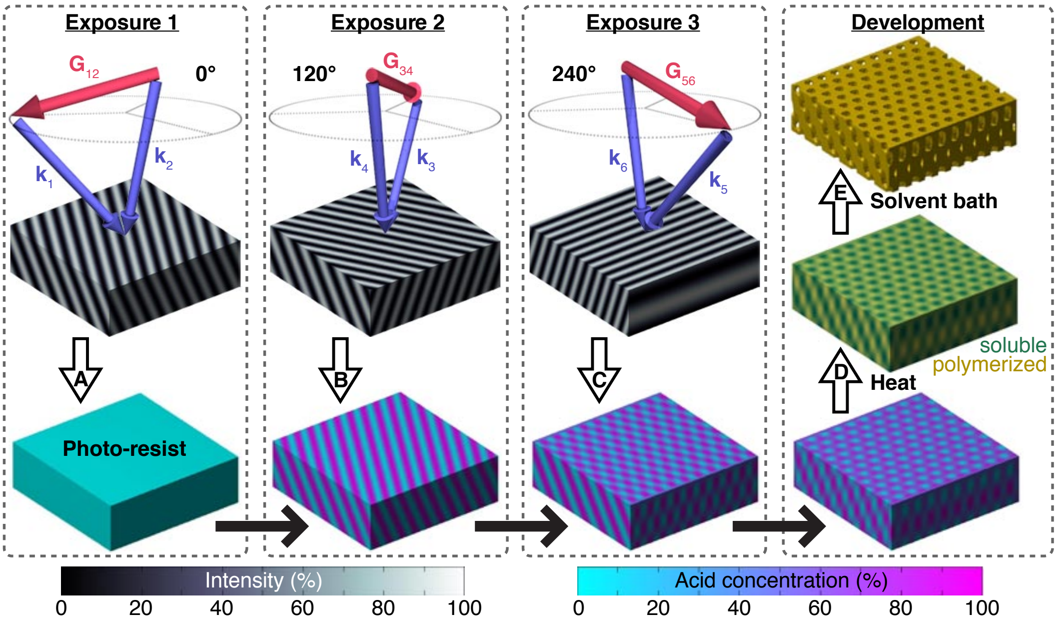

Figure 3.1: Schematic for 3-by-2 holographic lithography. Two simultaneous laser beams with wavevectors $\boldsymbol{k}_n$ and $\boldsymbol{k}_m$ (white interference fringes) expose a negative-tone epoxide photo-resist (SU-8) in three sequential steps (**A**–**C**). At each step the reciprocal lattice vector of the interference pattern, $\boldsymbol{G}_{nm} = \boldsymbol{k}_n - \boldsymbol{k}_m$, is rotated by 120° around the optical axis and adds one spatial dimension to the periodic cumulative optical exposure within the resist. The development procedure renders the exposed photo-resist solid by heating (**D**), removing noncross-linked SU-8 with solvents (**E**), and drying in air.

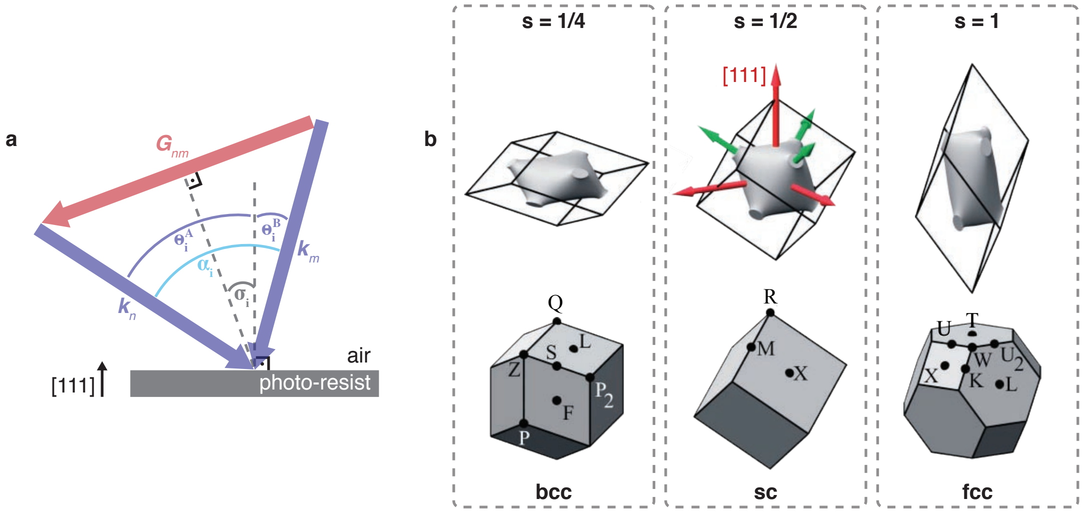

Figure 3.2: Relation between arrangement of the two interfering laser beams and $\boldsymbol{G}_{nm}$ for 3-by-2 beam lithography (**a**). Possible interference patterns (top) and first Brillouin zones (bottom) resulting from this triple exposure by adjusting the scaling factor s from Equation (3.2) (**b**). **b** adapted from [178].

the only constraint is $a \geq \lambda_{\mathrm{beam}}/2$. By keeping α fixed and by tuning the angle, σ, between the bisector of both beams and the surface normal of the photo-resist ([111]-axis), the orientation of $\boldsymbol{G}_{nm}$ and therefore the symmetry of the photonic crystal can be additionally adjusted. Apart from the fcc structure, beam arrangements can this way lead to rhombohedral structures with body-centered cubic (bcc) and simple cubic (sc) translational symmetry by simply distorting the interference pattern (Figure 3.2 b).

A developed photonic crystal structure shrinks by 40% along the surface normal of its substrate after photo-resist development. The three-by-two beam technique can be used to pre-compensate this shrinkage [178]. Both angles that determine the beam geometry within the photo-resist can be adjusted to compensate for the stretch ($s > 1$) or shrinkage ($s < 1$) of the fcc interference pattern with respect to the [111]-axis [178],

$$\sigma = \arctan\left(\frac{1}{2\sqrt{2}s}\right) \, , \qquad \alpha = 2 \arcsin\left(\frac{\lambda_{\mathrm{beam}}\sqrt{8+1/s^2}}{6an_{\mathrm{r}}}\right) \, , \tag{3.2}$$

where n_{r} is the refractive index of the photo-resist ($n_{\mathrm{r}} = 1.6$ for SU-8 resist). Both angles are also corrected for refraction occurring at the air to photo-resist interface by using Snell's law,

$$\sigma_{\mathrm{i}} = \frac{\theta_{\mathrm{i}}^{\mathrm{A}} - \theta_{\mathrm{i}}^{\mathrm{B}}}{2} + \theta_{\mathrm{i}}^{\mathrm{B}} \, , \qquad \alpha_{\mathrm{i}} = \theta_{\mathrm{i}}^{\mathrm{A}} - \theta_{\mathrm{i}}^{\mathrm{B}} \, , \tag{3.3}$$

where

$$\theta_{\mathrm{i}}^{\mathrm{A}} = \arcsin\left(\frac{n_{\mathrm{r}}}{n_{\mathrm{i}}}\sin\left(\sigma + \frac{\alpha}{2}\right)\right) \, , \qquad \theta_{\mathrm{i}}^{\mathrm{B}} = \arcsin\left(\frac{n_{\mathrm{r}}}{n_{\mathrm{i}}}\sin\left(\sigma - \frac{\alpha}{2}\right)\right) \, , \tag{3.4}$$

and n_{i} are the angles of each beam (A and B) with respect to the sample normal and refractive index of incident medium respectively (see Figure 3.2 a). The different transmission coefficients for both s-polarized beams need also to be considered by the Fresnel equations,

$$T_{\mathrm{A}} = 1 - \left[\frac{\sin(\theta_{\mathrm{i}}^{\mathrm{A}} - \sigma - \alpha/2)}{\sin(\theta_{\mathrm{i}}^{\mathrm{A}} + \sigma + \alpha/2)}\right]^2 \, , \qquad T_{\mathrm{B}} = 1 - \left[\frac{\sin(\theta_{\mathrm{i}}^{\mathrm{B}} - \sigma + \alpha/2)}{\sin(\theta_{\mathrm{i}}^{\mathrm{B}} + \sigma - \alpha/2)}\right]^2 \, . \tag{3.5}$$

3.2.2 Optical Apparatus for Holographic Exposures

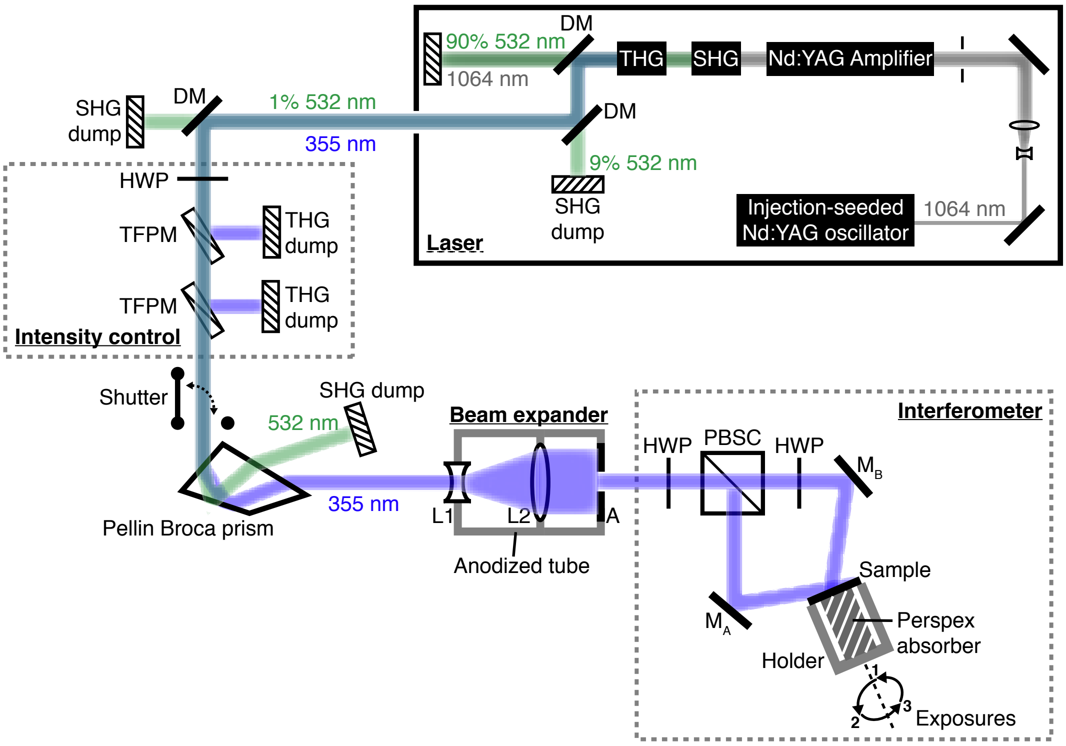

Figure 3.3: Optical apparatus for holographic three-by-two beam exposures. An injection-seeded Nd:YAG laser contained second (SHG) and third harmonic generating (THG) crystals that produced frequency tripled pulses at 355 nm. Dichroic mirrors (DM) and Pellin Broca prism diverted 532 nm and 1064 nm pulses into beam dumps. The 355 nm pulse energy was adjusted by a half-waveplate (HWP) combined with thin-film polarizing mirrors (TFPM). A 5× beam expander consisted of a diverging lens (L1) and a converging lens (L2) and was followed by a 10 mm aperture (A). The interferometer was composed of a polarizing beam splitter cube (PBSC) that directed a pulse onto two mirrors (M_A and M_B), each reflecting the pulse onto the sample. The sample, mounted on a Perspex cylinder, was contained in a sample holder and was exposed to the interfering pulses by releasing the shutter in between 120° turns around the surface normal of the sample.

The optical apparatus for holographic three-by-two beam exposures consisted of a commercial injection-seeded Nd:YAG laser (Continuum Precision II Powerlite 8000), a set of optical components that allowed control of the laser intensity, and an interferometer that created the desired interference pattern (Figure 3.3). The laser produced temporally coherent 6 ns pulses at 355 nm by frequency tripling an amplified pulse at 1064 nm with second and third harmonic generating crystals. Dichroic mirrors separated the 355 nm pulses from the 532 nm and 1064 nm pulses. Since each dichroic mirror transmitted 10% energy of each 532 nm pulse a Pellin Broca prism was used in order to completely separate them from 355 nm pulses. The pulse energy at the laser output was adjusted to ≈60 mJ by adjusting the time delay between the two flash lamps pumping the Nd:YAG oscillator and Nd:YAG amplifier. A half-wave plate combined with thin-film polarizing mirrors enabled fine adjustment of the transmitted 355 nm pulse energy to 47.5 mJ for the holographic exposure of the photo-resist. A mechanical shutter was synchronized to the 10 Hz repetition rate of the laser and allowed selection of one pulse for each exposure. A custom-built beam expander, which consisted of a ⌀0.5" plano-concave lens with 20 mm focal length and a ⌀1" plano-convex lens with 100 mm focal length, expanded the laser beam fivefold from its 9 mm $1/e^2$-diameter (see section 3.4 on page 51). An internally threaded, anodized ⌀1" aluminum tube contained both lenses and absorbed light that was over-filling the converging lens. A 10 mm wide aperture behind the beam expander prevented clipping of the laser pulse at optical components within the interferometer layout and was large enough to keep diffraction modulations of the intensity profile at minimum (see calculated Fresnel diffraction pattern in Figure 3.8 on page 51). The interferometer was composed of a polarizing beam splitter cube that directed the reflected and transmitted pulses onto two different mirrors ($\mathrm{M_A}$ and $\mathrm{M_B}$) along paths A and B, each targeting the pulse at the photo-resist in order to interfere. A half-wave plate before the polarizing beam splitter cube determined the energy ratio, $P_\mathrm{B}/P_\mathrm{A}$, between transmitted pulse and reflected pulse. The half-wave plate behind the polarizing beam splitter matched the polarization of the transmitted pulse to the one of the reflected pulse. The short pulse length prevented susceptibility to mechanical vibrations during the holographic exposure, but simultaneously provided a long enough coherence length of ≈2 m, which was significantly larger than the 50 cm optical path length of the two interferometer arms A and B. The sample resided on a Perspex cylinder which was index matched with mineral oil and absorbed both 355 nm pulses that traversed the sample. Sample and Perspex cylinder were held in a sample holder which was attached to a magnetic mount that allowed 120° turns around the the surface normal of the sample. The orientation of the sample normal with respect to the bisector of mirrors $\mathrm{M_A}$ and $\mathrm{M_B}$ was adjusted to the angle $\sigma = 21°$ so that the interference pattern in the resist featured the correct symmetry (Equation 3.3). The angle between both interfering beams was adjusted to $\alpha = 35.2°$ and resulted in the lattice constant $a = 592\,\mathrm{nm}$ of the interference pattern within the photo-resist (Equation 3.3). The power ratio $P_\mathrm{B}/P_\mathrm{A} = T_\mathrm{A}/T_\mathrm{B} \approx 0.95$ was adjusted to correct the powers of the two beams transmitted into the photo-resist (from Equations 3.5). During exposure photo-resist samples were masked by a brass sheet which comprised a ⌀5 mm aperture. This provided samples in the form of disks with a 5 mm diameter after development that was convenient for making solar cell devices. The sample holder could be loaded with circular ⌀22 mm coverslips (No 1.5, Agar-scientific) or 14 mm square (Pilkington TEC 15) substrates for test purposes and photovoltaic applications respectively.

3.2.3 Photo-resist Chemistry and Processing

Photo-resist Preparation

The photo-resist that was used for holographic lithography was made by casting a film of photo-resist in between a glass coverslip and a non-stick glass coverslip which was silanized with dichlorodimethylsilane. A 14 mm square fluorine-doped tin oxide glass (Pilkington TEC 15) substrate was cleaned (see Appendix E.1) and served as transparent conducting electrode for photovoltaic purposes (see Chapter 5). The photo-resist film consisted of 25%(w/w) negative-tone epoxide photo-resist (SU-8 or Shell Epon Resin) dissolved in ethyl-acetate and supplemented with 3% aryl sulfonium photoacid generator (PAG). After drying the cast film at 120°C for 90 min and cooling at ≈0.3°C/min to room temperature, the resulting photo-resist contained 90% SU-8 and 10% PAG.

SU-8 is an oligomer of n monomers which contain two epoxy groups each (Figure 3.4 a) [185]. Chromatography measurements by Prof. R. G. Denning [185] show a

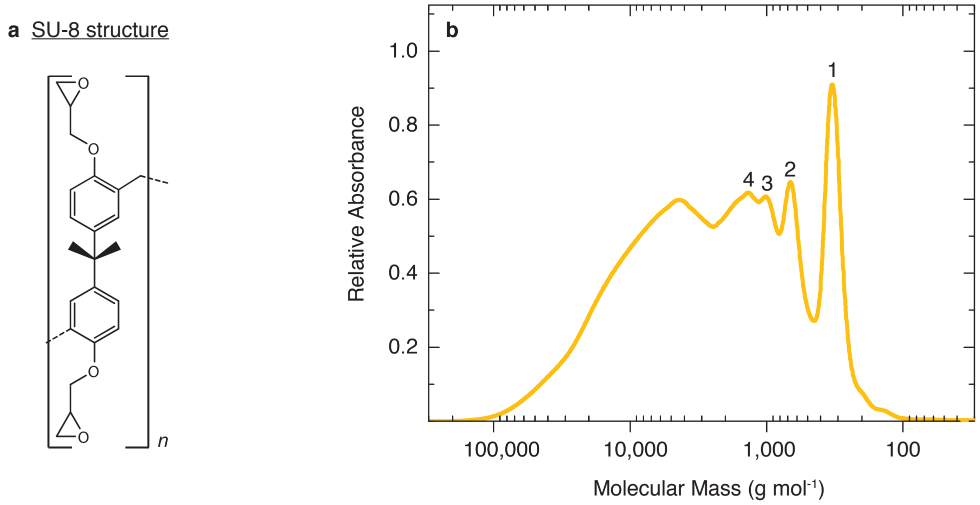

Figure 3.4: The SU-8 structure is an oligomer with n repeats of the shown fragment (**a**). Molecular mass distribution by size exclusion chromatography of a commercial SU-8 batch (**b**). Distinguishable SU-8 oligomers are labeled with n, the number of involved fragments. Adapted from ref. [185].

broad mass distribution ranging from a large proportion of light oligomers, $1 \leq n \leq 10$, to small quantities of heavy oligomers, $10 < n \lesssim 300$, (Figure 3.4 b). The name SU-8 originated from the over-simplified assumption that it is a purely tetrameric compound, $n = 4$, [186].

Photo-resist during Holographic Exposure

The PAG photo-initiator in the photo-resist is used to initiate chemically amplified polymerization of SU-8 in response to absorption of the laser pulse. The absorption cross-section and concentration of the initiator were such that a 10-100 µm thick film was polymerized by a single laser pulse from the holographic interferometer (Section 3.2.2 on page 45). On exposing the photo-resist with the laser interference pattern, the PAG molecules dissociate and generate protons (H^+), described as photoacid, within the exposed volume (Figure 3.5). This means that the structure of the photonic crystal already resides as a latent image in form of the photoacid distribution within the photo-resist (Figure 3.1).

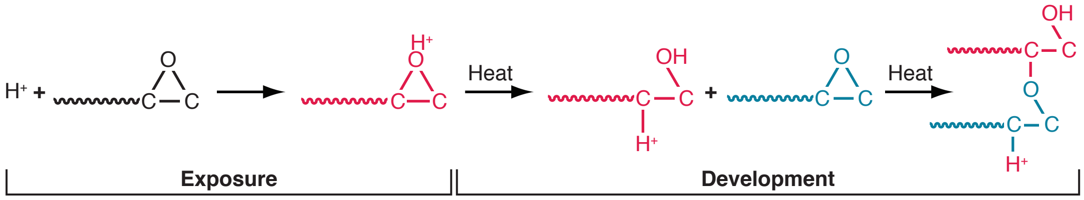

Figure 3.5: Photoacid (H^+) that originates from the PAG in the exposed photo-resist initiates the reaction from epoxy groups to hydroxyl groups. Polymerization of the photo-resist occurs in form of cross-linking the hydroxyl groups of separate SU-8 oligomers via ether bonds.

Photo-resist Development

In order to render this image solid, the exposed photo-resist was developed by heating it for one hour at 55°C. Heat causes the SU-8 oligomers to polymerize in regions of high enough photoacid concentration. In these regions the SU-8 epoxy groups react to hydroxyl groups that form ether bonds with other oligomers and establish the cross-links (Figure 3.5). In the regions of low photoacid density the polymer remains soluble and was dissolved in a 15 min bath of the solvent propylene glycol methyl ether acetate (PGMEA). In order to remove the PGMEA from the resulting polymer photonic crystal, it was slowly replaced with 150 ml propan-2-ol by using a burette (method described in Appendix B on page 114). After an additional 5 min bath in propan-2-ol the developed photonic crystal templates were dried in air.

3.3 Under-coats

Casting a photo-resist directly onto the glass or fluorine-doped tin oxide substrate resulted in delamination of the photonic crystal template after development. Preparing a 1 µm thick film of fully polymerized SU-8 between substrate and cast photoresist solved this delamination problem (Figure 3.6 a). The procedure for developing these so-called SU-8 under-coats was very similar to the one for cast resists (Section 3.2.3). Resist under-coats were produced by spin-coating photo-resist with 20% PAG onto the substrate at 3000 rpm, drying this film at 85°C for 20 min, exposing with an

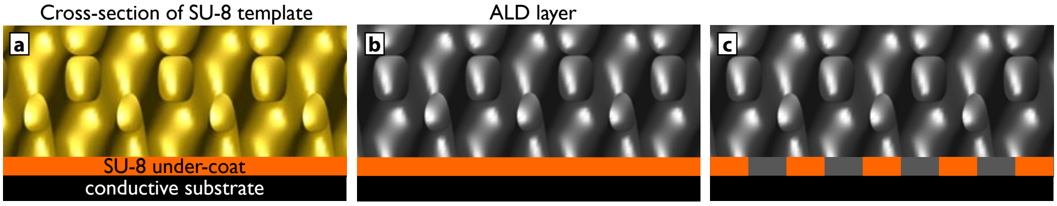

Figure 3.6: Solid SU-8 under-coats prevent delamination of photonic crystal templates from the substrate during development (**a**), but also obstruct contact between substrate and ALD layer (**b**). A patterned SU-8 under-coat solves this problem (**c**).

ultra-bright 364 nm UV i-LED (Nichia NCCU033) at 260 mW/cm^2 for 5 min, baking the resist at 95°C for 15 min, and soaking it in PGMEA for 5 min, followed by a short rinse in propan-2-ol.

Even though these solid under-coats prevent delamination of the template they are inconvenient for photovoltaic applications, because they act as insulators that hinder charge carriers reaching the substrate electrode (Figure 3.6 b). Patterning the under-coat by holographic lithography enabled the attachment of the template to the substrate as well as simultaneously enhancing the charge transport to the electrode (Figure 3.6 c). The 3-by-2 laser beam exposure simply replaced the UV-LED exposure, all other preparation steps were kept as just described. Using the 3-by-2 beam geometry for photonic crystal templates a 1 μm thickness of the photo-resist corresponds approximately to the height of one unit cell. Hence, the patterned under-coat turned out to be a porous two-dimensional structure instead of a three-dimensional photonic crystal (Figure 3.7 a).

In order to compare the impedance of the patterned and solid under-coats qualitatively, they were immersed in a bath of iodine/iodide electrolyte which allowed measurement of the current between the conductive fluorine-doped tin oxide substrate and the platinized top electrode (Figure 3.7 b). A Whatman® Laboratory sealing film acted as a spacer between the two electrodes. This assembly was sealed by melting the sealing film at 90°C. Current-voltage measurements with a Keithley 2400 sourcemeter demonstrated that the solid under-coat acted as an insulator (Figure 3.7 c). The patterned under-coat showed considerably less impedance than the solid under-

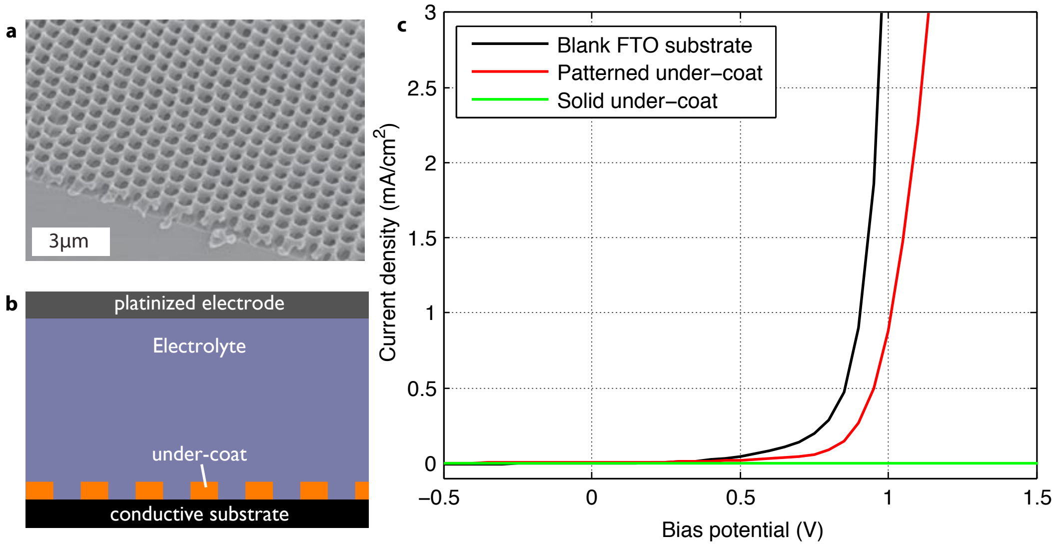

Figure 3.7: SEM image [187] of patterned under-coat (**a**) and schematic of assembly for current measurements (**b**). J-V curve for solid and patterned under-coates compared to blank substrate (**c**).

coat, almost as low as the blank substrate, so that it was utilizable for photovoltaic applications.

3.4 Laser Profile

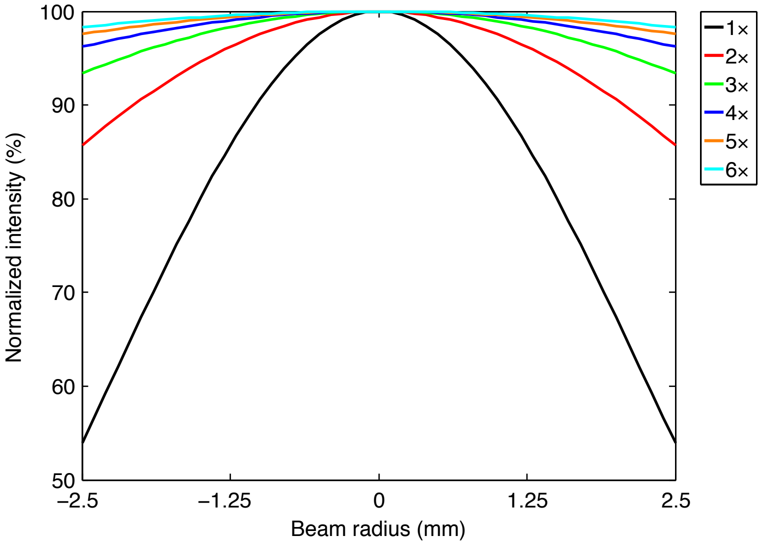

Figure 3.8: Gaussian profiles across the 5 mm sample diameter for various expansions of a laser beam with $1/e^2$-radius of $w = 4.5\,\mathrm{mm}$.

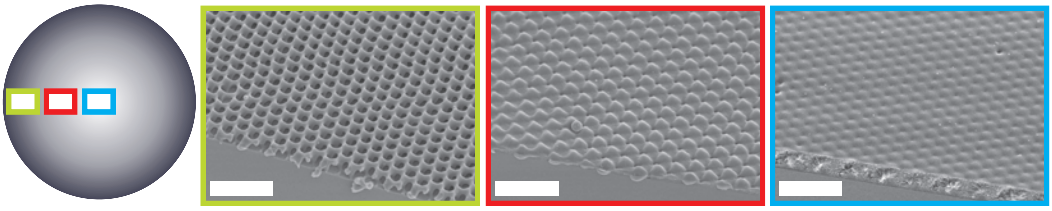

Figure 3.9: SEM micrographs [187] illustrate over-polymerization of an under-coat from its periphery towards the center—scale bars are 3 µm. Micro-graphed regions are marked green, red, and blue in the depicted top-view of the under-coat (left).

The patterned under-coats and photonic crystal templates were limited by a mask to 5 mm in diameter. Plotting Gaussian intensity profiles, $I(r) = I_0 \exp(-2r^2/w^2)$, of a beam with a $1/e^2$-radius of $w = 4.5$ mm (corresponding to the beam without a beam expander) shows that over a beam radius $r = 2.5$ mm the Gaussian profile of the 9 mm wide unexpanded laser pulse varied by 50% (Figure 3.8). This varying laser intensity distribution produced photonic crystal templates and patterned under-coats with non-uniform polymer/air fill-fractions. Scanning electron micrographs demonstrated that patterned under-coats were porous along the periphery where the laser intensity was 50% (Figure 3.9, green). But towards the center where the pulse energy reached maximum under-coats were over-polymerized (Figure 3.9, blue). In order to reduce this variation in porosity, the laser beam was expanded by a factor of five with a Galilean telescope (as already depicted in Figure 3.3 on page 45). The resulting intensity profile of the expanded laser beam drops by less than 5% across the 5 mm sample diameter, which is a tenfold increase in uniformity compared to the unexpanded laser beam (Figure 3.8).

The clear aperture of the optics within the interferometer limited the radius of the iris behind the beam expander to $a = 5$ mm (see Section 3.2.2 on page 45). In order to determine the impact of diffraction at the iris on fluctuations of the intensity profile the intensity distribution of the Fresnel diffraction pattern was calculated at a distance $z = 64$ cm from the iris to where the photo-resist sample resided. For this purpose the Gauss-quadrature algorithm in MATLAB was used to compute the light field at the

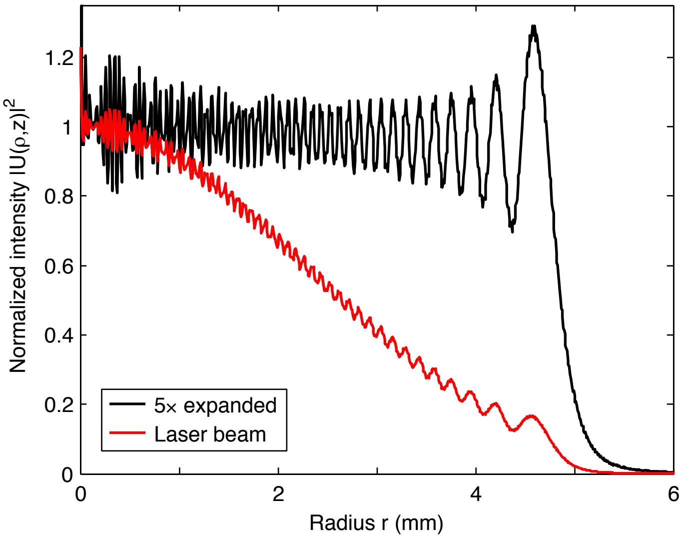

Figure 3.10: Calculated Fresnel diffraction patterns observed at a distance $z = 64\,\mathrm{cm}$ from a 10 mm wide, circular aperture at which a laser beam with radius $a = 4.5\,\mathrm{mm}$ and a 5× wider beam diffract.

photo-resist from the Fresnel diffraction integral [188],

$$U(\rho, z) = i2\pi N(z)\mathrm{e}^{-i2\pi z/\lambda}\mathrm{e}^{-i\pi N(z)\rho^2}\int_0^1 U_a(\rho_a)J_0(2\pi N(z)\rho\rho_a)\mathrm{e}^{-i\pi N(z)\rho_a^2}\rho_a\,\mathrm{d}\rho_a\ , \quad (3.6)$$

where $N(z) = a^2/\lambda z$, $U_a(\rho_a) = \sqrt{I(a\rho_a)}$, $J_0(x)$, $\rho_a = r_a/a$ and $\rho = r/a$ are the Fresnel number, the incident laser profile at the aperture, the zero-order Bessel function and the normalized radii at the aperture and photo-resist respectively. The intensity profile at the photo-resist was then calculated from the modulus squared of the light field, $|U(\rho, z)|^2$. The Fresnel diffraction pattern for a 5× expanded laser beam shows that the intensity profile is modulated between 10–20%, significantly more than the unexpanded laser beam (Figure 3.10).

The pulse profile at the laser output is itself not smooth as a result of diffraction at the optics within the laser, which illustrates the beam profile that was recorded on a fluorescent screen with a CCD camera by Mr. H. Bharaj [189] (Figure 3.11, left). The calculated modulations from diffraction at the aperture were quantitatively compared to the fluctuations originating from the laser optics by performing a nonlinear least-squares fit of a bivariate Gaussian model, $f(x, y)$, to the recorded image, img(x,y), of the pulse profile (Figure 3.11, center). Above a 25% threshold of the Gaussian peak

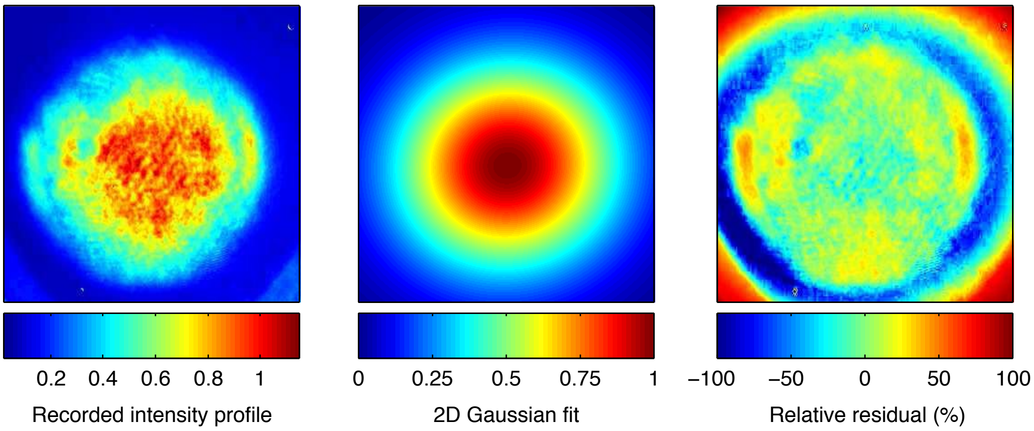

Figure 3.11: Nonlinear least-squares fit of a bivariate Gaussian model to a recorded laser pulse profile. The relative residual shows the magnitude of the fluctuations around the Gaussian fit. Recorded pulse profile from Mr. H. Bharaj [189].

the relative residual,

$$\frac{\mathrm{img}(x,y) - f(x,y)}{\mathrm{img}(x,y)}\,, \tag{3.7}$$

reveals fluctuations around the Gaussian fit between 10–50% (Figure 3.11, right). In comparison to the calculated Fresnel diffraction pattern above, this means that diffraction of a 5×-expanded laser pulse at the aperture in the described layout does not add significantly to the fluctuations of the intensity profile in the photo-resist. Scanning electron micrographs of a patterned under-coat that was produced with the 5× beam expander showed approximately uniform porosity throughout from the periphery to the center of the film (similar to Figure 3.9, green). The use of a 5× beam expander with a 10 mm wide aperture before the interferometer therefore has no significantly deteriorative effect on the uniformity of produced photonic crystal microstructures.

3.5 Photo-resist Reinforcement

As already outlined in Chapter 1 and Section 2.2, photonic crystal microstructures were used as templates for photovoltaic devices. The techniques applied in order to fabricate these devices involved material depositions above 100°C at which the porous structure of the polymer templates collapsed. The reason for this collapse is that at

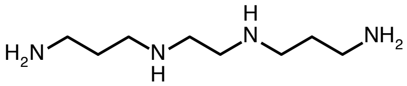

Figure 3.12: N,N'-Bis(3-aminopropyl)ethylenediamine (BAPEN).

modest exposure doses ≈65% of the epoxy groups in the photo-resist remain unreacted during template development [185].

The fact that commercial epoxy resin adhesives can be hardened with amines at room temperature [190] and begin to degrade above 200°C [191] led to the idea of including a hardening step with an amine compound in the development procedure (e.f. Section 3.2.3 on page 49). This hardening step consisted of soaking the photoresist in a solution of PGMEA supplemented with the polyfunctional amine N,N'-Bis(3-aminopropyl)ethylenediamine (BAPEN) after the 15 min PGMEA bath of the photo-resist, followed by slow solvent exchange with propan-2-ol. BAPEN enabled the residual noncross-linked SU-8 epoxy groups in the developed photo-resist to interconnect via its amine groups (Figure 3.12). Infrared spectroscopy and optical scattering techniques were utilized in order to optimize the dwell time of the photo-resist and amount of BAPEN. SEM allowed to draw conclusions about structural changes of the photonic crystal microstructure.

3.5.1 Infrared Spectroscopy of Reinforced SU-8 Structures

Since SU-8 epoxy groups are consumed in the cross-linking reaction with BAPEN, the vibrational resonance of the epoxy group at a wavenumber of 915 cm^{-1} provides a measure of how much polymer is cross-linked within the photo-resist. Consequently a reduction in the epoxy absorption was expected to be most pronounced for higher BAPEN concentrations and longer dwell times. For this purpose infrared spectroscopy was used to measure the amount of cross-linked polymer within the developed photonic crystal template after the BAPEN treatment. Attenuated total reflectance (ATR) spectroscopy is a well-suited infrared spectroscopy technique, as the absorbing substrate of the template cannot block the incident light. The ATR spectrometer probes the

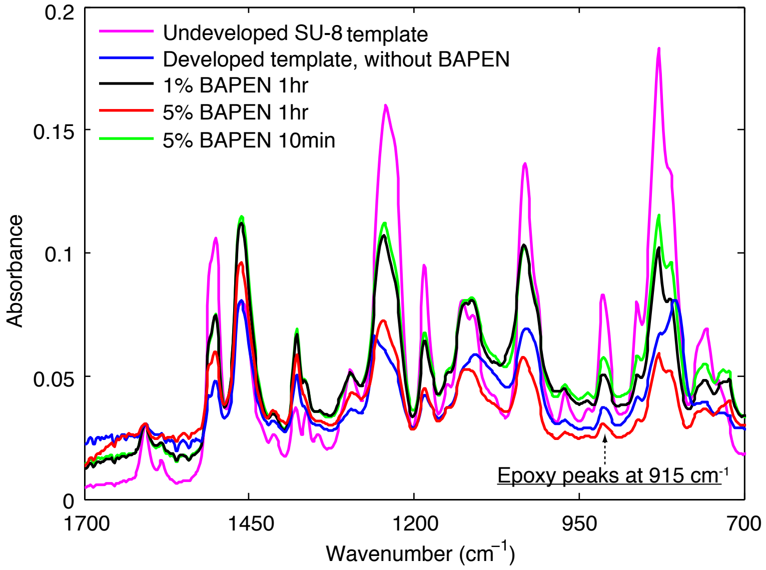

Figure 3.13: Attenuated total reflectance spectra of photonic crystal SU-8 polymer templates. During development the templates soaked for different time periods in PGMEA, which was supplemented with BAPEN at different concentrations. The reduction in the absorption at 915 cm^{-1} corresponds to an increase of polymerized su cross-linked via epoxy groups within the template. The epoxy-peak of the undeveloped template serves as reference, corresponding to the largest possible epoxy-absorption of non-cross-linked SU-8 oligomers.

template using the evanescent field of an infrared beam, which is totally internal reflected at the interface of the template and an ATR crystal. Since the evanescent field in this spectral region only extends to 1–5 µm, the template needs to be in direct contact with the ATR crystal. Whilst ATR spectra showed some evidence of a reduced epoxy absorption at higher BAPEN concentrations and longer dwell times (Figure 3.13), the method has proved to be unreliable. Due to the rough surface of the heated templates, some regions of the sample were not in direct contact to the ATR crystal so that the absorption spectra strongly depended on the position of the template with respect to the ATR crystal. Hence, this technique could not provide reproducible and quantitative measurements of cross-linked polymer within the template.

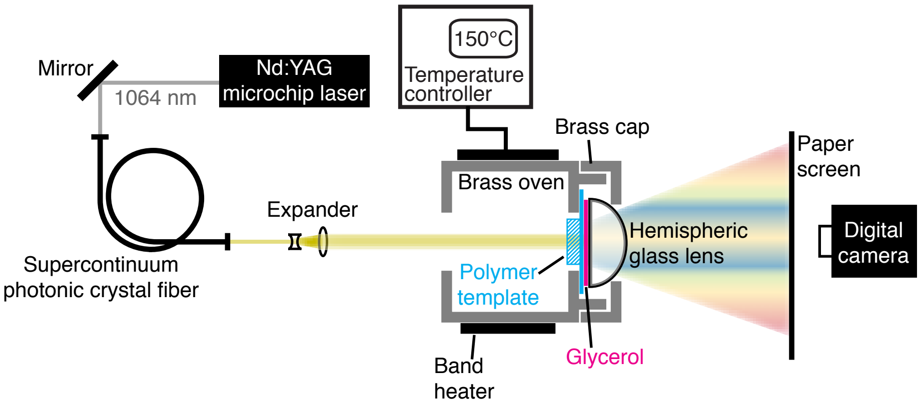

Figure 3.14: Schematic of apparatus for recording diffraction patterns of photonic crystal templates during a heating process.

3.5.2 Optimizing Photo-resist Reinforcement

For this reason a different approach was developed to monitor structural changes of BAPEN reinforced photonic crystal SU-8 templates. This approach was based on the detection of the diffraction pattern from a laser beam incident on the photonic crystal template. The diffraction pattern acted as indicator for the microstructure of the template so that its disappearance signaled the collapse of the microstructure during the heating process.

In order to measure the temperature at which a photonic crystal polymer template collapsed for different conditions of BAPEN treatment, an optical apparatus was assembled which was used to image the diffraction pattern of the template during a temperature ramp (Figure 3.14). The assembly utilized a Supercontinuum photonic crystal fiber (NKT Photonics, SC-5.0-1040) as light source, which was pumped at 1064 nm by a passively Q-switched Nd:YAG microchip laser (NKT Photonics, NP-10620-100). The spectrally continuous and broad light beam from the Supercontinuum fiber was expanded to a $1/e^2$-diameter of $\approx$3 mm and diffracted at the polymer template. The diffraction pattern was projected onto a paper screen and recorded by a digital color camera. The template was mounted in a custom-made brass oven which enabled controllable heating of the sample with a band heater (RS, XQ-012-RS) and temperature controller (2216e Eurotherm and K-type thermocouple). A fitted brass cap held the sample in place and ensured that the substrate of the template was

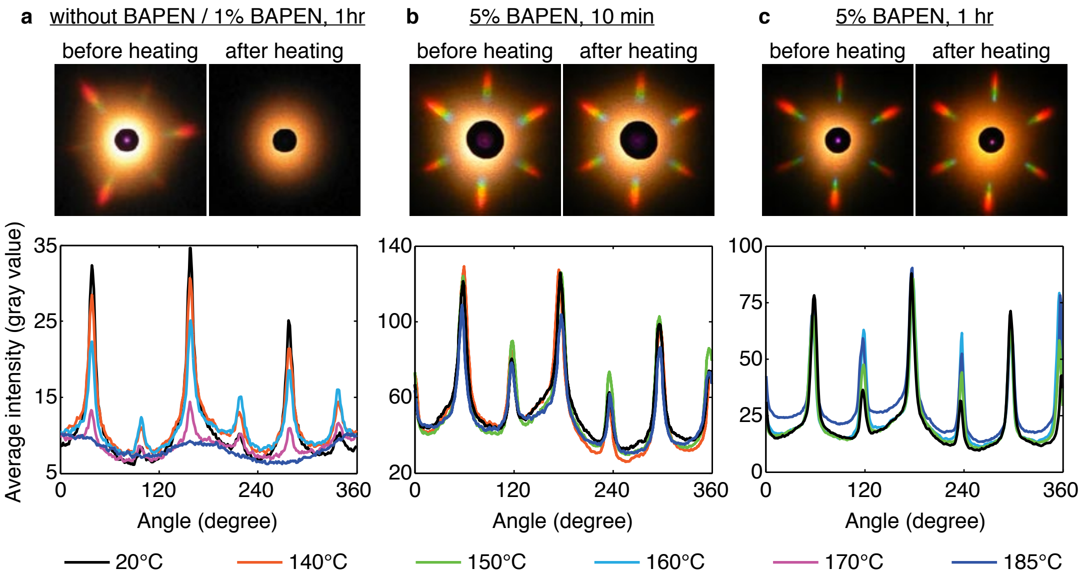

Figure 3.15: Diffraction patterns, and their radially averaged intensity, from photonic crystal polymer templates developed in 1% BAPEN for 1 hr (**a**, similar result without BAPEN), in 5% BAPEN for 10 min (**b**), as well as 1 hr (**c**). Diffraction patterns were recorded during temperature ramp from 20°C to 185°C.

in permanent contact with a hemispheric glass lens in order to couple out diffracted light that would otherwise be totally internally reflected at the substrate-air interface. The lens was index-matched with glycerol, with a boiling point of 290°C that is well above 185°C—the maximum temperature of the heat experiments. The advantage of this method was that it allowed structural changes of photonic crystal templates to be followed in real time. This enabled optimization of the BAPEN concentration and dwelling time for the development of heat resistant photonic crystal SU-8 templates.

Templates were produced by soaking them in PGMEA supplemented with 1% and 5% BAPEN, in which they dwelled for 10 min or 1 hour. These templates were each mounted in the described apparatus and diffraction patterns recorded during a temperature ramp from 20°C to 185°C. The intensity of each pattern was radially averaged in order to compare the diffraction patterns of each template quantitatively. The average intensity of the diffraction pattern of the template that was treated in 1% BAPEN started to decrease above 100°C and disappeared completely at 185°C (Figure 3.15 a). A polymer template that was produced without BAPEN by following the conventional development (in Section 3.2.3 on page 49) demonstrated the same

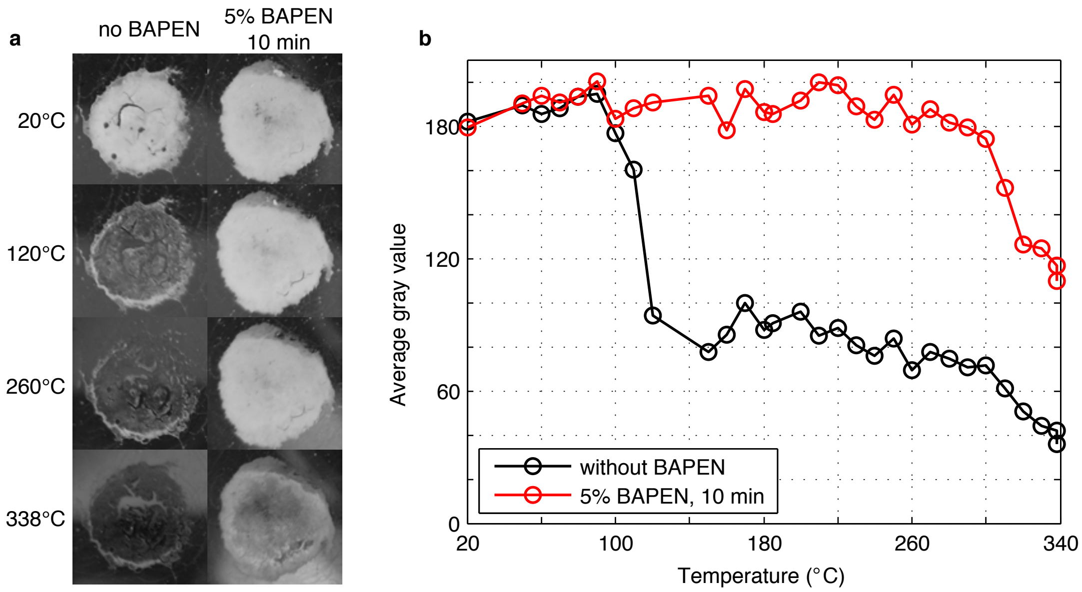

Figure 3.16: Photographs (**a**) of photonic crystal microstructures which were heated from 20°C to 338°C and averaged gray values of the images with respect to temperature (**b**). The lines serve as guides to the eye.

behavior. In contrast, the diffraction patterns of the templates that were treated in 5% BAPEN for 10 min and 1 hr persisted over the whole temperature range (Figure 3.15 b and 3.15 c). For the template that dwelled 1 hr in BAPEN, the proportion of directly transmitted light around the center of the diffraction pattern increased at 185°C (Figure 3.15 c), which suggested that low spatial-frequency features started to emerge within the template. This template also exhibited a change of symmetry of the intensity distribution within its diffraction pattern over time, which is difficult to understand. These diffraction experiments show that the development in 5% BAPEN strengthened the photonic crystal templates against heat within the sampled temperature range. All photonic crystal templates were thenceforth reinforced by soaking in 5% BAPEN for 10 min.

3.5.3 Photographs of Heated Templates

Since the temperature range of the oven, which was used for the above diffraction measurements, was limited to 185°C it was unfeasible to test the maximum heat resistance of a BAPEN reinforced photonic crystal template. For this purpose the

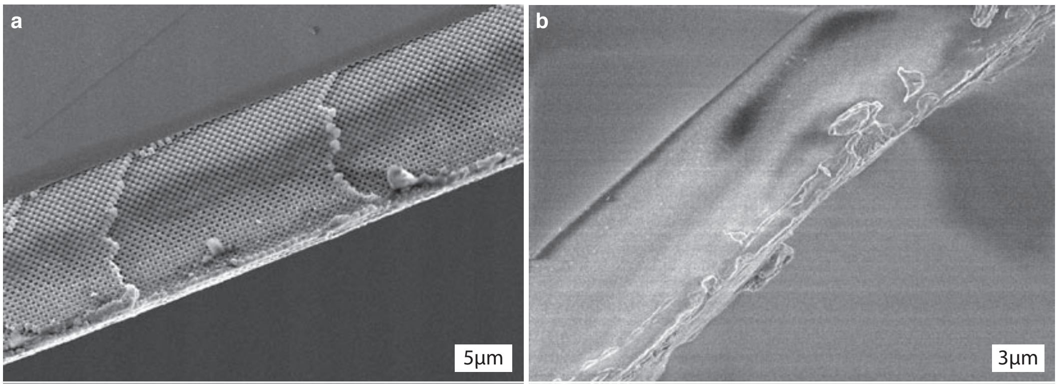

Figure 3.17: Two SEM micrographs [187] depict the side view of two photonic crystal polymer templates after heating to 185°C. One sample contains BAPEN and shows preservation of the template bulk-structure upon heating to 185°C (**a**), whereas the one lacking the cross-linking molecule features a collapse of the bulk structure at 100°C (**b**).

optical appearance of reinforced templates was characterized at a larger temperature range by placing them on a hot-plate and imaging them with a CCD camera during a temperature ramp from 20 to 338°C. Conventional photonic crystal templates lost their white appearance above 100°C where their light-scattering microstructure collapsed (Figure 3.16 a). In comparison, a template that dwelled in 5% BAPEN for 10 min retained its opacity but turned brown, indicating the chemical decomposition of SU-8. The averaged gray-scale values of the recorded photographs as a function of temperature served as a qualitative measure for the porosity of the two microstructures. A drop of the average gray value indicated the moment at which the structure began to collapse. The average gray value for the BAPEN treated template remained approximately constant up to 260°C, whereas for the untreated sample it rapidly dropped around 100°C (Figure 3.16 b).

3.5.4 Structural Characterization with SEM

Templates were heated to 185°C and imaged by scanning electron microscopy (SEM) in order to support the effects of heat and BAPEN treatment on photonic crystal microstructures observed by the above techniques. The SEM images show that the pore-structure in the bulk of the BAPEN-reacted template remained intact (Fig-

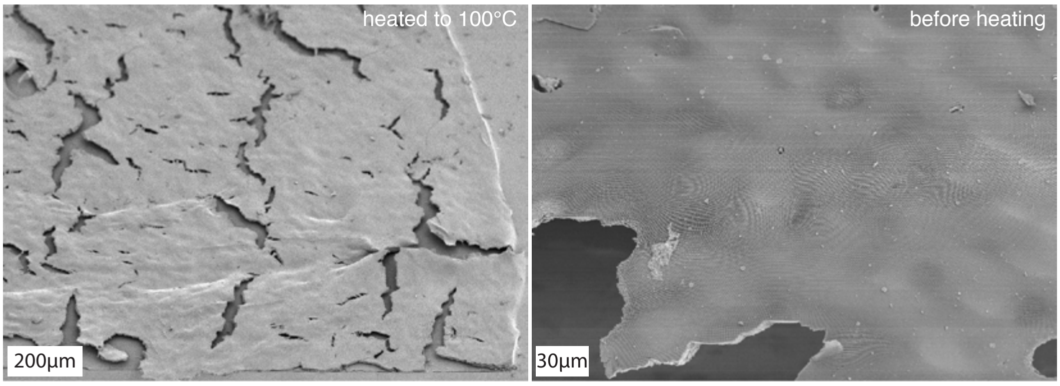

Figure 3.18: SEM images [187] show that elevating the temperature of a photonic crystal polymer structure to 100°C after it dwelled in a 5% BAPEN solution for 10 min resulted in macroscopic cracks (left). These cracks arise from modulations in the SU-8 to air fill fraction, which appear as dark regions in the SEM micrograph before heating (right).

ure 3.17 a) whereas the bulk-structure of a normally developed template completely collapsed (Figure 3.17 b). This confirms the above results from optical characterization (Section 3.5.2 and 3.5.3) and supports the conclusion from infrared spectroscopy that the BAPEN treatment enhances thermal stability of the template by improving cross-linkage of SU-8 in the photo-resist (Section 3.5.1).

However imaging a BAPEN-treated photonic crystal template at a large field of view in the SEM revealed that the features that were responsible for the larger background intensity between the diffraction spots (in Figure 3.15 c) were caused by macroscopic cracks that appeared already after heating the template to 100°C (Figure 3.18, left). The micrograph of a template kept at room temperature shows dark regions on a comparable length scale (Figure 3.18, right). These dark regions appear in parts of the porous microstructure that have a low SU-8 to air fill fraction, because they contain less material from which electrons in the SEM back-scatter. This suggests that the macroscopic cracks develop in regions of low fill fraction where the polymer structure is to weak to withstand the strain arising from thermal expansion of SU-8. The dark regions in the micrograph resemble the speckled fluctuations in the pulse profile at the laser output (as presented in Section 3.4 on page 51). This suggests that the fill fraction fluctuations are a consequence of the laser profile during the holographic exposure.

3.6 Discussion

Holographic lithography, in form of triple two-beam exposure, is a flexible method to produce photonic crystal SU-8 templates with rhombohedral structure on a broad length scale. The templates produced detached from the substrate during development. Patterned under-coats that were produced by exposing thin SU-8 photo-resist pre-layer with the same optical apparatus assisted in fixing the templates to the substrate. A telescope expanded the laser beam fivefold during holographic exposures which enhanced uniformity of the templates and under-coats. Due to their porous structure, these under-coats maintained a continuous path to the substrate. This is a requirement for photonic crystal microstructures serving as templates for fabrication of the proposed photovoltaic heterojunction (Scheme 1 on page 38) because it demands conductive pathways to the underlying substrate, which consists of a transparent conductive oxide. The assembly of the heterojunction involves the deposition of absorbing and charge separating materials on the SU-8 template. The deposition techniques involved demand elevated temperatures above 100°C at which the SU-8 templates collapse. Optical characterization techniques together with infrared spectroscopy and electron microscopy demonstrated that utilizing the polyamine BAPEN during photo-resist development strengthened the templates and prevented a collapse of their periodic bulk-structure up to 260°C. SEM also showed that the fluctuations in the pulse profile at the laser output created modulations of the fill fraction in the developed template, which resulted in macroscopic cracks at 100°C. These cracks are however no hindrance to the use of templates for resulting solar cell devices. They only lower the power conversion efficiency of photovoltaic devices by reducing the internal surface area of the heterojunction. The fabrication of the heterojunction within photonic crystal microstructures involves atomic layer deposition, a deposition technique introduced in the following chapter.

4 Atomic Layer Deposition

4.1 Introduction

Development of the proposed photovoltaic device (Scheme 1 on page 38) requires deposition of thin films of organic or inorganic materials that compose the photovoltaic heterojunction. The techniques used to deposit thin films of various elements and compounds are abundant and range from solution processing such as sol-gel [195] and plating techniques [196; 197] to physical vapor deposition (PVD) approaches [198] such as evaporation, sputtering or molecular beam epitaxy (MBE) [199], and to various chemical vapor deposition (CVD) procedures [200; 201]. All these methods however have difficulties in satisfying the increasing need for conformal thin films on complex three-dimensional structures for photonic and photovoltaic applications and to keep pace with the scaling down of micro-electronic devices [202–204]. A deposition technique called atomic layer deposition (ALD) has proved to be suitable for producing conformal inorganic films with thickness down to a fraction of a monolayer and step coverage as high as 100% in deep trench and hole structures [193; 194; 205; 206] with aspect ratios exceeding 1000 [207] (Figure 4.1).

ALD is a thin-film material growth technique that is closely related to CVD. In CVD, two reactants A and B are present at the same time and form a material product P continuously on a surface: $\mathrm{A} + \mathrm{B} \longrightarrow \mathrm{P}$ [208]. In ALD, this reaction is divided in two sequential half-reactions where each reactant interacts with the surface individually so

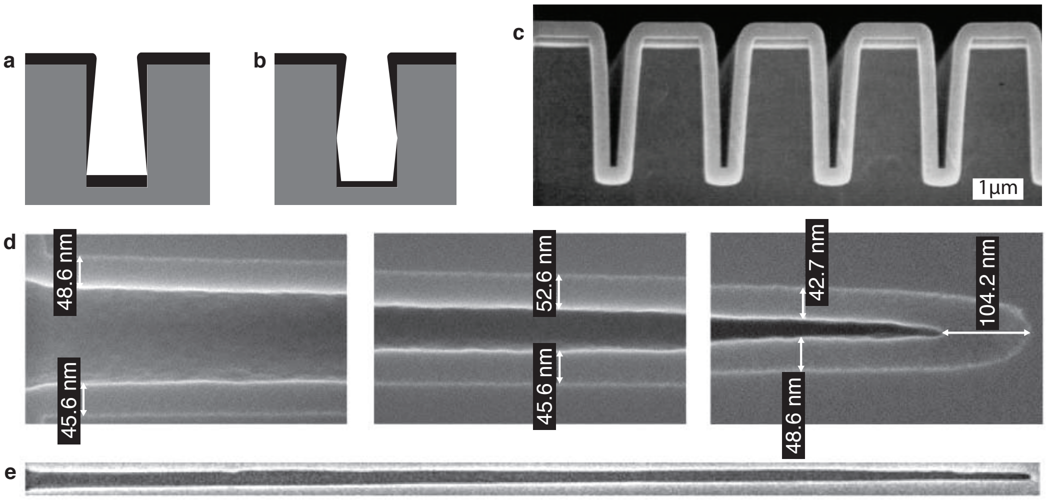

Figure 4.1: Directional depositions such as physical (PDV) or chemical vapor deposition (CVD) produce non-conformal films in high aspect-ratio structures (**a** and **b**, followed schematic in ref. [192]). Electron micrographs showing conformity of films deposited by atomic layer deposition (ALD). In (**c**) 300 nm thick alumina film grown on trench structure (adapted from ref. [193]). In (**d**) silica film in a 7 µm deep hole that is 200 nm wide at top and 100 nm at bottom—cross-section of complete uncoated hole (**e**) shown for illustration (**d** and **e** adapted from ref. [194]).

that the product film forms in a stepwise fashion,

$$\begin{gathered}\text{surface} + \text{A} \longrightarrow \text{surface}{-}\text{A}\\ \text{surface}{-}\text{A} + \text{B} \longrightarrow \text{surface}{-}\text{P}\\ \text{surface}{-}\text{P} + \text{A} \longrightarrow \text{surface}{-}\text{P}{-}\text{A}\\ \text{etc.}\end{gathered} \tag{4.1}$$

This type of deposition was invented independently by a Soviet-Russian group as molecular layering technique in the 1960s [209; 210] and by a Finnish group as atomic layer epitaxy in the 1970s [211; 212]. The widely adopted name atomic layer deposition dates back to the year 2000 and is now commonly used [208]. In the 1980s and 1990s, liquid-phase [213; 214] and electrochemical [215; 216] analogs of ALD were investigated, but in this work only the original gas-phase form of ALD is described.

ALD has been used to grow materials in photonic crystal templates according to Scheme 1. The processes adopted are explained after shortly reviewing the general

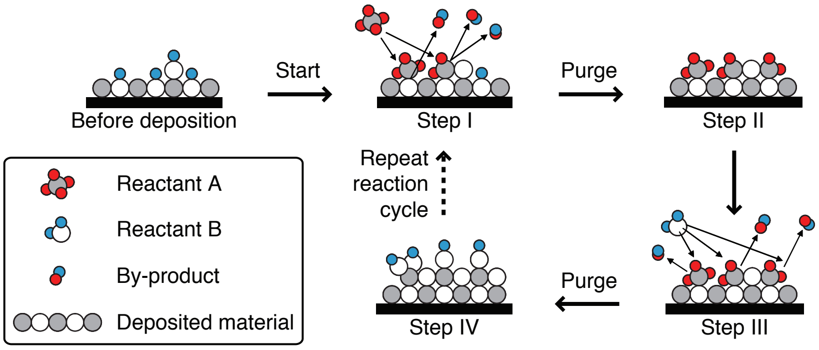

Figure 4.2: Schematic of procedure for one ALD reaction cycle. Adapted from ref. [217].

principles of ALD growth and the type of materials that can currently be produced by ALD (Section 4.2). An ALD apparatus has been built and its properties and precursors characterized (Section 4.3). The apparatus was used to grow metal oxide and metal nitride films on planar substrates, which were tested for uniformity, thickness, crystallinity, and conductivity (Section 4.4). Photonic crystal inverse replicas were successfully produced by depositing these films on photonic crystal templates (Section 4.5).

4.2 ALD Process

4.2.1 ALD Reaction Cycle

As indicated by the reactions (4.1), the growth of material layers by ALD takes place by sequential pulsing of two precursors that undergo self-terminated gas-solid reactions under low pressure. These reactions are separated by inert-gas purges. The following procedure summarizes the ALD growth sequence [204].

(I) Self-terminating reaction of the first precursor (Reactant A).

(II) Purge or evacuation, which removes by-products and non-reacted reactants A.

(III) Self-terminating reaction of the second precursor (Reactant B), which reactivates the surface for the reaction with reactant A.

(IV) Purge or evacuation, which removes by-products and non-reacted reactants B.

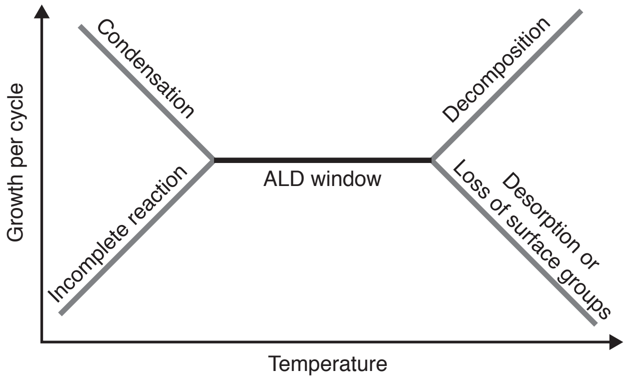

Figure 4.3: Schematic of possible behavior of growth per cycle with respect to temperature illustrates the optimal temperature range for ALD growth—the ALD window. Adapted from ref. [208].

Steps (I)–(IV) in this procedure comprise one ALD reaction cycle (depicted in Figure 4.2). Each ALD reaction cycle adds a certain amount of material onto the surface, defined as growth per cycle, and is repeated until the intended film thickness is reached. A functional ALD reaction cycle requires (i) volatile reactants, (ii) suitable temperature for gas-solid reactions of the reactants, (iii) thermally stable reactants that do not decompose at the processing temperature, (iv) irreversible gas-solid reactions in order to fulfil the criterion of self-termination, and (v) saturation of all reactive surface sites [204]. In the processing temperature range that meets the above requirements for ALD behavior—the so-called ALD window—an adsorbed molecule forms a specific bond by consuming a reactive surface group, i.e. the surface adsorbs not more than a monolayer of the reactant [208]. During this process, which is often called chemisorption, the number of reactive sites on the surface and the steric hindrance of chemisorbed reactants determines the growth per cycle [204]. The dose of reactants and the timing of each step during the ALD cycle need to be adjusted in order to ensure saturation of reactions at all surface sites.

In the ALD window chemisorption is irreversible, but deposition can become reversible and lead to a reduced growth per cycle due to incomplete surface reactions or desorption of reactants if the deposition temperature is below or above the ALD window respectively (Figure 4.3) [204; 218]. For some ALD processes at a temperature outside the ALD window, reactants may condense at the surface in a non-specific

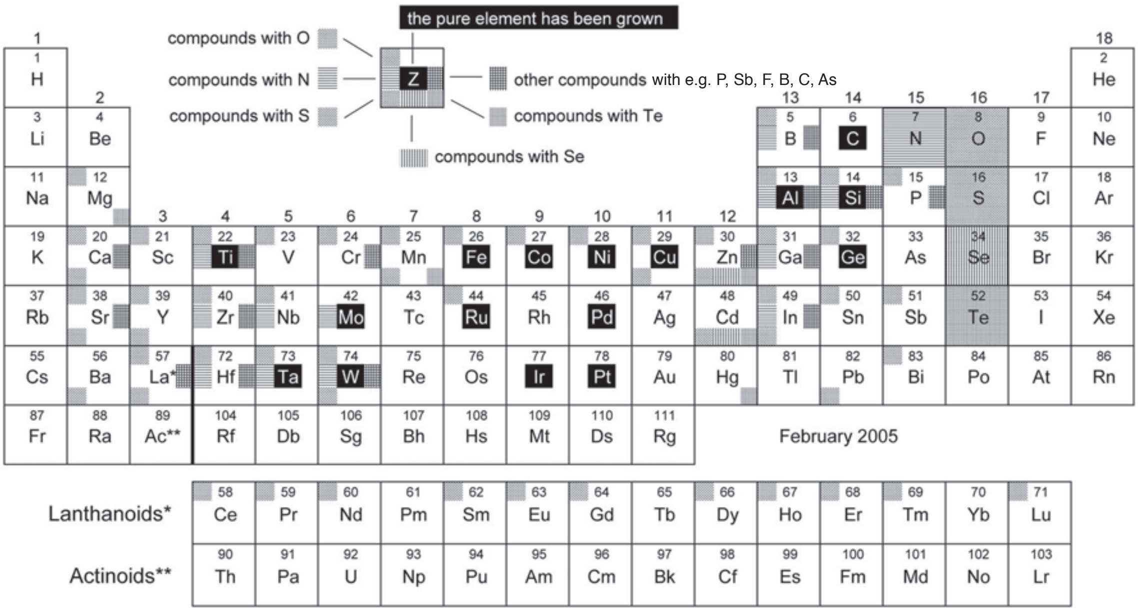

Figure 4.4: Elements and compounds grown by ALD as before 2005. Adapted from [204].

continuous manner or decompose and allow additional reactions so that the growth per cycle increases (Figure 4.3) [204; 208]. Therefore correct adjustment of the processing temperature is essential for conformal ALD growth. The type of substrate also determines conformity of ALD growth. For example in ALD on silicon [219; 220] or carbon structures such as carbon nanotubes [221; 222] nucleation of some ALD processes is impeded, inducing island-growth [223] and non-linear growth per cycle, due to lack of reactive surface sites. After multiple ALD cycles these islands grow together and form a continuous film [208; 223]. Functionalization of the substrate can facilitate ALD nucleation and improve film roughness [221; 222; 224]. ALD growth on a variety of polymers is also non-uniform during the first few cycles, because precursors diffuse into the porous polymer where they are trapped and react in a CVD fashion before conformal growth starts [225].

4.2.2 Established ALD Processes

The ALD processes that have been developed to grow materials are abundant. The biggest class of materials grown by ALD are compounds of inorganic materials, which are largely oxides but also numerous nitrides, sulfides, selenides, tellurides, some fluorides, phosphides or phosphates and more complex compounds (Figure 4.4) [204; 208]. A survey shows that the reactants used for growing these materials are mainly pure elements, halides or metal-organic reactants, which establish CVD processes too [204]. Elements are versatile reactants for some ALD processes, but their low vapor pressure, tendency to reversible adsorption at the surface, and their limitations in self-terminating reactions restrict their choice. Halides are reactive and thermally stable above 800°C so that diverse compounds can be grown from them. However their reaction by-products with hydrogen-containing reactants tend to be corrosive and can etch film constituents and create impurities of e.g. 1.6 at.% hydrogen in HfO_2 films [204]. Metal-organic precursors exist with numerous organic ligands and due to their reactivity and large diversity numerous compounds can be deposited [204; 226]. The thermal stability of metal-organic reactants between 150–300°C remains moderate and they are prone to cause impurities [204]. For some ALD processes films grown from alkoxides, β-diketonates, alkylamides, and silylamides contain e.g. hydrogen impurities of 8 at.%, 2 at.% , 6 at.%, and 20 at.%, respectively [204].

Apart from inorganic compounds, single-element materials, such as metals, can be grown by ALD processes (Figure 4.4) [204; 207; 208]. These processes are often based on reactions with radicals from a plasma source, because these radicals are more reactive compared with merely thermal ALD reactions [192; 208; 227]. Plasma enhanced ALD was also used to grow films of compounds. Aluminum oxide Al_2O_3 has been deposited at room temperature this way [228] and possessed even better electrical properties than thermally grown films [229]. Plasma enhanced ALD is advantageous for fabricating ALD films on thermally fragile substrates. It is, however, limited in growing films on substrates with high aspect-ratios as it produces less conformal films [208].

Recently ALD processes for growth of organic compounds have been developed. The technique is widely referred to as molecular layer deposition (MLD) [208; 230; 231]. Yoshimura et al. [232] used MLD to make wires of different organic compounds that composed a tether of quantum dots. Furthermore thin and conformal polymer films have been produced by vapor phase polymerization (VPP) and oxidative chemical vapor deposition (oCVD) where a CVD process is combined with oxidants [233; 234]. By varying the deposition temperature during oCVD growth of thin PEDOT films, the electrical properties such as work function and electrical conductivity could be systematically controlled [235; 236], especially convenient for photovoltaic applications.

4.2.3 ALD Processes used in this Work

In order to deposit titanium dioxide TiO_2, zinc oxide ZnO, aluminum doped zinc oxide ZnO:Al, and zirconium nitride Zr_3N_4 by ALD on photonic crystal templates (as proposed in Section 2.3), established ALD processes were used and are summarized in the sections below.

Titanium dioxide TiO_2

Titanium dioxide films were grown from the precursors water H_2O and titanium tetra chloride $TiCl_4$ following the studies by Ritala et al. [237] and Aarik et al. [238]. This ALD process is well established and dates back to one of the early ALD experiments by Russian researchers in the 1960s [204; 209]. During each reaction cycle $TiCl_4$ reacts with hydroxyl groups on the surface by ligand exchange and forms hydrogen chloride HCl as by-product. H_2O then removes the remaining chloro-groups by re-hydroxylation. The two surface reactions during the exposure of each precursor are [239]

$$\begin{gathered}\text{surface}-(\mathrm{OH})_2 + \mathrm{TiCl_4} \longrightarrow \text{surface}-\mathrm{O_2TiCl_2} + 2\,\mathrm{HCl}\\ \text{surface}-\mathrm{O_2TiCl_2} + 2\,\mathrm{H_2O} \longrightarrow \text{surface}-\mathrm{O_2Ti(OH)_2} + 2\,\mathrm{HCl}\ .\end{gathered}$$

Zinc oxide ZnO

The organo-metallic precursor diethylzinc $Zn(C_2H_5)_2$ and water are a very common combination for producing zinc oxide films [240; 241]. In the ALD reaction cycle, $Zn(C_2H_5)_2$ interacts with hydroxyl groups on the surface and forms the by-product ethane by ligand exchange. The resulting ethyl groups on the surface are displaced by re-hydroxylation with H_2O. The sequential surface reactions for each precursor are [242]

$$\begin{aligned} \text{surface}{-}\text{OH} + \text{Zn}(\text{C}_2\text{H}_5)_2 &\longrightarrow \text{surface}{-}\text{O}{-}\text{Zn}{-}\text{C}_2\text{H}_5 + \text{C}_2\text{H}_6 \\ \text{surface}{-}\text{O}{-}\text{Zn}{-}\text{C}_2\text{H}_5 + \text{H}_2\text{O} &\longrightarrow \text{surface}{-}\text{O}{-}\text{Zn}{-}\text{OH} + \text{C}_2\text{H}_6 \ . \end{aligned}$$

Aluminum oxide Al_2O_3

Lujala et al. [243] first suggested ALD growth of Al doped ZnO from organo-metallic precursors. The ZnO:Al ALD process is based on the ZnO process above, but periodically replaces one ZnO cycle with a Al_2O_3 ALD process [240; 243]. In this impurity cycle the precursor trimethylaluminium $Al(CH_3)_3$ reacts with the hydroxyl surface groups by ligand exchange and the water precursor re-hydroxylates the surface similar to the processes above. The two surface reactions for $Al(CH_3)_3$ and H_2O during the impurity cycle are [218]

$$\begin{aligned} \text{surface}{-}\text{OH} + \text{Al}(\text{CH}_3)_3 &\longrightarrow \text{surface}{-}\text{O}{-}\text{Al}(\text{CH}_3)_2 + \text{CH}_4 \ , \\ \text{surface}{-}\text{Al}{-}\text{CH}_3 + \text{H}_2\text{O} &\longrightarrow \text{surface}{-}\text{Al}{-}\text{OH} + \text{CH}_4 \ \ . \end{aligned}$$

Zirconium nitride Zr_3N_4

Following the ALD process established by Becker et al. [244], zirconium nitride Zr_3N_4 was deposited from the metal alkylamide tetrakis(dimethylamido)-zirconium $Zr(N(CH_3)_2)_4$ and ammonia NH_3. Studies of surface reactions of group IV metal alkylamides with ammonia suggest that both precursors in the ALD cycle produce Zr_3N_4 by transamination [245–250]. In this process, $Zr(N(CH_3)_2)_4$ reacts with amine groups on the surface by ligand exchange and forms the by-product dimethylamine $(CH_3)_2NH$. NH_3 then eliminates the remaining dimethylamine groups on the surface. The two transamination surface reactions during exposure of each precursor are [247–250]

$$\begin{aligned} \text{surface}{-}(\text{NH}_2)_2 + \text{Zr}(\text{N}(\text{CH}_3)_2)_4 &\longrightarrow \text{surface}{-}(\text{NH})_2\text{Zr}(\text{N}(\text{CH}_3)_2)_2 + 2\,(\text{CH}_3)_2\text{NH} \\ \text{surface}{-}(\text{NH})_2\text{Zr}(\text{N}(\text{CH}_3)_2)_2 + 2\,\text{NH}_3 &\longrightarrow \text{surface}{-}(\text{NH})_2\text{ZrNH}_2 + 2\,(\text{CH}_3)_2\text{NH} \ . \end{aligned}$$

4.3 ALD Apparatus and Properties

4.3.1 ALD Apparatus

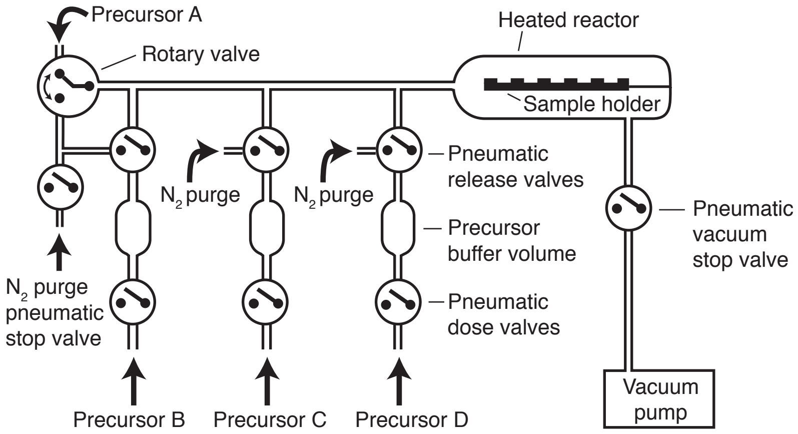

Figure 4.5: Schematic of custom-made ALD apparatus that I use to deposit films of aluminum doped zinc oxide, titanium dioxide and zirconium nitride into the bulk of photonic crystal SU-8 templates. The setup allows sequential release of up to four precursors into the reaction chamber under continuous purge of nitrogen (N_2) via the rotary valve (precursor A) and three pneumatic release valves (precursors B–D).

For the ALD processes introduced above, a custom-made ALD apparatus has been constructed in collaboration with Prof. R. G. Denning [251] and Mr. H. Bharaj [252] (see parts list and schematic diagrams in Appendix C on page 116). The ALD apparatus principally consists of precursor reservoirs, a reaction chamber, and a manifold that introduces precursors sequentially into the reaction chamber via a two-position gas chromatography valve (rotary valve), precursor buffer volumes and pneumatic valves that are remotely controlled by solenoid drivers (Figure 4.5 and 4.6). The manifold sits in an oven that can be heated up to 100°C. An electric fan circulates hot air from heating elements around the manifold. This controls the manifold temperature and prevents condensation of precursors within the manifold before they reach the reaction chamber. The precursor reservoirs are either kept in a precursor box at room temperature or they can be connected directly to the manifold in the oven, which controls the precursor vapor pressure by its temperature (precursor B in Figure 4.6). The pneumatic dose valves fill the precursor buffer volumes. A rotary vane vacuum

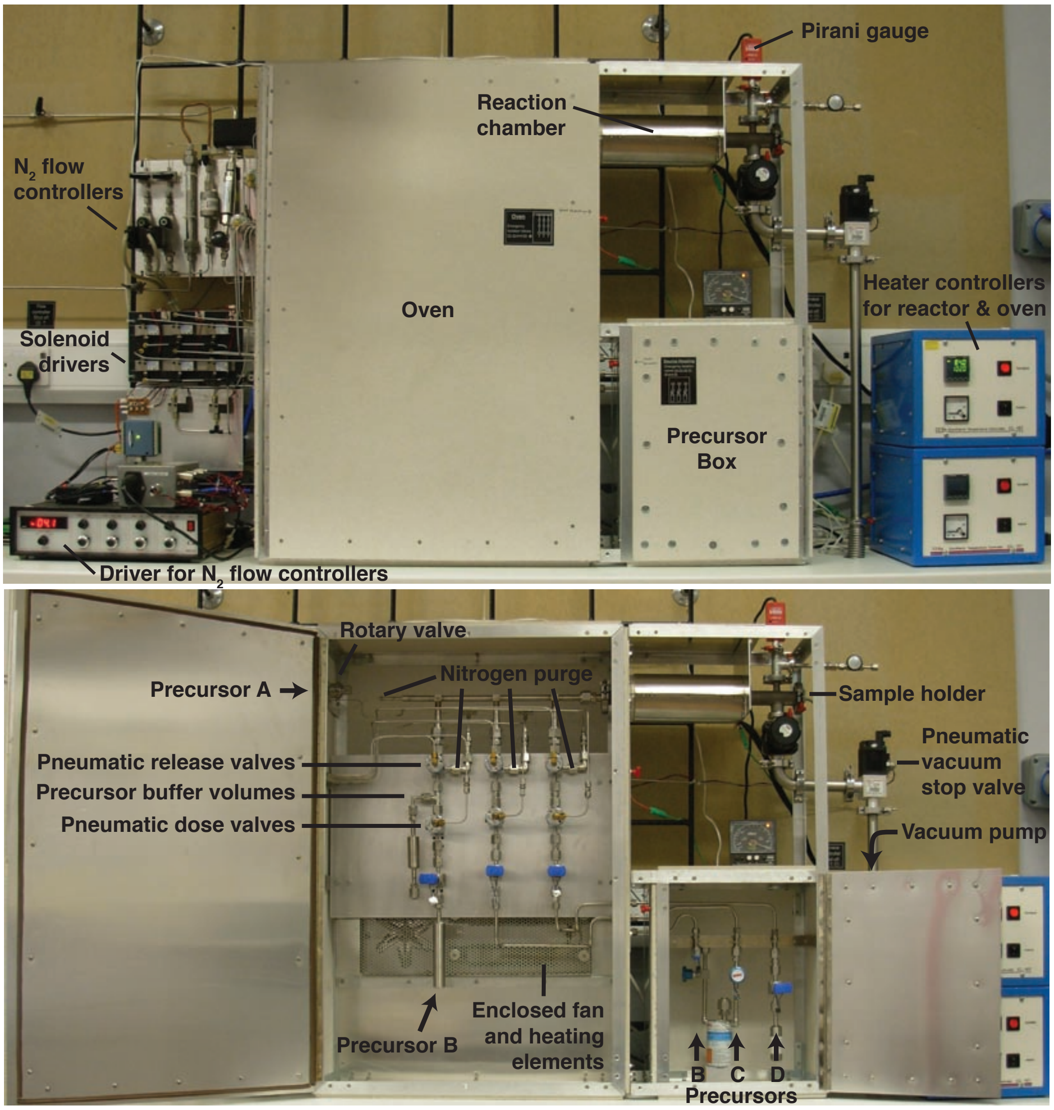

Figure 4.6: Photographs of completed ALD apparatus.

pump keeps the base pressure in the reaction chamber (0.35 mbar) below the vapor pressure of the gaseous precursors (>1 mbar) in the buffer volume so that they can effuse into the reactor (see Table 4.1 on page 75). Together precursor vapor pressure, size of the buffer volumes, and manifold temperature define the reactant dose that is released by the pneumatic release valve into the reactor (see Equation (4.2) in Section 4.3.2). Band heaters around the reaction chamber control the temperature of the enclosed sample holder between 20–250°C. Since the inert reaction chamber is made of a stainless steel tube with poor thermal conductivity ($16\,\mathrm{W\,m^{-1}\,K^{-1}}$), a copper enclosure ($400\,\mathrm{W\,m^{-1}\,K^{-1}}$) was fabricated, which distributes the heat from the band heaters more uniformly along the reactor tube. Probing the temperature of the copper enclosed reactor with a thermocouple showed a reduction of the temperature difference between both reactor ends from >10°C to <1°C. The pneumatic N_2 purge stop valve and the pneumatic vacuum stop valve isolate the reactor volume from the continuous nitrogen flow and vacuum pump and keep the precursor in the reactor for a chosen time until the reaction at the substrate in the sample holder completes.

4.3.2 Precursor and Deposition Properties

Precursor dose

All hot surfaces in the reactor are coated by the deposited material. These surfaces include sample substrates, sample holder, and reactor walls with a total surface area of $A_\mathrm{t} \approx 350\,\mathrm{cm}^2$. In order to ensure complete coverage of this area, precursor doses were adjusted so that they were equivalent to at least 2 monolayers per cycle (Table 4.1 on page 75). The precursor buffer volume V_b, manifold temperature T_m and vapor pressure p_v determine the molar precursor dose in the reactor,

$$S = \frac{n}{A_\mathrm{t}} = \frac{p_\mathrm{v} V_\mathrm{b}}{R T_\mathrm{m} A_\mathrm{t}} \ , \tag{4.2}$$

where n and R are amount of precursor and gas constant respectively.

Timing for precursor dose

Precursors with molar mass M flow into and out of the precursor buffer volume V_b through a cross-section A_b. The minimum opening time of the buffer fill and release valves depends on the vapor pressure equilibration time t_e of the precursors, which can be estimated from the rate of effusion,

$$\frac{n}{t_\mathrm{e}} = J_\mathrm{b} A_\mathrm{b} \ , \tag{4.3}$$

where the molar flux of molecules through the aperture A_b is given by kinetic theory [253],

$$J_\mathrm{b} = \frac{p_\mathrm{v}}{\sqrt{2\pi M R T_\mathrm{m}}} \ . \tag{4.4}$$

The equilibration time results in

$$t_\mathrm{e} = \sqrt{\frac{2\pi M}{R T_\mathrm{m}}} \frac{V_\mathrm{b}}{A_\mathrm{b}} \tag{4.5}$$

and for all our precursors it is less than 100 ms (see Table 4.1). An opening time of 1 sec was used for the buffer fill and release valves, chosen well above the precursor pressure equilibration time.

Timing for precursor exposure

The duration for which the pneumatic nitrogen purge stop valve close and the vacuum stop valve holds the precursors in the reactor determines the precursor exposure in the reaction chamber. During their exposure, precursors need to be able to diffuse in time t_d over a mean-distance $\langle x \rangle \approx 1\,\mathrm{cm}$ to the surface of the sample substrate. For a Brownian precursor particle with collision diameter d and collision cross-section $\sigma = \pi d^2$ the diffusion time in the reactor at temperature T_r is determined by ([253], chapter 21.4)

$$t_\mathrm{d} = \frac{\pi \langle x \rangle^2}{4D} \ , \tag{4.6}$$

using the diffusion coefficient

$$D = \frac{2}{3\sigma p_\mathrm{r} N_\mathrm{A}} \sqrt{\frac{R^3 T_\mathrm{r}^3}{\pi M}} \ . \tag{4.7}$$

The precursor diffusion times for the used precursors are in the range $t_\mathrm{d} \approx 1$–100 ms (see Table 4.1). Hence, the length of time for which both the pneumatic nitrogen purge stop valve and the pneumatic vacuum stop valve close at each cycle was kept at 1 s for all depositions in order to allow sufficient time for termination of ALD reactions.

Deposited material	**Titanium dioxide**		**Aluminium doped zinc oxide**			**Zirconium nitride**	
	TiO_2		**ZnO:Al**			**Zr_3N_4**	
Reactor temperature T_r (°C)	100		160			175	
Precursors	**titanium tetrachloride**	**water**	**diethylzinc**	**water**	**trimethyl aluminium**	**tetrakis (dimethylamino) zirconium**	**ammonia**
Formula	$TiCl_4$	H_2O	$Zn(C_2H_5)_2$	H_2O	$Al(CH_3)_3$	$[Zr(N(CH_3)_2)_4]_2$	NH_3
Collision diameter d (Å)	5.24	2.06	9.34	2.06	6.24	15.26	2.22
Collision cross-section $\sigma = \pi d^2$ (nm^2)	0.86	0.13	2.74	0.13	1.22	7.32	0.15
Molar weight M (g/mol)	189.68	18.02	123.49	18.02	72.09	535.16	17.03
Vapor pressure p_v at 20°C (mbar)	13.3	23.4	16.2	23.4	11.6	1.3	1300
Manifold temperature T_m (°C)	50	50	50	50	50	70	70
Buffer volume V_b (ml)	2.85	2.85	3.55	2.85	2.85	29.40	0.05
Buffer cross-sectional area A_b (cm^2)	0.17	0.17	0.17	0.17	0.17	0.17	0.01
Diffusion coefficient D (cm^2/s)	82	1723	40	2155	117	8	2009
Precursor dose S (nmol/cm^2)	**4.0**	**7.1**	**6.1**	**7.1**	**3.5**	**3.9**	**6.5**
Precursor dose S (monolayers)	**6**	**2**	**26**	**2**	**7**	**44**	**2**
Equilibration time t_e (ms)	**4**	**1**	**4**	**1**	**2**	**61**	**0.3**
Diffusion time t_d (ms)	**10**	**0.5**	**20**	**0.4**	**7**	**104**	**0.4**
Diffusion time t_s (ms)	**2**	**0.5**	**2**	**0.6**	**1**	**32**	**0.01**

Table 4.1: Physical properties of precursors for ALD of titanium dioxide, aluminium doped zinc oxide, and zirconium nitride. Precursor collision diameters, d, were estimated by the covalent atomic radii (from ref. [254]) of the elements that compose each precursor molecule. Note that a monolayer of the precursor dose is defined as a close-packed array of reactant molecules on the surface and not as a layer of chemically bound (chemisorbed) molecules.

Gordon et al. [205] also showed that the time for precursors saturating the surface of structures is proportional to their aspect ratio squared,

$$t_{\mathrm{s}} = \frac{S\sqrt{2\pi M R T_{\mathrm{r}}}}{p_{\mathrm{v}}} \left(1 + \frac{9}{32}a + \frac{3}{32}a^2\right) \ , \tag{4.8}$$

where the aspect ratio is defined as the ratio of the surface area in the bulk and the area of the hole through which the precursor has to diffuse, $a \equiv A_{\mathrm{bulk}}/A_{\mathrm{hole}}$. This means that the saturation exposure of precursors in the reactor depends largely on the structure of the template if its aspect ratio is large. The photonic crystal templates used in this thesis have an aspect ratio on the order of $a \approx 100$ (see roughness factor in Section 5.3.3 on page 94). In this case, t_{s} for the precursors is 32 ms and less (see Table 4.1), which is small compared to the chosen 1 s precursor hold time in the reactor.

4.4 Characterization of Deposited Films

4.4.1 Uniformity of ALD Films

In order to verify uniformity of thickness and refractive index of deposited films on all substrates along the sample holder, zirconium nitride was deposited by following the ALD process outlined on page 70. Deposition temperature and timing of the ALD cycle are summarized in Table 4.2 on page 78. Constructive and destructive interference within a thin zirconium nitride film deposited on the sample holder create bands of different color, similar to an etalon. Since the color varies with film thickness, this effect was used as a convenient tool to qualitatively test thickness uniformity of zirconium nitride films on the ALD sample holder and to optimize the sample holder design.

The first sample holder provided a bevelled surface with five pockets each containing a 22 mm silica cover-slip substrate. An ALD run with 5 sec nitrogen purge time per cycle revealed an irregular coloration of the sample holder, suggesting a non-uniform Zr_3N_4 deposition (Figure 4.7 a). Increasing the purge time to 10 sec slightly

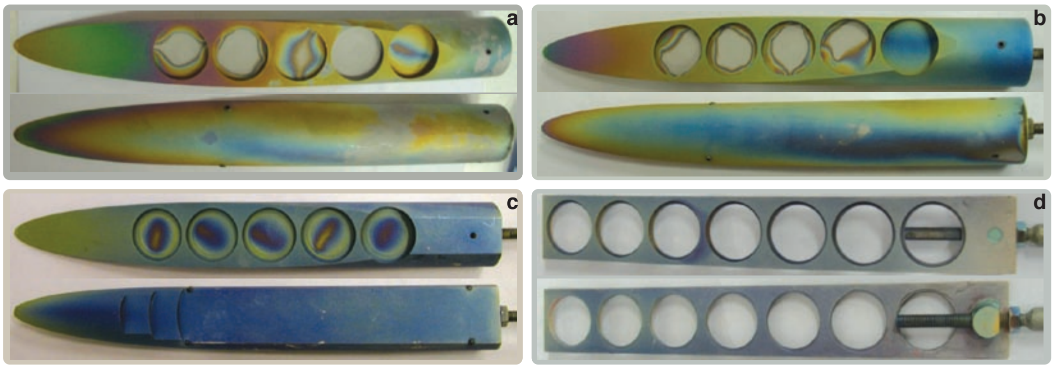

Figure 4.7: Top and bottom view of various sample holders that were coated with 300 ALD cycles of Zr_3N_4. (**a**) bevelled aluminum sample holder with 5 sec and (**b**) 10 sec long nitrogen purges at each ALD cycle. (**c**) beveled aluminum sample holder with less impedance to gas flow using 10 sec purge. (**d**) copper sample holder frame with very low gas flow impedance using 10 sec purge.

improved uniformity of Zr_3N_4 growth (Figure 4.7 b). This suggested the occurrence of chemical vapor deposition (CVD) instead of ALD where the nitrogen flow is too short to fully purge the reactor so that ammonia still reacts with the Zr-compound from the preceding precursor pulse. Since further increasing the purge time would unnecessarily prolong the ALD run time, the impedance of the sample holder to the gas flow was reduced by lowering its height. This resulted in an almost completely uniform deposition (Figure 4.7 c). The coloration of the sample pockets however made obvious that precursor molecules were trapped underneath the substrate. For this reason, a sample holder frame which provided minimal impedance to the gas flow was produced and prevented trapping of vapor molecules by holding the substrates only on a 2 mm edge so that film growth occurred equally on both sides. The resulting Zr_3N_4 deposition looked very uniform (Figure 4.7 d). This sample holder was used for all subsequent depositions.

4.4.2 Thickness of ALD Films and Growth per Cycle

In order to determine the uniformity of deposited films for all ALD processes introduced in Section 4.2.3, material films were produced of various thickness on flat coverslip substrates. The conditions for all ALD processes are summarized in Table 4.2.

Deposited material	**Zr_3N_4**	**TiO_2**	**ZnO**	**ZnO:Al**
Reactor temperature (°C)	175	100	200	200
Precursor temperature (°C)	70	20	20	20
Manifold temperature (°C)	70	50	50	50
Buffer fill & release time (s)	1	1	1	1
Precursor hold time (s)	1	1	1	1
Purge time (s)	10	5	20	20
Impurity every # cycle	–	–	–	20
Measured growth per cycle (Å)	2.9	0.56	2.1	1.9
Literature growth per cycle (Å)	1.2 [244]	0.4–1.2 [237; 238]	2.0 [240]	1.9 [240]
Measured refractive index	2.2	2.33	1.9	1.75
Literature refractive index	3.2 [255]	2.32 [238]	2.0 [256]	1.95 [256]

Table 4.2: ALD routine for each of the deposited films. Measured ALD growth rate and refractive index at 632 nm in comparison to literature values (references in square brackets). ZnO:Al films were compared to literature values for 4 wt% aluminum doped zinc oxide.

Dr. R. Jacobs [257] determined the thickness and refractive index of the ALD films by ellipsometry measurements. The ellipsometry measurements showed a difference in film thickness of less than 1% for substrates distributed across the sample holder. This confirmed the above qualitative result of uniform film growth in photographs of the sample holder (Figure 4.7).

The ellipsometry measurements of each material film also allowed calculation of the refractive index and growth per cycle of each ALD process. Growth per cycle and refractive indices of all materials except Zr_3N_4 were comparable to values reported in the literature (see Table 4.2). Rutherford backscattering experiments on Zr_3N_4 films by Becker et al. [244] showed that the Zr_3N_4 ALD process is susceptible to oxygen contaminants in the ALD reactor, which result in oxygen impurities in the bulk of the material and a lower refractive index. According to infrared spectroscopy measurements by Prof. R. G. Denning [258], the ammonia precursor feed contained 1‰ water contaminations. Unfortunately these contaminations could not be eliminated after evacuating and purging the ammonia feed with nitrogen. The ammonia was purified with a custom-made drying tube that contained 5 g of 3Å molecular sieves (beads, Sigma-Aldrich 20858-2) and that had a capacity to absorb 1 mbar water vapor in 20 liters of ammonia gas at 1 bar. The drying tube was followed by a NH_3 gas purifier (SAES Pure Gas, MC1-702) that is capable of removing water contaminants to less than 1 ppb. However, the growth per cycle was still more than twice as high as for ALD processes producing pure films [244] and the refractive index of the produced Zr_3N_4 films remained too low (Table 4.2). This indicates other possible impurities in the films.

4.4.3 Crystallinity of ALD Films

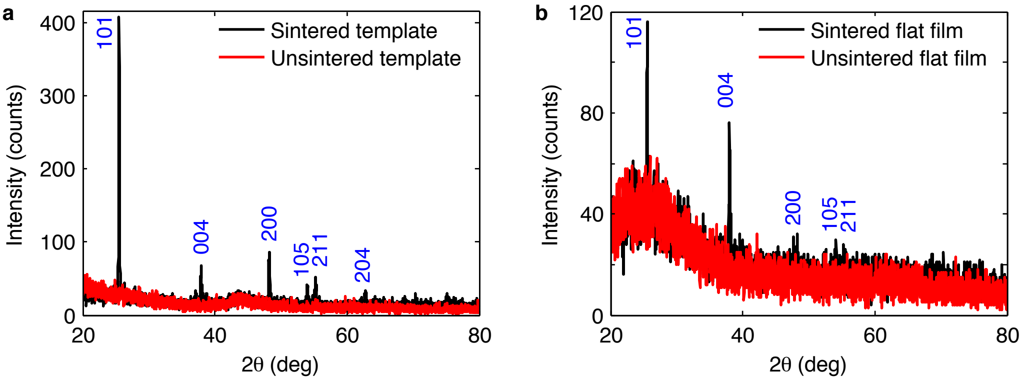

Figure 4.8: X-ray diffraction patterns of 400 nm thick ALD layer of sintered (black) and non-sintered (red) TiO_2 on a photonic crystal template (**a**) and flat glass substrate (**b**). Blue numbers represent Miller indices for crystal planes of anatase.

X-ray diffraction (XRD) measurements, performed by Dr. R. Gunning [259], confirmed the tetragonal and hexagonal structures of anatase and zincite for the TiO_2 and ZnO ALD films respectively. TiO_2 grown by ALD at 100°C was amorphous (Figure 4.8) [as in ref. 237; 238]. Sintering these films at 500°C for 45 min formed poly-crystalline anatase. Analysis of the XRD patterns revealed that the crystallite size in the 400 nm thick films was ≈105 nm. Two sintered TiO_2 films, 30 nm and 60 nm in thickness, were measured for comparison and resulted in a crystallite size of ≈47 nm and ≈78 nm respectively (patterns similar to Figure 4.8). These grain sizes have been determined by assuming a isotropic crystallite shape. The fact that the crystallites of these films are larger than the film thickness and smaller than the grains in the 400 nm thick films suggests that these crystallites have an anisotropic shape, which is restricted to the thickness of the constituent film.

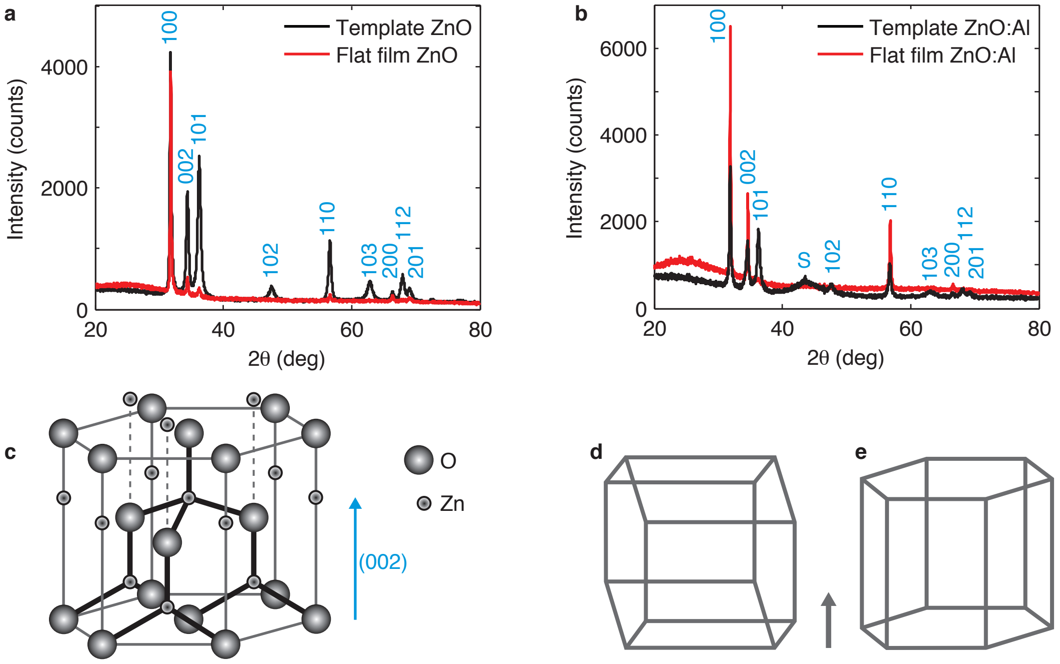

Figure 4.9: Diffractograms of 400 nm thick ZnO (**a**) and 250 nm thick ZnO:Al (**b**) film deposited by ALD at 200°C on a template (black) or flat glass substrate (red). The ZnO:Al template was small so that part of the X-ray beam scattered from the aluminum sample holder, resulting in broad peak (S). Blue numbers represent crystal planes of the wurtzite structure, represented in (**c**), adapted from ref. [260]. (**d**, **e**) The diffractograms of flat films show that each ZnO and ZnO:Al film grows in two distinct phases with different orientations of the wurtzite structure with respect to the surface normal of the substrate (arrow).

X-ray diffractograms of 400 nm thick ZnO and 250 nm thick ZnO:Al films deposited at 200°C on photonic crystal polymer templates and flat glass coverslips show ALD growth of poly-crystalline zincite, which has the hexagonal wurtzite structure [241; 261; 262] (Figure 4.9 a–c). However, reflections from the (101), (102), (103), (201), and (112) crystal planes are absent in the XRD pattern of the flat films. This suggests ALD growth of ZnO and ZnO:Al films in two distinct modes, represented by the (100), (200), and (110) reflections (Figure 4.9 d) and by the (002) reflection (Figure 4.9 e). The diffractograms of the films grown on photonic crystal templates could not show this effect of oriented ALD growth because, in contrast to a flat substrate, the topology of the template allows X-ray diffraction from all crystal planes of the wurtzite structure. Refinement analysis of the patterns by Dr. R. Gunning [259] also revealed that the ZnO and ZnO:Al films were highly strained, which made determination of crystallite sizes difficult (not shown). XRD patterns of films which were sintered at 500°C resembled the patterns of the non-sintered films above. This means that the observed strain was not released at this temperature, so higher temperatures may be needed.

4.4.4 Conductivity of ZnO:Al Films

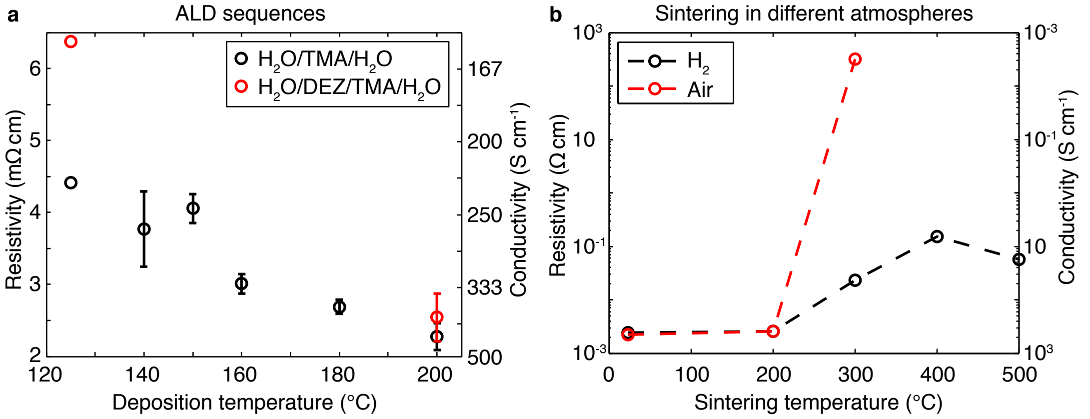

Figure 4.10: Resistivity of ZnO:Al films that were deposited at different reactor temperatures (**a**). As second impurity sequence, a diethylzinc (DEZ) pulse was added to the water/trimethylaluminium (H_2O/TMA) impurity cycle. Error bars represent the standard error of the mean over three different samples. Resistivity of ZnO:Al films that were sintered in air compared to a 2% hydrogen/nitrogen (H_2/N_2) atmosphere (**b**). Dashed lines serve as guides to the eye.

As outlined in Section 4.2.3 on page 70, in the impurity cycle of the ZnO:Al ALD process the precursor sequence water/trimethylaluminium (H_2O/TMA) replaces a water/diethylzinc sequence (H_2O/DEZ). The reported resistivity of ZnO:Al films produced this way reaches a minimum at a TMA/DEZ doping ratio of 1/20 [263]. By adopting this doping ratio and a 20 s purge time for the ZnO:Al process, 56 nm thick ZnO:Al films were produced at various processing temperatures (see ALD routine in Table 4.2 on page 78) and their resistivity measured with the van-der-Pauw method (described in Appendix D on page 123). The resistivity of these films decreased with temperature and followed a trend as in ref. [240] (Figure 4.10 a). Na et al. [263] showed that inserting an additional diethylzinc (DEZ) pulse into the impurity cycle at 125°C, i.e. using the sequence H_2O/DEZ/TMA, led to an improvement in conductivity of the resulting ZnO:Al films. Using this impurity cycle sequence at 125°C resulted in ZnO:Al films with increased resistivity in comparison to the films grown with the conventional impurity sequence, which opposed the result of Na et al. [263] (Figure 4.10 a). The resistivity of ZnO:Al films deposited at 200°C was comparable for both type of impurity sequences, $\rho \lesssim 3\,\mathrm{m}\Omega\,\mathrm{cm}$. Sintering ZnO:Al films in air induced a rapid loss of conductivity above 200°C deposition temperature (Figure 4.10 b). This confirms the studies by Ellmer and Vollweiler [264], who found that ZnO:Al films are susceptible to oxidation, which leads to defects in the film. Hydrogen inclusion can passivate these defects [265; 266]. Performing the sintering in a 2% hydrogen/nitrogen atmosphere revealed a reduced rise in resistivity above 200°C and a trend of recovery at 500°C.

4.5 Deposition on Photonic Crystal templates

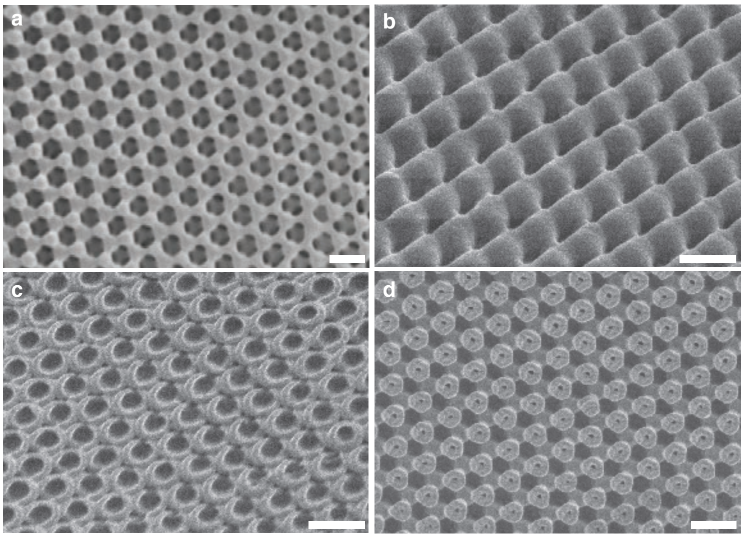

Figure 4.11: SEM images [187] illustrate procedure for producing inverse replicas of photonic crystal templates by ALD (TiO_2 in this case). (**a**) Initial photonic crystal SU-8 template. (**b**) Template completely back-filled with TiO_2 ALD layer. (**c**) Argon-ion (Ar^+) milling the top surface of TiO_2 layer until underlying template exposed. (**d**) Removing SU-8 template by oxygen plasma etching produces the TiO_2 inverse replica. Scale bars are 1 µm.

In order to show that ALD is uniform throughout the bulk of the photonic crystal template, inverse replicas of the template were prepared and imaged with a scanning electron microscope (details in ref. [187]). The initial step for making inverse replicas

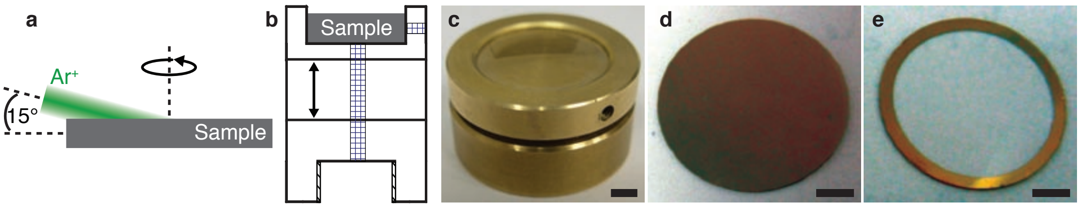

Figure 4.12: Schematic of Ar^+ milling process (**a**). Side view of ion mill sample holder (**b**) that was variable in height (double arrow) in order to set the Gaussian Ar^+ beam off center. Photograph of custom built sample holder (**c**). Gold coated coverslip served as indicator for uniformity of Ar^+ etch (**d**: before and **e**: after milling). Scale bars are 3 mm.

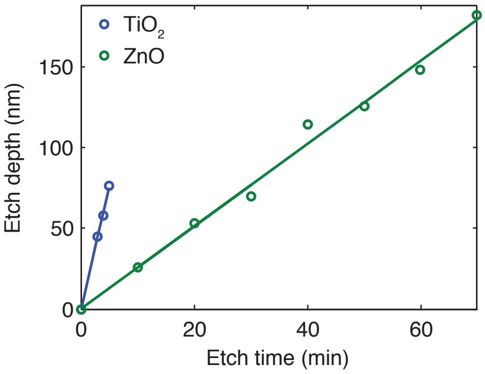

Figure 4.13: The reactive ion etch (RIE) rates 15 nm/min and 2.6 nm/min for TiO_2 and ZnO respectively were determined by linear fits.

was to deposit a thick ALD layer on the template so that its pores were completely filled (Figure 4.11 b). The template beneath the enclosing ALD layer was exposed by etching the top surface of the ALD coated sample (Figure 4.11 c). Initially a Gatan dual-beam argon-ion (Ar^+) mill was used to etch TiO_2 at a rate 4 nm/min with a 15° incidence angle, 6 keV acceleration voltage, and 1.5 mA gun current (Figure 4.12 a). A custom-made sample holder was able to hold 3 mm thick substrates for photovoltaic purposes (Figure 4.12 b) and coverslips for testing etch uniformity (Figure 4.12 c). Adjusting the height of the sample holder set the 2 mm wide Ar^+ beam off center and allowed a very uniform etch across the whole width of the sample, which is confirmed by etching a gold coated coverslip for test purposes (Figure 4.12 d, e). Due to failure of the vacuum pump and impossibility for replacement, following etches were done in a reactive ion plasma of 67% sulfur hexafluoride and 33% Ar. Profiling TiO_2 and ZnO samples that were etched at 100 W and 200 W forward power respectively

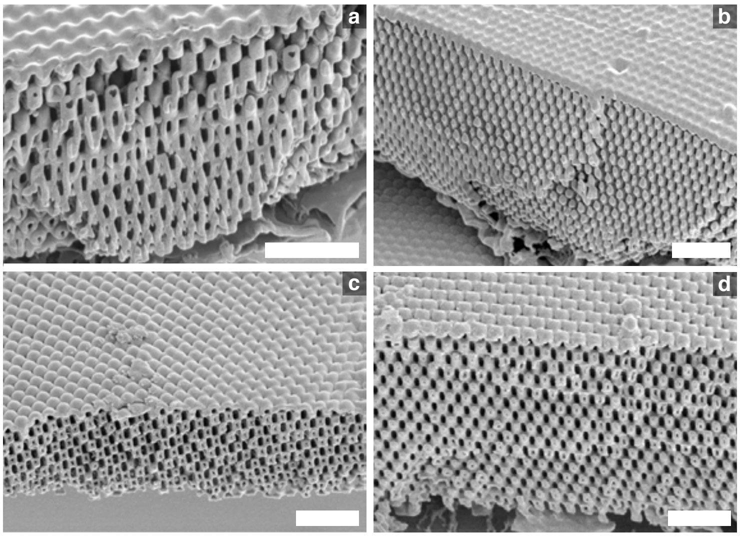

Figure 4.14: Scanning electron micrographs [187] show bulk of photonic crystal inverse replicas produced by ALD of (**a**) 250 nm Zr_3N_4 at 175°C, (**b**) 400 nm TiO_2 at 100°C, (**c**) 250 nm ZnO:Al at 200°C, and (**d**) 250 nm Al_2O_3 at 200°C. Scale bars are 3 µm.

resulted in etch rates of 15 nm/min and 2.5 nm/min (Figure 4.13). The template was finally removed in an oxygen plasma at an etch rate 2 µm/h by using a plasma-cleaner (Diener-electronic Pico) at 200 W (Figure 4.11 d). Alternatively, if subsequent sample treatment included a sintering step at 500°C the polymer template was burned off within 45 min. Photonic crystal inverse replicas of TiO_2, Zr_3N_4, ZnO, ZnO:Al, and Al_2O_3 were produced by following the introduced ALD routines (Table 4.2 on page 78). In SEM images they all appeared uniform in the bulk (Figure 4.14) and confirmed the developed reinforcement method of photonic crystal polymer templates, described in Section 3.5.

4.6 Discussion

Atomic layer deposition is a thin-film growth technique, which allows the deposition of an abundant selection of materials. The produced films are highly conformal and can coat structures with aspect ratios larger than 1000. Commonly used ALD processes were applied to grow TiO_2, ZnO, ZnO:Al, and Zr_3N_4 on photonic crystal polymer templates that were fabricated according to the techniques outlined in Chapter 3. For this purpose an ALD apparatus was constructed. Optimization of its reactor and sample holder design enabled a uniform temperature distribution and homogeneous ALD in the reaction chamber. Ellipsometry measurements confirmed uniformity of the produced films and determined the growth per cycle for each ALD process used. Electron micrographs confirmed that all these ALD processes produced uniform films within photonic crystal polymer templates. Calcination and dry etching techniques, such as argon-ion milling, reactive ion etching, and oxygen plasma etching, were utilized in order to produce inverse replicas of photonic crystals templates with the mentioned ALD materials. XRD experiments showed that ZnO and ZnO:Al films deposited at 200°C consisted of crystalline zincite with a preferential orientation but possessed strain, which could not be released by sintering. The ZnO:Al films grown between 160–200°C exhibited a resistivity below $4\,\mathrm{m\Omega\,cm}$ after ALD. However, these films lost their conductivity in a sintering process due to oxidation. This increase in resistivity with temperature could not be completely diminished in a 2% hydrogen/nitrogen atmosphere. The ZnO:Al films were therefore impractical for use as transparent conducting oxides in solar cell architectures, which require sintering processes during device manufacture. TiO_2 films grew amorphous at 100°C but turned to poly-crystalline anatase with a crystallite size of 105 nm after sintering at 500°C. ZnO and TiO_2 films were used as electron-transporting layers in different heterojunctions that were implemented in solar cell devices according to Scheme 1 in Section 2.3. The fabrication and characterization of these devices will be described in the following chapter (Chapter 5).

5 Solar Cell Device Structures

5.1 Introduction

Following Scheme 1 on page 38, metal oxide photonic crystal structures were produced on fluorine doped tin oxide (FTO) substrates by applying the techniques of holographic lithography (Chapter 3) and atomic layer deposition (Chapter 4) and were included in the proposed DSSC and organic-norganic hybrid solar cell devices. Because the fabrication of these solar cell devices involved calcination and sintering processes at 500°C, it was unfeasible to grow ZnO:Al films by ALD and to use them as transparent conducting oxide electrodes in the proposed photonic crystal solar cell devices. The produced photonic crystal structures therefore consisted of TiO_2 and ZnO and were included as electron-transporters in TiO_2 DSSC devices and ZnO-polymer solar cell devices respectively. Before reporting on fabrication and performance of these devices (in Section 5.3 and Section 5.4), this chapter starts with an introduction to the characterization techniques (Section 5.2).

The TiO_2 DSSC device comprised the ruthenium-based dye N-719 (dye B2 from Dyesol; abbreviation in Appendix A) and an iodine-iodide electrolyte (composition in Appendix E.2) (Sections 5.3.1–5.3.2). Its performance was compared to a nanocrystalline TiO_2 DSSC device (as in ref. [99]) that contained the same dye and electrolyte (Section 5.3.3). The attempt to combine the TiO_2 photonic crystal structure with nanocrystalline TiO_2 is described in Section 5.3.4.

The ZnO photonic crystal structure comprised a solar cell device with layers of the organic electron-acceptor molecule $PC_{60}BA$ (Sigma-Aldrich), the absorbing polymer P3HT (Rieke Metals, 4002-E), and the hole transporting polymer PEDOT:PSS (Clevios) (Sections 5.4.1 and 5.4.2; abbreviations in Appendix A). The thickness of these organic layers was optimized (Section 5.4.3) and the performance of the resulting photonic crystal devices was compared to a flat bilayer device with the same material layers (Section 5.4.4).

5.2 Solar Cell Device Characterization

The power-conversion efficiency, fill factor, charge carrier transport properties, and external and internal quantum efficiency were characterized by using established techniques in the group of Dr. H. Snaith [267]. They are introduced in the following sections.

Current-Voltage Characteristics

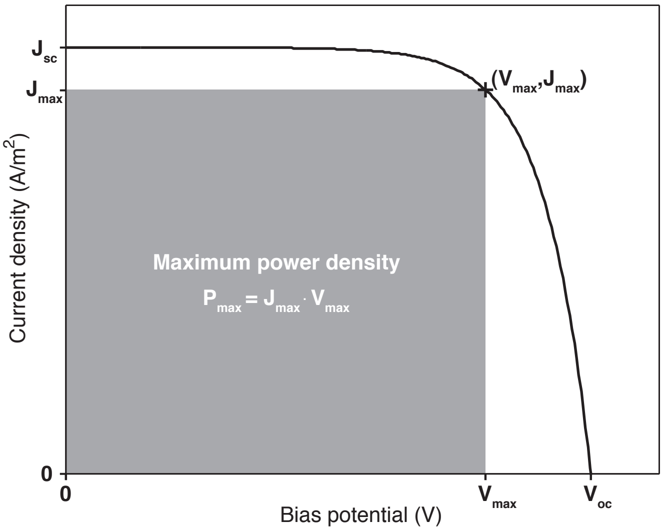

Figure 5.1: Photocurrent density-voltage (J-V) curve of a photovoltaic device connected to an external load, highlighting its maximum power density ($\mathrm{P}_{\mathrm{max}}$), short-circuit current density (J_{sc}), and open-circuit voltage (V_{oc}).

The relationship between current density and bias potential (J-V curve) of a photovoltaic device is a convenient tool to determine its power-conversion efficiency η, open-circuit voltage V_{oc}, short-circuit current density J_{sc}, and fill factor FF (Figure 5.1). In order to measure these four quantities, solar cell devices were illuminated with white light from a Solar Simulator (ABET Technologies Sun 2000) under standard test conditions, i.e. at 25°C and using a reference spectrum with air mass coefficient 1.5 (AM1.5) [11] and solar power density $P_\mathrm{s} = 100\,\mathrm{mW/cm^2}$. Simultaneously a sourcemeter (Keithley 2400) applied a bias potential difference, V, to the devices and measured their photo-current densities, J, which were recorded with respect to the bias by a National Instruments card (NI-SCX-1000) and LabVIEW program (written by Mr. P. Docampo [268]). From these J-V curves J_sc, J_max, V_oc, and V_max were determined with a MATLAB script and FF and η were calculated according to Equations (2.8) and (2.11) on page 10.

5.2.1 Charge Carrier Transport Measurement

Measurements of photo-current and photo-voltage transients provide insight into the kinetics of electron transport and recombination in solar cell devices [269; 270]. For this purpose perturbation transient photo-voltage and photo-current decay measurements were performed by using the instrument established by Mr. P. Docampo [271] (and described in ref. [272]). In this apparatus a steady-state bias light from an array of white light diodes (Lumiled LXHLNWE8 whitestar) generated charge-carriers (photo-carriers) in the device. In order to probe the kinetics of these photo-carriers a probing light pulse was superimposed on the bias light [273]. This probe pulse originated from red light diodes (LXHLND98 redstar). They were pulsed by a solid-state switch that opened upon a square, 200 µs wide electrical pulse with 100 ns rise and fall time from a function generator (Agilent 33250A). The pulse intensity was adjusted so that the resulting intensity perturbation induced monoexponential photo-voltage and photo-current transients. These transients were measured by a 1 GHz oscilloscope (Agilent MSO6104A) and recorded with a LabVIEW program (developed by Mr. P. Docampo [271]).

Photo-voltage transients, in the form of

$$V(t) = V_\mathrm{A}\mathrm{e}^{-t/\tau_\mathrm{r}} + V_0\ , \tag{5.1}$$

were measured at open-circuit conditions across the high-impedance ($1\,\mathrm{M\Omega}$) port of the oscilloscope. The constant voltage offset V_0 caused by the bias light was removed from the voltage transient with a sourcemeter (Keithley 2400) that was connected in parallel to the oscilloscope port [272]. As a result, the decay time τ_r, obtained from Equation (5.1), determines the recombination rate $k_\mathrm{r} = 1/\tau_\mathrm{r}$ of charge carriers generated solely by the probe pulse.

Photo-current transients, in the form of

$$J(t) = J_\mathrm{A}\mathrm{e}^{-t/\tau_\mathrm{s}} + J_\mathrm{sc} \ , \tag{5.2}$$

were measured at short-circuit conditions through the oscilloscope's low-impedance ($50\,\Omega$) port. During this transient however, charge carriers recombine on their journey to the electrode. Hence, the decay time τ_s from Equation (5.2) is a combination of charge-recombination time, τ_r, and charge-collection time, τ_c, so that [272]

$$\tau_\mathrm{c} = \frac{1}{1/\tau_\mathrm{s} - 1/\tau_\mathrm{r}} \ . \tag{5.3}$$

Measurement of τ_c, sample thickness d_sample, and porosity P of the solar cell device allows determination of the diffusion constant

$$D_\mathrm{e} = \frac{d^2_\mathrm{sample}}{2.35\tau_\mathrm{c}} \tag{5.4}$$

and the photo-carrier density

$$N = \frac{J_\mathrm{sc}\tau_\mathrm{c}}{e d_\mathrm{sample}(1-P)} \tag{5.5}$$

of the injected electrons [111; 274], where e is the electron charge. The electron diffusion length

$$L_\mathrm{e} = \sqrt{D_\mathrm{e}\tau_\mathrm{r}} \tag{5.6}$$

conveniently illustrates the distance that an electron diffuses before it recombines (see also Equation 5.6 on the preceding page).

5.2.2 Spectral Response Measurement

The spectral response of a solar cell device is revealed by the external quantum efficiency (EQE), which describes the number of electrons delivered to a load per incident photon (as introduced in Section 2.1.2 on page 9). Hence the EQE can be written as the ratio of the number of electrons per second, J_λ/e, and the number of incident photons per second, $P_\lambda/h\nu$,

$$\mathrm{EQE}(\lambda) = \frac{J_\lambda h\nu}{eP_\lambda} = \frac{hc}{e}\frac{J_\lambda}{\lambda P_\lambda} \approx (1241/\mathrm{V\,nm})\,\frac{(J_\lambda/\mathrm{A\,cm^{-2}})}{(\lambda/\mathrm{nm})(P_\lambda/\mathrm{W\,cm^{-2}})}\ , \tag{5.7}$$

which is conveniently expressed in terms of short-circuit current density J_λ and spectral power density P_λ at the incident wavelength of light λ, and the constant $hc/e = 1241\,\mathrm{V\,nm}$ [275].

In order to measure the EQE, solar cell devices were illuminated with a monochromator (Princeton Instruments, Acton SP2150i), which selected a 0.5 nm narrow band of wavelengths from a 250 W tungsten-halogen light source (Acton TS428) and scanned it from 300 nm to 800 nm in 5 nm increments [276]. The monochromatic light beam was periodically chopped with a shutter (Thorlabs, SH05) in order to perturb a steady-state white bias light, which was provided at 0.5 sun by two LEDs (Luxeon star, LXHL-NWE8). Three 50 mm convex lenses superimposed the light of all three light sources and converged it onto the device. Both electrodes of the device were connected to a sourcemeter (Keithley 2400), which measured the generated photo-current density, J_λ. A LabVIEW program, written by Dr. M. Brown and Dr. J. Ball [276], recorded J_λ with respect to wavelength from a National Instruments card (NI-SCX-1000). A photodiode (Centronic, OSD5.8-7Q) was used as reference for the measured solar cell devices in order to calibrate P_λ. The resulting EQE is less than 100% due to reflection losses of the incident light, imperfect absorption of the photoactive material within the cell, recombination of charge carriers, and electrical resistance losses in the device and external circuit.

5.2.3 UV-Vis Absorption Spectrum

The absorption spectrum, $A = 1 - T - R$, of a device was obtained by measuring the reflection, R, and transmission, T, with the ultraviolet-visible (UV-Vis) spectrometer (Varian Cary 300 Bio). The instrument was equipped with an integrating sphere that collected scattered light in the range (250–800) nm.

5.3 TiO_2 Dye-Sensitized Solar Cell Devices

5.3.1 TiO_2 Structures

Two different TiO_2 photonic crystal structures were developed and compared to a nanocrystalline TiO_2 reference structure. All three structures were produced on conductive 14 mm square FTO-substrates (Pilkington, TEC 15). Fabrication of the photonic crystal structures included the TiO_2 ALD process introduced in Section 4.2.3. During this process a 3 mm wide area on the edge of the FTO substrate was covered by Kapton tape in order to facilitate electrical contact between the conductive FTO and the conductive silver paste (Agar-scientific) that was applied at the end of device production.

Photonic Crystal Shell

One photonic crystal structure consisted of a 90 nm thick TiO_2 shell, which was fabricated by growing a 30 nm thick TiO_2 layer on the photonic crystal SU-8 template and burning the template off at 500°C for 1 hour. Due to the removal of the template, cracks developed in the TiO_2 film and exposed the FTO substrate underneath. A 30 nm TiO_2 ALD blocking layer on the photonic crystal shell structure covered these cracks in order to prevent leakage currents in the complete device.

Photonic Crystal Inverse Replica

The other photonic crystal TiO_2 structure was an inverse replica of the original template, which was fabricated as described in Section 4.5 on page 82. Due to removal of the polymer template, this replica structure also developed cracks, which were covered by a 30 nm thick TiO_2 blocking layer.

Nanocrystalline Reference Structure

Nanocrystalline TiO_2 reference devices were made by following established procedures [99; 277]. For this purpose, FTO substrates were cleaned (procedure in Appendix E.1) and provided with a ≈100 nm thick TiO_2 blocking layer by 40 sprays of a solution of 10 wt% titanium diisopropoxide bis(acetylacetonate) (Sigma-Aldrich) in ethanol at 450°C. After cooling to room temperature, 0.7 ml of 625 mg/ml colloidal TiO_2 paste (Dyesol DSL 18 NR-T) in ethanol was spread with a Pasteur pipette onto the TiO_2 blocking layer. A temperature ramp to 500°C burned off the ethyl cellulose in the paste and created the nano-porous TiO_2 structure. By using a craft knife the resulting 3–5 µm thick nanocrystalline film was removed from most of the substrate, leaving a 5 mm wide circular area in the center of the substrate so that the sample size was comparable to the photonic crystal structures. Subsequently the structures were kept in a bath of 20 mM $TiCl_4$ in deionized water for 1 hour at 70°C, which formed a continuous TiO_2 film on the nano-particulate structure.

5.3.2 TiO_2 Device Configuration

Dye Loading

Once the above TiO_2 structures were established, they were sintered at 500°C for 45 min on a hot-plate. As soon as the hot-plate cooled to 70°C the structures were immersed in a dye solution for 20 hours and subsequently rinsed in acetonitrile. The dye solution consisted of 10 mg N-719 dye dissolved in 40 ml of a 1:1 solution of acetonitrile and tert-butanol.

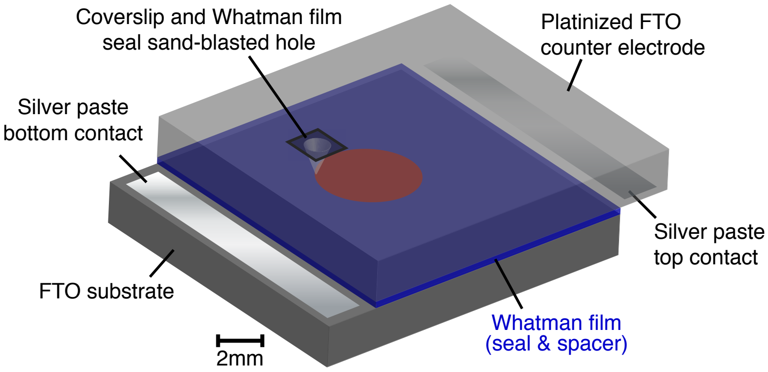

Figure 5.2: Schematic of dye-sensitized solar cell (DSSC) device. The red circular region illustrates the volume between the two electrodes filled with electrolyte, i.e. the heterojunction of the device.

Counter Electrode

The TiO_2 structures were covered with a platinized 15×13 mm^2 FTO glass (Pilkington, TEC 15) counter electrode (Figure 5.2). This counter electrode was provided with a ≈1 mm hole by using a fine nozzle of a sand-blaster and cleaned following the protocol in Appendix E.1. Subsequently this electrode was platinized by spreading 40 µl of 50 mM chloro-platanic acid hydrate (Aldrich 254029) in propan-2-ol evenly with the edge of a Pasteur pipette (Camlab) and heated for 15 min at 450°C.

Sealing the Solar Cell Device

The counter electrode was attached to the substrate with a strip of Whatman sealing film in which a 5.5 mm circular hole had been punched out with a custom-made steel stamp. This hole was lined up with the 5 mm wide TiO_2 structure between both electrodes so that the sealing film completely covered the FTO substrate around the sample and the sand-blasted hole in the counter electrode was at the periphery of the TiO_2 structure (see Figure 5.2). By placing both electrodes on a hot plate at 90°C, the film melted, sealed the cell under compression, and acted simultaneously as an insulating spacer which kept both electrodes ≈100 µm apart. The space that resulted from the circular hole in the film defined a volume of ≈0.8 µl.

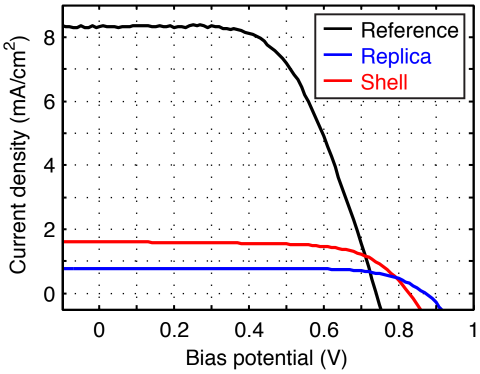

Figure 5.3: J-V curve of dye N-719 sensitized electrolyte devices, which were based on nanocrystalline (black), photonic crystal 90 nm shell (red), and inverse replica (blue) TiO_2 structures (see Section 5.3.1).

Adding Electrolyte and Electrode Contacts

By adding 20 µl of the iodine-iodide electrolyte solution into this opening and applying low-pressure in a vacuum chamber, the electrolyte displaced the air in the device volume. A piece of Whatman sealing film was sandwiched between the opening and a coverslip (Agar-Scientific, 18 mm, #1.5). The use of a 300°C hot soldering iron sealed the sand-blasted hole. After applying conductive silver paste (Agar-scientific) onto clear regions of bottom and top electrodes the device was characterized.

5.3.3 Device Performance

This section describes the characterization of the fabricated dye N-719 sensitized TiO_2 photonic crystal 90 nm shell and inverse replica devices with the techniques outlined in Section 5.2 on page 87. The above described dye N-719 sensitized 20 nm nanocrystalline TiO_2 reference device served as a reference for the photonic crystal devices.

Roughness Factor and Current-Voltage Characteristics

Analysis of the J-V curves (Figure 5.3) showed that the photonic crystal shell device provided a two times larger power conversion efficiency η and short-circuit current density J_{sc} than the replica device (results in Table 5.1). With the intention to explain this gain in performance, the roughness factors of both photonic crystal shell and

	Reference	Shell	Replica	$\frac{\text{Shell}}{\text{Replica}}$	$\frac{\text{Reference}}{\text{Shell}}$	$\frac{\text{Reference}}{\text{Replica}}$
P	0.54	0.70	0.45			
d_{sample} (μm)	6	15	15			
RF	600	155	75	2.1	3.9	8.0
η (%)	3.6	0.90	0.49	1.8	4.0	7.3
J_{sc} (mA/cm^2)	8.3	1.6	0.77	2.1	5.2	10.7
V_{oc} (mV)	741	830	872			
FF (%)	58	67	73			

Table 5.1: Porosity P, sample thickness d_{sample}, and roughness factor (RF) of fabricated TiO_2 structures. Performance results of DSSC devices from J-V curves in Figure 5.3.

replica structures were determined by

$$\text{RF} = \frac{A_{\text{unit}}}{d_{\text{unit}}} d_{\text{sample}} \tag{5.8}$$

where A_{unit}, d_{unit}, and d_{sample} are the interfacial surface area per unit cell, thickness per unit cell layer, and sample thickness for each structure respectively. A_{unit} was calculated by surface triangulation with a MATLAB script [278], resulting in ≈7.2 and ≈3.5 for photonic crystal shell and replica structures respectively. SEM micrographs (such as in Figure 4.14 on page 84) revealed a unit cell layer thickness of $d_{\text{unit}} \approx 700\,\text{nm}$ for both shell and replica structures. The sample thicknesses (d_{sample}) of shell and replica devices were measured with a stylus surface profilometer (Dektak 6M) and resulted both in 15 μm, leading to the roughness factors $\text{RF}_{\text{shell}} = 154.5$ and $\text{RF}_{\text{replica}} = 75$ respectively. The resulting ratio, $\text{RF}_{\text{shell}}/\text{RF}_{\text{replica}} \approx 2.1$, shows that the 90 nm shell device is expected to contain at least twice the amount of charge generating dye molecules in comparison to the replica device. This result accords with the (shell/replica) ratios ≈1.8 and ≈2.1 of the measured η and J_{sc} respectively (see Table 5.1).

Profilometry of the nanocrystalline reference device resulted in a sample thickness of 6 μm, leading to a roughness factor of $\text{RF}_{\text{reference}} \approx 600$ [279], which is ≈3.9× and ≈8.0× larger than RF_{shell} and $\text{RF}_{\text{replica}}$ respectively. These RF ratios are lower than the reference/shell and reference/replica ratios for J_{sc} (see Table 5.1). This can be explained by an overestimation of the photonic crystal shell and replica roughness

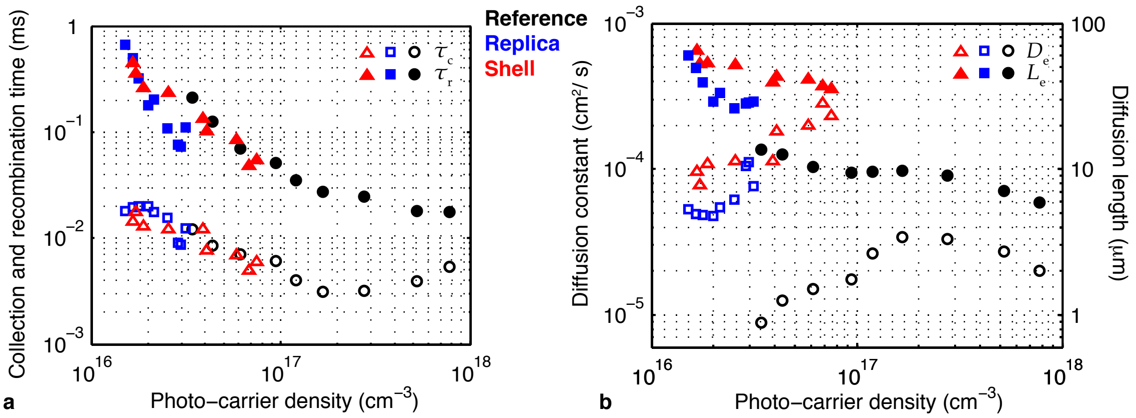

Figure 5.4: Photo-current and photo-voltage transient measurements on nanocrystalline reference (circle), photonic crystal shell (triangle), and photonic crystal inverse replica (square) devices result in collection time τ_{c}, recombination time τ_{r}, diffusion constant D_{e}, and diffusion length L_{e} of charge-carriers (Section 5.3.1). Data points at the second highest photo-carrier density of each sample was measured at 100 mW/cm^2 (1 sun) irradiance.

factors due to the macroscopic cracks emerging in the templates at elevated ALD processing temperatures (as described in Section 3.5.4 on page 60). FF and V_{oc} of both photonic crystal devices is significantly larger than of the nanocrystalline device, which suggests that more defect states occur in the solution processed nanocrystalline $\mathrm{TiO_2}$ structure, compared to the ALD processed photonic crystal devices.

Photo-current and photo-voltage transients

The kinetics of charge carriers in solar cell devices were characterized by measuring and analyzing photo-current and photo-voltage transients (as described in Section 5.2.1 on page 88) at bias light intensities in the range (26–124) mW/cm^2. The resulting charge collection times, τ_{c}, and recombination times, τ_{r}, (Figure 5.4 a) and the film porosities of nanocrystalline and photonic crystal devices were used to calculate the photo-carrier density with respect to the incident bias light intensity (according to Equation 5.5). The porosity of the reference structure, $P_{\mathrm{reference}} \approx 0.54$, was obtained by gas adsorption studies on nanocrystalline films by Mr. P. Docampo [280]. SEM of photonic crystal structures allowed estimation of the porosities $P_{\mathrm{replica}} \approx 0.45$ and $P_{\mathrm{shell}} \approx 0.7$ for $\mathrm{TiO_2}$ replica and 90 nm shell structures respectively. The resulting

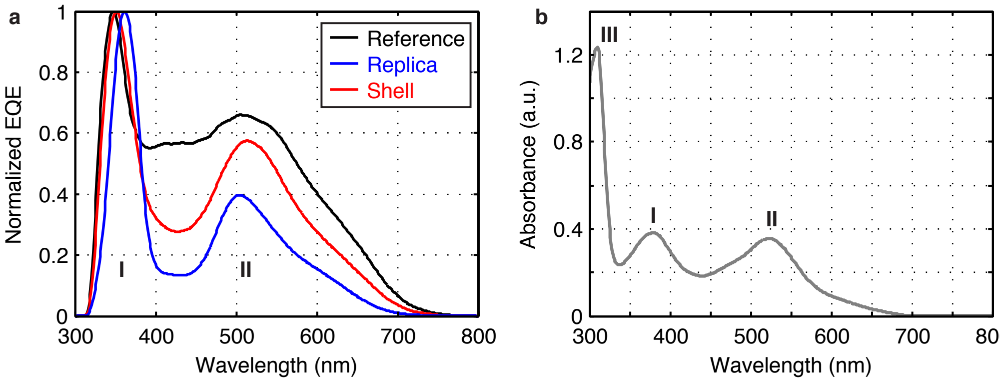

Figure 5.5: Normalized external quantum efficiency (EQE) of solar cell devices, based on nanocrystalline reference (black), photonic crystal 90 nm shell (red), and inverse replica (blue) TiO_2 structures, that were sensitized with dye N-719 (**a**). EQE peaks **I** and **II** correspond with absorbance peaks (**I** and **II**) of the dye N-719 which result from metal-to-ligand charge transfer transitions (**b**, adapted from ref. [282]). Ligand-centered charge transfer transitions of the dye lead to absorbance peak **III**, not apparent in the EQE.

photo-carrier density of the nanocrystalline device is larger than that of the photonic crystal devices, as expected, due to its larger internal surface area (Figure 5.4).

The diffusion constants for charge carriers (Equation 5.4) in the photonic crystal devices were an order of magnitude larger than that of the nanocrystalline device (Figure 5.4 b). In comparison to the reference device, the diffusion lengths (Equation 5.6) were two and three times larger for photonic crystal replica and shell devices respectively (Figure 5.4 b). This result suggests that compared to the discontinuous assembly of TiO_2 nano-particles in the nanocrystalline device, which is prone to charge recombination, the continuous network of the TiO_2 photonic crystal structure is beneficial for charge transport to the electrode. Faster charge collection in the continuous photonic crystal network is supported by the fact that the measured crystallite size of 105 nm in sintered TiO_2 ALD films (Section 4.4.3) is significantly larger compared to the 20 nm large crystallites in the nanocrystalline TiO_2 film [126; 281]. This leads to less scattering of charge carriers in the ALD film and thus higher charge mobilities.

Spectral response

The measured EQEs of the three TiO_2 devices exhibit two distinct peaks—one in the near ultraviolet (**II**), which sets the baseline at ≈360 nm, and the other in the visible part of the spectrum (**III**) at ≈560 nm (Figure 5.5 a). Both EQE peaks correspond with the absorbance peaks of the N-719 dye that result from the lower-energy metal-to-ligand charge transfer transitions [282; 283] (**I** and **II** in Figure 5.5 b). The absorbance at ≈310 nm (**III**), which results from higher-energy ligand-centered charge transfer transitions of the dye, did not contribute to the photo-current of the devices.

5.3.4 Combining Photonic Crystal and Nanocrystalline Structures

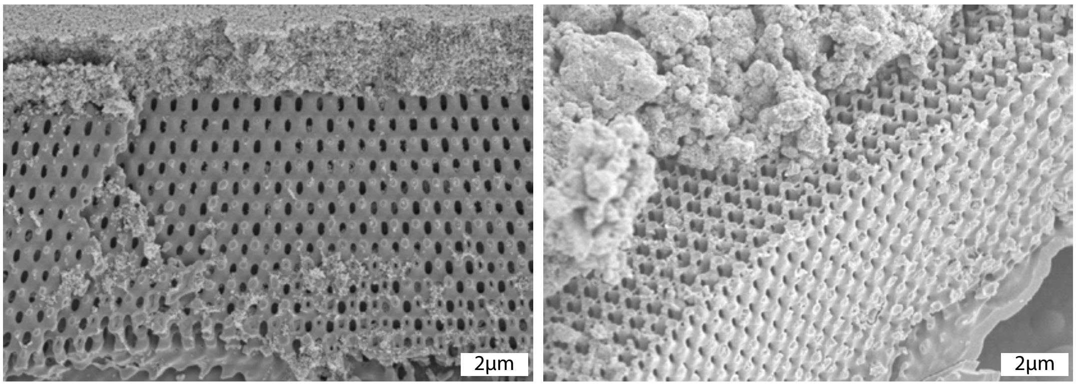

Figure 5.6: Instead of filling the pores of TiO_2 photonic crystal inverse replica structures, the TiO_2 nano-particulate paste formed a layer on the top surface of the replica structure regardless of concentration and composition of the paste used—whether it contained ethyl-cellulose, α-terpineol and ethanol (left), or only TiO_2 particles and ethanol (right). Structures shown in both SEM images [187] were made from 20 v% TiO_2 paste.

Combining the advantages of fast transport properties of the photonic crystal TiO_2 network and the high surface area of the nanocrystalline film was attempted by infiltrating TiO_2 photonic crystal structures with TiO_2 nano-particles. For this purpose commercial TiO_2 paste (Dyesol DSL 18NR-T) was diluted in ethanol with concentrations in the range (0.1–25) v%. 20 µl of these pastes was added to TiO_2 photonic crystal structures by spin-coating for 30 sec at 1000 rpm. SEMs confirmed that, regardless of its concentration, the paste remained at the top surface of the structure instead of coating the bulk (Figure 5.6, left).

The used Dyesol paste contained high viscosity ethyl-cellulose (10-46 mPa s). With the intention to make a TiO_2 paste with lower viscosity, a paste was prepared from 10.3 v% low-viscosity ethyl cellulose (Sigma-Aldrich, 46070, 5-15 mPa s), 5.6 v% TiO_2 powder (Sigma-Aldrich, 637254, particle size <25 nm), and 84.1 v% α-terpineol by following the procedure of Ito et al. [284]. This custom-made paste was diluted in ethanol at the same concentrations as above and TiO_2 photonic crystal structures were spin-coated under the same conditions. However, electron micrographs showed that this paste remained at top of the structure similarly to the commercial paste (comparable to Figure 5.6, left). Applying low pressure or heating the paste to 70°C during its application gave the same result. With the aim to increase wettability, the photonic crystal structure was oxygen plasma etched before spin-coating the solution, but the colloids still accumulated at the top surface.

Finally the ethyl cellulose was left out by just diluting the TiO_2 powder in ethanol at concentrations of 1 v%, 5 v%, and 20 v%. These solutions were applied to TiO_2 structures by spin-coating at 1000 rpm for 30 sec. Three separate structures were left in 5 v% and 20 v% solutions for 30 min and in the 1 v% solution for 14 hours for comparison. However, the TiO_2 colloids formed dense clusters on the top surface of the micro-porous structure from all solutions irrespective of the method used (Figure 5.6, right).

5.4 ZnO-Polymer Solar Cell Devices

5.4.1 ZnO Structures

Photonic Crystal ZnO Structure

ZnO photonic crystal structures were produced on conductive 14 mm square FTO-substrates analogous to the procedure for TiO_2 structures above (Section 5.3.1). To this end a ZnO film was deposited on the photonic crystal polymer template by applying the ZnO ALD process (described in Section 4.2.3 on page 69). The FTO-substrate electrode was protected during ALD by covering a 3 mm wide area on the edge of the substrate with Kapton tape. This maintained electrical contact between the conductive FTO and the metal electrode contact that was added at the end of device fabrication (see Section 5.4.2 on the following page). After ALD, the template was burnt off at 540°C for 1 hour, which produced a photonic crystal ZnO shell. During this calcination process, photonic crystal shells collapsed if they consisted of ZnO films that were thinner than 120 nm. After removal of the template a 30 nm ZnO blocking layer was added in order to cover cracks that develop during the heating process.

Flat ZnO Film

Flat ZnO reference films were fabricated for comparison with the ZnO photonic crystal structure by using the same ALD process. For this purpose 14 mm square FTO-substrates were prepared by following the procedure in Appendix E.1. These substrates were protected with Kapton tape prior ALD as explained above.

5.4.2 ZnO Device Configuration

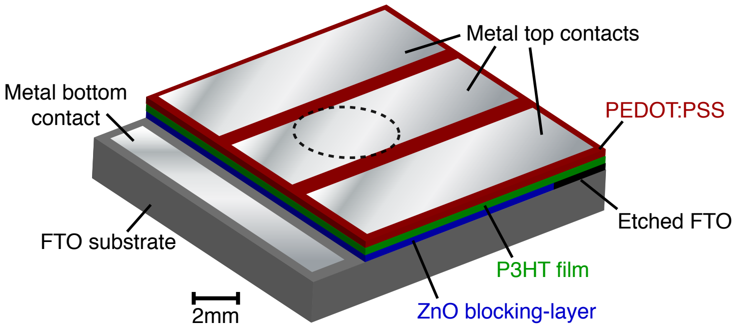

Figure 5.7: Schematic of organic solar cell (DSSC) device. The dashed circle depicts the region where the photonic crystal micro-structure resides.

After supplying the ZnO structures with ZnO blocking layers they were sintered and provided with a layer of P3HT and PEDOT:PSS, along with gold and silver electrode contacts (according to the schematic in Figure 5.7). As these metal contacts were at risk of short-circuiting with the FTO substrate upon contact with a clamp probe, the 350 nm thick FTO electrode was etched before sintering up to a distance of 3 mm from one edge of the substrate which allowed sufficient space for a clamp (black region in Figure 5.7). This region was etched with a mixture of zinc powder and 2 M hydrochloric acid for 30 sec, subsequently rubbed with a cotton bud for another 30 sec, rinsed with deionized water, and dried with a tissue. Thereafter the samples were sintered at 500°C for 45 min. As soon as the samples reached room temperature, they were kept in a 50 μg/ml solution of $PC_{60}BA$ in chlorobenzene for 45 min and rinsed in acetonitrile. Once the samples dried they were spin-coated with P3HT in chlorobenzene and water-based dispersion of PEDOT:PSS. See Section 5.4.3 below for details of the process and how thickness and coatability of both films were optimized. The produced P3HT and PEDOT:PSS films were dried at 150°C for 15 min and enclosed the bottom FTO electrode completely. These polymer films were removed with a craft knife along the edge opposite to the region where the FTO was etched in the first place. Polymer residues were wiped off with a chlorobenzene drenched cotton bud. This enabled electrical connection between the uncovered FTO substrate and the subsequently added metal contact. Metal electrode contacts with the FTO substrate and the PEDOT:PSS film were established by evaporating a 10 nm thick gold electrode pattern onto the device. Subsequently evaporating a 150 nm thick silver film in form of the same pattern reinforced the fragile gold film (as depicted in Figure 5.7).

5.4.3 Film Thickness and Coatability of P3HT and PEDOT:PSS

The P3HT film thickness was optimized with the intention to produce two different devices. One device contained only the P3HT film that filled the pores of the microstructure completely. In the other device the P3HT film thickness was adjusted so that the pores of the photonic crystal provided enough space for an additional layer of PEDOT:PSS.

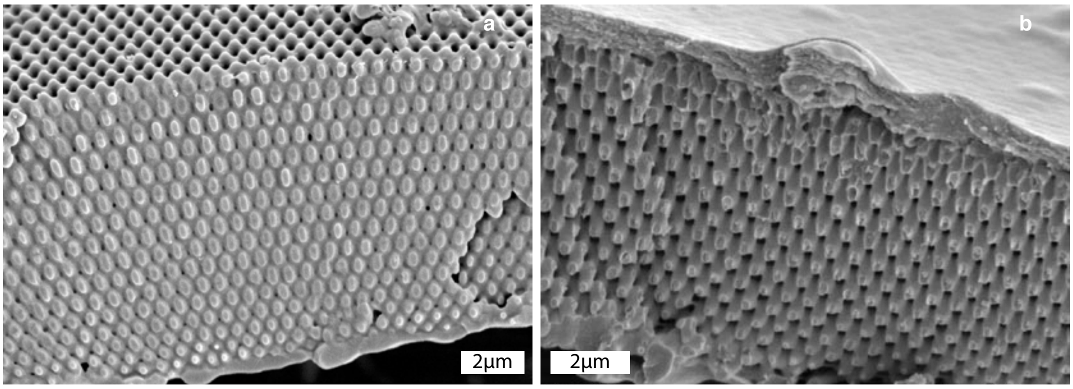

Figure 5.8: SEM images [187] depict photonic crystal templates with 30 nm thick ZnO layers, which were spin-coated at 150 rpm for 5 sec and 2000 rpm for 30 sec with 20 mg/ml (**a**) and 15 mg/ml (**b**) P3HT in chlorobenzene. At the same speeds the P3HT coated photonic crystal structure (**b**) was spin-coated with the commercial PEDOT:PSS dispersion Clevios PH-500. The dispersions Clevios P and Clevios P-VP-AI-4083 were supplemented with 1% Hellmanex, but resulted in a similar film as shown in (**b**).

P3HT Film

The optimal P3HT film thickness was identified for each type of device by SEM imaging photonic crystal structures with a 30 nm thick ZnO layer and by spin-coating them with P3HT dissolved in chlorobenzene at concentrations in the range (5–80) mg/ml. The best P3HT film uniformity was achieved by adding 30 µl of the solution to the sample while it rotated at 150 rpm and subsequently spinning at 2000 rpm for 30 seconds. Scanning electron micrographs confirmed that P3HT started to fill the pores of the ZnO microstructure at concentrations $\geq$20 mg/ml (Figure 5.8 a). 15 mg/ml resulted in a microstructure with open pores and a conformal P3HT film throughout the bulk (Figure 5.8 b). This concentration was therefore used for producing the type of device with P3HT and PEDOT:PSS.

PEDOT:PSS Film

Establishing a uniform film of the water-based PEDOT:PSS dispersion on the hydrophobic P3HT film was difficult due to the high surface tension between them. For test purposes P3HT films were prepared on flat substrates and spin-coated with the water-based PEDOT:PSS dispersion (Clevios P) after filtration with a glass-fiber syringe filter (Acrodisc 1 µm, Sigma-Aldrich). The P3HT film repelled the PEDOT:PSS dispersion so that it formed a droplet with large contact angle. However, exposing the P3HT film to a 6 sec oxygen plasma (200 W) increased its wettability, but colorful fringes in reflection revealed a non-uniform distribution of the subsequently spin-coated PEDOT:PSS films. Supplementing the dispersion with 1% of the detergent Hellmanex in deionized water further reduced the surface tension between the water-based solution and the hydrophobic P3HT film and enhanced uniformity of the resulting PEDOT:PSS film considerably. Thus, Clevios P was used at concentrations in the range (25–100) v% with 1% Hellmanex for spin-coating photonic crystal structures that contained a 30 nm thick ZnO film and a layer of P3HT (as described on the previous page). Similarly to the spin-coating conditions above, this process consisted of a 150 rpm spin at which the PEDOT:PSS solution was applied and was followed by a fast spin at 2000 rpm for 30 sec. However, SEMs showed that the PEDOT:PSS solution formed a layer on the top surface of the P3HT coated microstructures instead of penetrating its pores (Figure 5.8 b).

The used PEDOT:PSS dispersion Clevios P has a viscosity of $\lesssim$100 mPa s, which is the highest in the Clevios product range [41]. The lower viscosity PEDOT:PSS dispersions Clevios P-VP-AI-4083 ($\lesssim$12 mPa s) and Clevios PH-500 ($\lesssim$25 mPa s) (both generously supplied by Dr. A. Watt [285]) were tested whether they infill the P3HT coated ZnO photonic crystal structure. This structure was spin-coated with each dispersion under the same conditions as above and at concentrations in the range (25–100) v%—except that the PH-500 solution precipitated due to addition of Hellmanex so it was used without detergent. Unfortunately both low-viscosity dispersions, Clevios P-VP-AI-4083 and PH-500, had the same effect as Clevios P. They formed a layer of PEDOT:PSS on the top surface of the P3HT coated photonic crystal (Figure 5.8 b).

5.4.4 Current-Voltage Chracteristics

Despite the poor contact between the P3HT and PEDOT:PSS layers, ZnO/P3HT photonic crystal devices were prepared with the above PEDOT:PSS dispersions (following

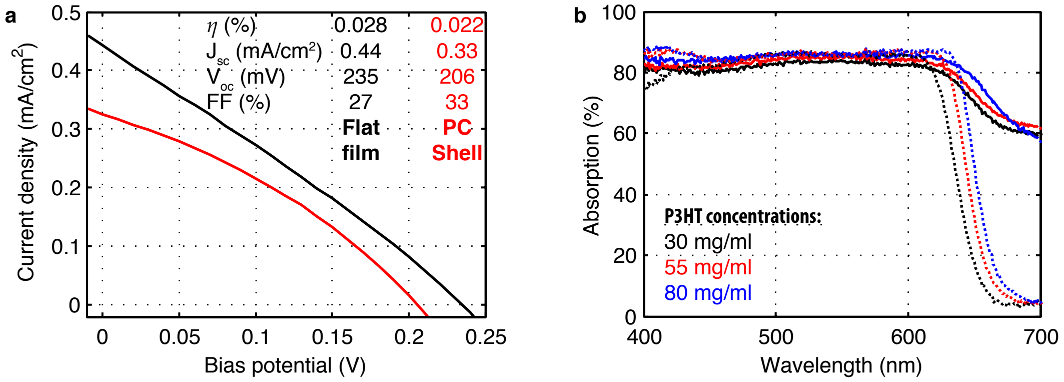

Figure 5.9: (**a**) Current-voltage characteristics of best ZnO/P3HT/PEDOT:PSS devices, based on a 180 nm thick photonic crystal (PC) shell structure (red), compared with a 30 nm thick flat ZnO film (black). (**b**) UV-Vis absorption of P3HT coatings that were spun from solutions with different P3HT concentrations on flat ZnO substrates (dotted) and 150 nm thick photonic crystal ZnO shell structures (solid).

fabrication methods in Sections 5.4.2 and 5.4.3). Their current-voltage characteristics were assessed and compared to flat devices which comprised the equivalent ZnO/P3HT/PEDOT:PSS film sequence. However, the photonic crystal devices performed worse (Figure 5.9 a). As the absorption spectrum shows (Figure 5.9 b), the P3HT film in flat and microstructured devices absorbs more than 80% of the incident light between 400 and 630 nm, but the poor current-voltage characteristics imply that charge collection in these devices remained inefficient. The diminished charge collection may result from the absence of a ZnO:Al TCO electrode layer and a hole-transporting PEDOT:PSS film in the bulk of the micro-porous structure. This forces photo-generated holes to traverse several micrometer through the P3HT film to the electrode in comparison to 100–200 nm in the bilayer device and results in an increased susceptibility to charge recombination.

Please note that in comparison to the bilayer reference device the performance of the photonic crystal device was very inconsistent between repeated experiments, which suggested that they were susceptible to shortages through the polymer films. With the aim to prevent these shortages, devices with a very thick P3HT film were produced by soaking the ZnO microstructure with 50 µl of 80 mg/ml P3HT at 150°C for 15 min. However the FF of these devices degraded. In summary, out of 21 tested devices the best photonic crystal device comprised a 180 nm thick ZnO shell (incl. ZnO blocking layer), a P3HT film spun from a 20 mg/ml solution, and two PEDOT:PSS films that were added sequentially from the two dispersions Clevios P-VP-AI-4083 supplemented with 1% Hellmanex and Clevios P (Figure 5.9 a). The best flat bilayer device consisted of a 30 nm ZnO layer, a P3HT film spun from 30 mg/ml solution and a PEDOT:PSS film spin-coated at 1000 rpm for 30 sec from the Clevios P dispersion with 1% Hellmanex (Figure 5.9 a).

5.5 Discussion

As described in Chapter 4, ZnO:Al films grown by ALD loose their conductivity during calcination and sintering processes at 500°C. For that reason the transparent electrode layer in the initially proposed photonic crystal solar cell device had to be omitted. According to Scheme 1 on page 38, TiO_2 and ZnO photonic crystal structures were produced by holographic lithography and atomic layer deposition and were included in DSSC and organic-inorganic hybrid solar cell devices respectively.

TiO_2 photonic crystal structures could be produced 30 nm thin, resulting in a 90 nm TiO_2 shell structure after adding a 30 nm ALD blocking layer. The 90 nm TiO_2 shell structure and a photonic crystal TiO_2 inverse replica structure were included in two different DSSC devices, which were characterized and compared to a nanocrystalline TiO_2 DSSC reference device. The photonic crystal TiO_2 shell device provided an approximately two times larger power conversion efficiency η and short-circuit current density J_{sc} than the TiO_2 replica device, which was attributed to the enhanced roughness factor of the shell structure. Comparing the current-voltage characteristics of both photonic crystal devices to those of the nanocrystalline device suggested overestimation of their roughness factors due to macroscopic cracks observed with the SEM (in Section 3.5.4). Photo-current and photo-voltage transient measurements showed an order of magnitude larger charge diffusion constant in the photonic crystal devices compared to the nanocrystalline device. The charge diffusion length in the nanocrystalline device was twofold and threefold smaller compared to the photonic crystal replica and shell structures respectively. This charge transport enhancement in the photonic crystal devices was attributed to the larger crystallite size of the TiO_2 ALD films. The peaks in the measured EQE of all devices corresponded with the absorbance peaks of the N-719 dye. The attempt to combine the superior charge transport properties of the photonic crystal TiO_2 structure with the large surface area of a nanocrystalline TiO_2 film failed. Instead of filling the pores of the photonic crystal structure, the TiO_2 nano-particulate paste formed a layer on the top surface of the micro-structure regardless of concentration and composition of the paste. Whether the prepared pastes contained ethyl-cellulose, α-terpineol and ethanol, such as the commercial Dyesol paste, or only TiO_2 particles and ethanol, the result was identical.

Two types of ZnO-polymer photonic crystal devices were also developed and their performance compared to a flat bilayer device with equivalent material layer sequence. One photonic crystal device was completely filled with P3HT and the other contained a conformal layer of P3HT and was covered by a PEDOT:PSS film. As SEM images showed the PEDOT:PSS film remained on the top surface of the micro-structure instead of permeating its pores. However the performance of each type of ZnO photonic crystal device was inferior to the bilayer device despite comparable absorption >80% of the incident light in both devices. The lower FF and J_{sc} in the photonic crystal device suggested that its poor performance resulted from space charge build-up which led to a reduced charge dissociation rate at the donor acceptor interface. This was accompanied with enhanced possibility for charge recombination due to longer distances for photo-generated holes traveling through the P3HT film to the electrode. Compared to the bilayer reference device, photonic crystal device performance behaved inconsistently with respect to P3HT film thickness and type of PEDOT:PSS dispersion used. This was attributed to short-circuits through the polymer layers.

6 Conclusion

Solar energy is a promising non-polluting, renewable energy resource. Photovoltaic technologies such as organic and dye-sensitized solar cells facilitate low-cost manufacture, but their limited power-conversion efficiency prevents them from becoming economically viable. The multi-layer photonic crystal solar cell, introduced in this thesis, complies with the demands of low-cost manufacture and has the potential to reduce the losses occurring in these solar cell devices. The geometry of the photonic crystal structure has the advantage of providing direct conduction pathways and keeping the thickness of the absorbing layer at the order of its exciton diffusion length without sacrificing absorption. The other advantage of the photonic crystal solar cell is that its optical properties can be designed to increase the optical absorption length and minimize radiative recombination losses by matching the acceptance angles of incident and emitted radiation cones.

This thesis shows that such a solar cell can be produced by the techniques of holographic lithography, atomic layer deposition, and solution processing. For this purpose an ALD apparatus was constructed and holographic lithography was adapted to produce uniform and large enough photonic crystal polymer structures. These structures were thermally stabilized to be used as templates for ALD processes, which required processing temperatures in the range 100–200°C. These stabilized templates suffered from macroscopic cracks emerging above 100°C, because during holographic lithography fluctuations in the laser pulse profile created modulations of the fill fraction in the developed template. The main effect of these cracks was to reduce the roughness factor of the templates, which were still applicable for solar cell device fabrication. ALD processes for the growth of TiO_2, ZnO, Al_2O_3, ZnO:Al, and Zr_3N_4 were established and these materials were successfully grown on the developed photonic crystal templates. The attempt to produce photonic crystals with refractive index contrast larger than 3:1 failed because water contamination in the ammonia feed resulted in oxygen impurities in the Zr_3N_4 films and lowered the refractive index to 2.2. ALD of the metal oxides for solar cell device fabrication required removal of the polymer template by calcination at 500°C. The calcination process was used to sinter the amorphous TiO_2 films to poly-crystalline anatase with a crystallite size of 105 nm. ZnO and ZnO:Al films were deposited as crystalline zincite with a preferential orientation but possessed strain, which could not be released by sintering. The ZnO:Al films grown between 160–200°C exhibited a resistivity below $4\,\mathrm{m\Omega\,cm}$, but due to oxidation in the calcination process these films lost their conductivity. This loss could not be diminished in a 2% hydrogen/nitrogen atmosphere so that it was not possible to use a TCO electrode as encouraged in the initially proposed solar cell device. The produced solar cell devices comprised TiO_2 and ZnO photonic crystal structures which acted as electron transporters in TiO_2 DSSC and ZnO-P3HT solar cell devices respectively.

TiO_2 DSSC devices based on a 90 nm photonic crystal shell structure provided an approximately two times larger power conversion efficiency and short-circuit current density than the device that was based on a TiO_2 photonic crystal inverse replica structure. This effect was attributed to a larger density of dye molecules in the shell structure resulting from its enhanced roughness factor. However, in comparison to the nanocrystalline reference device, the current-voltage characteristics of both photonic crystal devices suggested overestimation of their roughness factors resulting from the macroscopic cracks in the templates. The photonic crystal devices featured an order of magnitude larger charge diffusion constant compared with the nanocrystalline device, resulting in a twofold and threefold larger charge diffusion length for photonic crystal replica and shell structures respectively. This charge transport enhancement in the photonic crystal devices was attributed to the larger crystallite size of the TiO_2 ALD films. The plan to combine the superior charge transport properties of the photonic crystal TiO_2 structure with the large surface area of a nanocrystalline TiO_2 film failed. Various TiO_2 nano-particulate pastes were prepared for filling the pores of the photonic crystal structure, but they formed a layer on the top surface of the micro-structure instead, regardless of concentration and composition of the paste.

Fabrication of an organic-inorganic hybrid solar cell device that consisted of a $PC_{60}BA$ grafted ZnO photonic crystal structure acting as electron-transporter which is coated with a conformal absorber layer of P3HT, and covered by a hole-transporting PEDOT:PSS film was unsuccessful. SEM images confirmed that the PEDOT:PSS film remained on the top surface of the micro-structure instead of permeating its pores, regardless of the solution processing conditions. The resulting solar devices performed worse than a flat reference device with equivalent material layer sequence despite comparable absorption >80% of the incident light in both devices. The lower FF and J_{sc} in the photonic crystal device was explained by (i) a space charge build-up leading to a reduced charge dissociation rate at the donor acceptor interface and (ii) an enhanced possibility for charge recombination due to longer distances for photo-generated holes traveling through the P3HT film to the electrode. The ZnO photonic crystal devices performance also behaved inconsistently with respect to P3HT film thickness and type of PEDOT:PSS dispersion used: this was attributed to short-circuits through the polymer layers.

Despite the limited performance of the produced devices, the experiments in this thesis showed that it is feasible to create DSSC and organic-inorganic hybrid photonic crystal solar cell devices by combining the techniques of holographic lithography, atomic layer deposition, and solution processing, which are suitable for low-cost manufacture. The next section presents further work required to overcome the observed limitations.

Further Work

Because ZnO:Al proved to be unsuitable for creating an electrode layer in the solar cell device proposed in this thesis, another TCO must be found that can be introduced as a conformal electrode layer in the bulk of the photonic crystal structure and maintain its conductivity up to 500°C in air. A TCO that is compatible with this environment is fluorine doped tin oxide SnO_2:F (FTO) [286]. Yang et al. [287] recently showed that precursors for a FTO spray pyrolysis process [288] can be used to replicate a polystyrene opal structure with FTO. This process would need to be adapted for the SU-8 templates used in this thesis. Another promising method to produce transparent tin oxide films is the low-temperature ALD process which produces SnO_x films with $\approx 10^{-2}\,\Omega\,\text{cm}$ resistivity at 100–200°C from the precursors hydrogen peroxide and N^2,N^3-di-tert-butyl-butane-2,3-diamidotin(II) ($C_{12}H_{26}N_2Sn$) [289]. In order to further reduce the resistivity of these films would be to find a suitable fluorine dopant precursor for this ALD process.

In order to complete the photonic crystal organic-inorganic bulk-heterojunction (as in Figure 2.14 on page 37), a conformal PEDOT:PSS film must be in direct interfacial contact with the absorbing P3HT layer in the bulk of the photonic crystal device. Because the solution processed P3HT appeared to have short-circuits and the PEDOT:PSS film did not permeate the photonic crystal bulk, different deposition techniques must be developed. A possible route is the development of a vapor deposition process for each polymer that is based on molecular layer deposition (MLD) (the ALD analog for molecules) or soft landing of complex molecules, which allows deposition without molecule degradation [290]. So far Kovacik et al. [291] have demonstrated functional bilayer heterojunctions that were created by thermal evaporation of P3HT and C_{60} at 360°C. They showed that to a large extent the conjugation of the P3HT molecules remained intact at these processing temperatures, but material degradation caused loss in molecular weight and was accompanied by a blue shift in absorption. Since thermal evaporation can only produce conformal films on flat substrates, progression to an MLD process for P3HT would be necessary for growth of conformal films with controllable thickness on high aspect-ratio structures. Lock et al. [292] developed an oxidative chemical vapor deposition (oCVD) process for PEDOT as an alternative to conventional solution-based processing of PEDOT:PSS films. The oCVD process is based on oxidative polymerization of EDOT precursor monomers which form conjugated

PEDOT in the presence of the oxidant ferric chloride Fe(III)Cl_3. Thus, the PEDOT process does not rely on solvents which limit the choice of substrates, and the use of acidic poly(styrenesulfonate) (PSS) which is a likely source of corrosion and device degradation becomes redundant [292]. The researchers also demonstrated the growth of conformal PEDOT films on paper towel fibers and flexible substrates. The resulting PEDOT films showed up to 35× larger conductivity than PEDOT:PSS films grown from solution [235; 292]. Im et al. [236] showed that the temperature of the PEDOT oCVD process can be used to control doping level, work function [236], and conductivity [235] of the deposited films.

Due to the limited absorption spectrum of P3HT, the photonic crystal device could be further extended to a tandem solar cell by adding a stack of multiple absorbing layers with band-gaps different to that (1.9 eV) of P3HT (as described in Section 2.1.4 on page 22). The resulting device would provide a larger absorption efficiency and higher output voltage. The low-bandgap polymers PCPDTBT (1.46 eV) and PTB7 (1.6 eV) would be suitable, but their deposition technique would also need to be adapted to produce conformal films in the photonic crystal device.

The absorption efficiency of the device could be also increased by optimizing its photonic band-structure so that localized and slow-light modes exist near the boundary of the absorption spectrum of the absorber. Additionally the band-structure could be utilized to reduce radiative recombination losses by angularly confining the emission of light modes. However, these endeavors require a defect-free photonic crystal polymer template. Thus it is necessary to prevent the emergence of macroscopic cracks in the polymer template at elevated temperatures. For this purpose the beam quality of the laser used for holographic lithography would have to be removed e.g. with a spatial filter. However, at the required pulse energy of the used UV-laser spatial filtering is a challenge. A different photoresist chemistry might allow less energetic photo-resist exposures, and use of a CW gas laser [180] rather than a solid-state laser would improve beam quality dramatically.

Appendix

A Abbreviations

Abbreviation	Denotation
ALD	atomic layer deposition
BAPEN	N,N'-Bis(3-aminopropyl)ethylenediamine
CVD	chemical vapor deposition
DSSC	dye-sensitized solar cell
FTO	fluorine doped tin oxide
ITO	indium doped tin oxide
MEH-PPV	poly[2-methoxy,5-(2'-ethyl-hexyloxy)-p-phenylene vinylene]
MLD	molecular layer deposition
N-719	di-tetrabutylammonium cis-bis(isothiocyanato)bis(2,2'-bipyridyl-4,4'-dicarboxylato)ruthenium(II)
P3HT	poly(3-hexylthiophene)
PBTTPD	poly{bi(dodecyl)thiophene-thieno[3,4-c]pyrrole-4,6-dione}
$PC_{60}BM$	[6,6]-phenyl-C_{61}-butyric acid methyl ester
$PC_{70}BM$	[6,6]-phenyl-C_{71}-butyric acid methyl ester
PCDTBT	poly[N-900-hepta-decanyl-2,7-carbazole-alt-5,5-(40,70-di-2-thienyl-20,10,30-benzothiadiazole)
PCPDTBT	poly[2,6-(4,4-bis-(2-ethylhexyl)-4H-cyclopenta[2,1-b;3,4-b]-dithiophene)-alt-4,7-(2,1,3-benzothiadiazole)]

.... *Continued on next page* ....

Abbreviation	**Denotation**
PEDOT:PSS	poly(3,4-ethylenedioxythiophene):polystyrene sulfonate
PTB7	poly{[4,8-bis[(2-ethylhexyl)oxy]benzo[1,2-b:4,5-b']dithiophene-2,6-diyl][3-fluoro-2-[(2-ethylhexyl)carbonyl]thieno[3,4-b]thiophenediyl]}
SEM	scanning electron microscopy
SU-8	negative-tone epoxide photo-resist
TCO	transparent conducting oxide
XRD	X-ray diffraction

……

B Solvent Exchange for Photo-resist Development

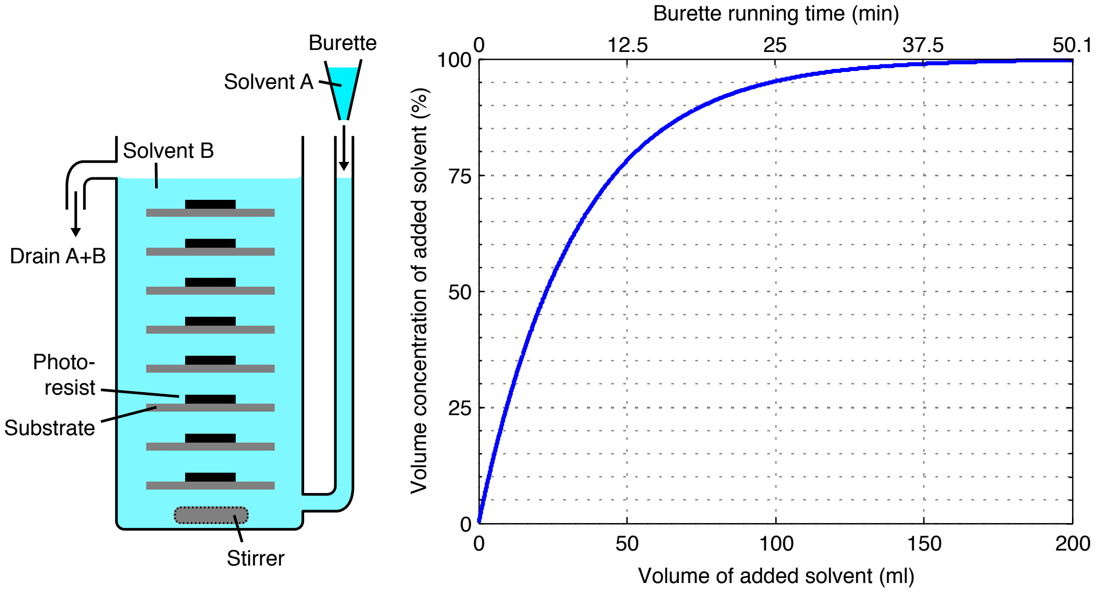

Figure 6.1: Schematic of the reservoir which contained samples and magnetic stirrer that were used to exchange the solvent PGMEA (solvent B) after polymerization of the photo-resist by dropping propan-2-ol (solvent A) with a burette into the reservoir. In order to estimate the time and amount of propan-2-ol needed to replace PGMEA, the volume concentration of propan-2-ol in the reservoir is plotted against the added volume and the burette running time.

As described in section 3.2.3 on page 49, the solvent PGMEA that dissolves the unpolymerized regions in the developed photo-resist was slowly removed by exchanging it with another solvent, propan-2-ol, in a burette (Figure 6.1, left). A reservoir with volume $V_{\mathrm{res}} = 33\,\mathrm{ml}$ contained the developed photo-resists in a bath of PGMEA. The burette released $V_{\mathrm{drop}} = 22.2\,\mu\mathrm{l}$ large drops of propan-2-ol into the reservoir at a drop rate $\omega_{\mathrm{drop}} \approx 3\,\mathrm{Hz}$. Propan-2-ol was mixed with PGMEA by a magnetic stirrer and this mixture drained at an over-flow.

In order to determine the volume of propan-2-ol and the burette running time that is needed to exchange PGMEA in the reservoir, this volumetric solvent exchange process was described by the recursion relation

$$V_n = \left(1 - \frac{V_{\mathrm{drop}}}{V_{\mathrm{res}} + V_{\mathrm{drop}}}\right) \cdot (V_{\mathrm{drop}} + V_{n-1}) \tag{6.1}$$

which was solved for a sufficiently large number of drops, where V_n is the volume of propan-2-ol in the reservoir after adding n drops. The plot of the volume concentration of propan-2-ol in the reservoir, V_n/V_{res}, with respect to the added volume of the solvent, $n \cdot V_{\mathrm{drop}}$, shows that 95% of PGMEA is replaced by dropping ≈100 ml of propan-2-ol into the reservoir in ≈25 min and 99% PGMEA is exchanged by ≈150 ml propan-2-ol in ≈38 min (Figure 6.1, right).

C Schematic Diagrams and Parts List of ALD Apparatus

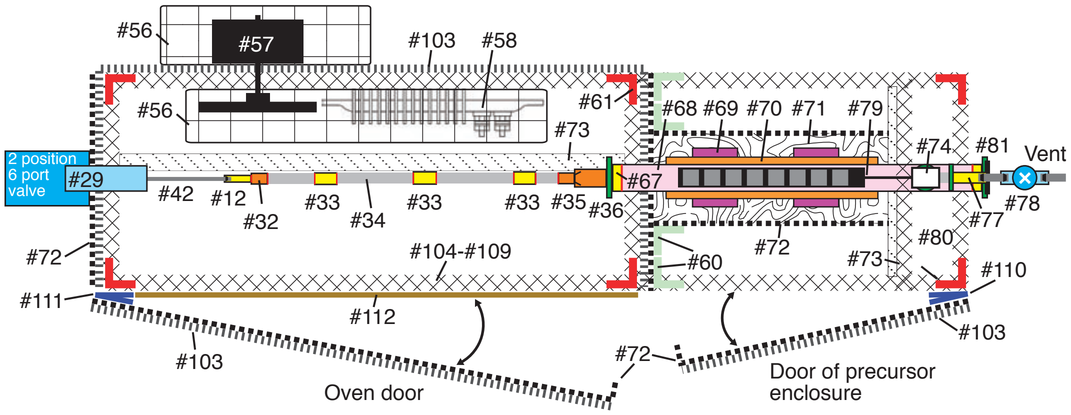

Figure 6.2: Top view diagram of ALD apparatus at scale 1:9 with item numbers from the parts list below.

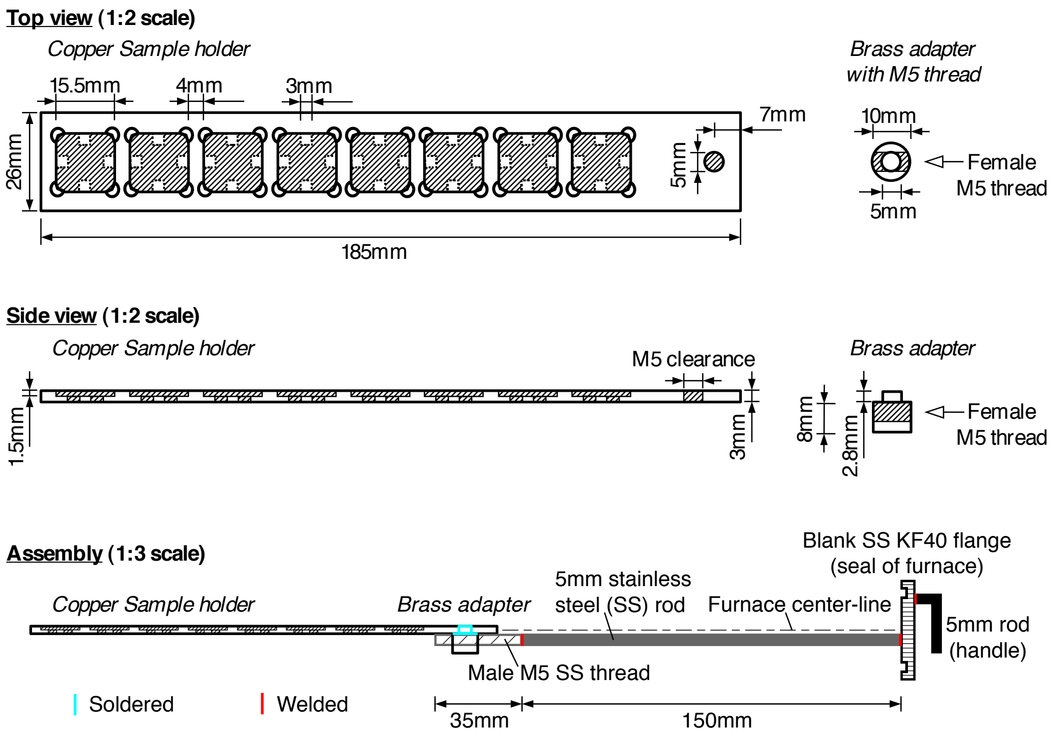

Figure 6.3: Schematic diagram of sample holder assembly for ALD apparatus.

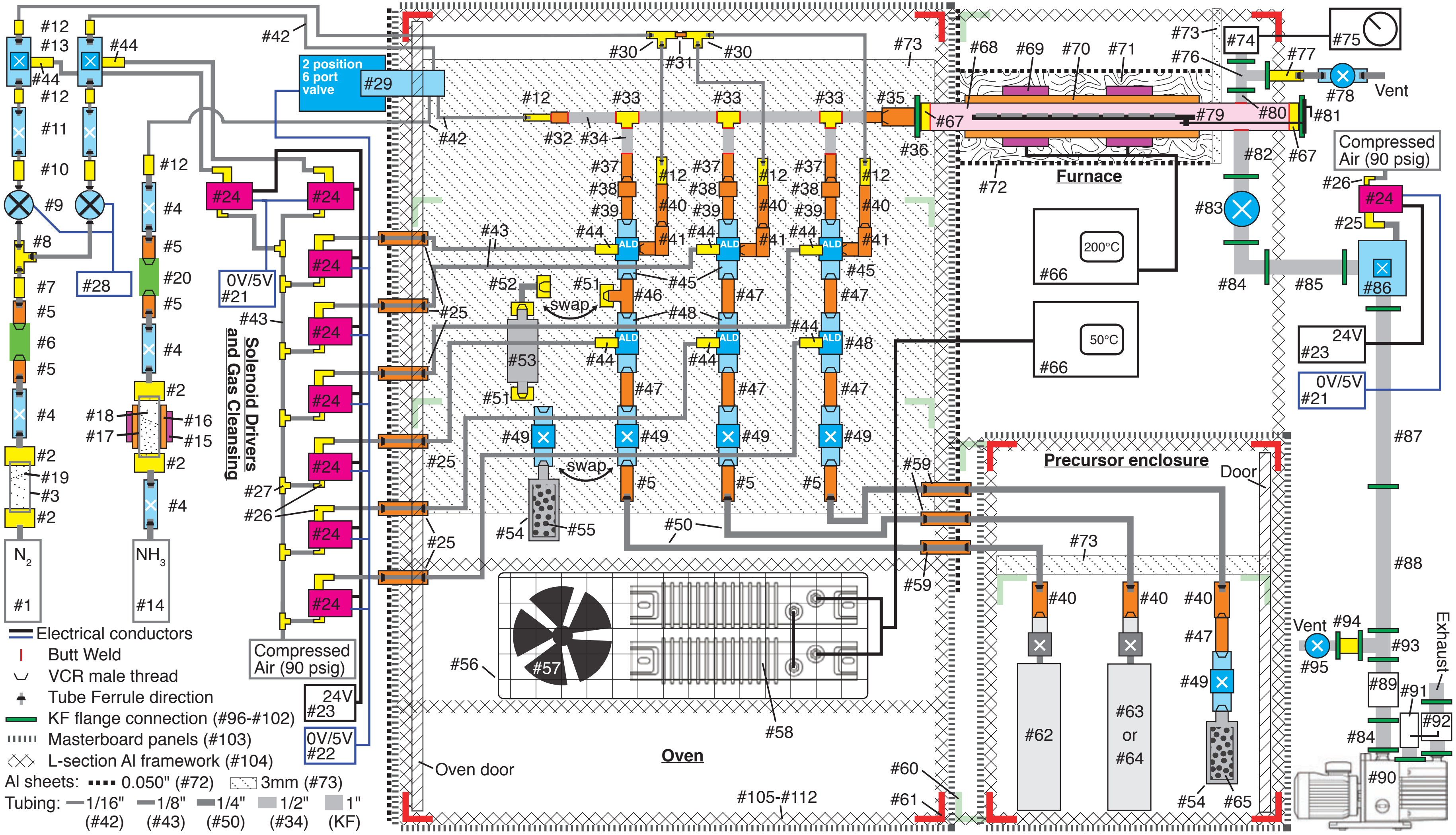

Figure 6.4: Front view diagram of ALD apparatus at scale 1:7 with item numbers from the parts list below.

Parts list of ALD apparatus

Item	Qty.	Description	Function	Brand	Model / Part No.
#1	1	Ultra high purity nitrogen, N6.0, size L, 200 bar	Inert purging gas regulated to 1.3 bar	BOC	296 180-L
#2	4	3/4” to 1/4” reducer	Connect desiccant container to gas feed	Swagelok	SS-1210-6-4
#3	1	6” long polished 3/4” SS tube	Reservior of nitrogen gas desiccant	Swagelok	SS-T12-S-065-20
#4	4	2-way On-Off Valves, 1/4” tube unions	Gas Line stop valves	Swagelok	SS-43GS4
#5	7	1/4” Male VCR to 1/4” Tube Connector	Source input coupling	Swagelok	SS-4-VCR-6-400
#6	1	Gatekeeper Inert Gas Purifier	Purify nitrogen to <1 ppb impurities	Entegris	CE35KFI4R
#7	1	1/4” to 1/8” Reducer	1/8” Gas line input feed ports	Swagelok	SS-400-R-2
#8	1	1/8” Tee Union	Nitrogen line branches	Swagelok	SS-200-3
#9	2	Nitrogen mass flow controller	Measure and control nitrogen gas flow	Brooks Instrument	5850 TR
#10	2	1/8” to 1/16” Reducer	1/16” Gas line input feed ports	Swagelok	SS-200-R-1
#11	2	2-way On-Off Valves, 1/16” tube unions	Gas Line stop valves	Swagelok	SS-41GS1
#12	9	1/4” to 1/16” Reducer	1/16” Gas line input feed ports	Swagelok	SS-100-R-4
#13	2	1/4” Female VCR pneumatic Diaphragm-Sealed Valve	Stop-valves for nitrogen line	Swagelok	6LVV-DPS4-0
#14	5Kg	Electronic Grade Ammonia	Precursor for zirconium nitride growth process, regulated to 1.3 bar	BOC Edwards	CAS 7664-41-7
#15	2	Band heater, 38mm, 250W, 230V	For outgasing molecular sieve	RS	353-4663
#16	1	100mm long machined copper tube, outer diameter 38mm, inner diameter 3/4”	Distribute heat along molecular sieve container	custom-made	–
#17	1	5” long polished 3/4” SS tube	Reservoir of ammonia feed desiccant	Swagelok	SS-T12-S-065-20
#18	1	Molecular Sieves, 3Å, beads, 8-12 mesh	Ammonia feed desiccant	Sigma-Aldrich	20,858-2
#19	1	di-Phosphorus pentoxide	Nitrogen feed desiccant	VWR	21411.230
#20	1	Hydride Gas Purifier	Purify ammonia to <0.4 ppb impurities	SAES Getters	MC1-702F
#21	1	USB data acquisition device	Open / close command to Solenoid valves	LabJack	U3-HV
#22	1	USB-based 24-channel digital I/O device	Open / close command to Solenoid valves	Measurement Computing	USB-1024LS
#23	1	Custom-made 24V power supply	Power supply for Solenoid Valves	Physics Electronics	–

…… *Parts list continued on next page* ……

Item	Qty.	Description	Function	Brand	Model / Part No
#24	9	Solenoid Pilot Valves (not assembled onto valves)	Solenoids for 6 ALD, 2 nitrogen, and vacuum stop actuators	MAC	34C-AAA-GDFC-1KT
#25	6	Bulkhead Union, 1/8”	Connects two 1/8” tubes through masterboard panel for optimum sealing between fitting and panel	Swagelok	SS-200-61
#26	18	1/8” Push-Quick Threaded Male Elbow	Connection of 1/8” tubing to solenoid valves	Clippard	PQ-ME04N-PKG
#27	8	1/8” Push-to-connect Union Tee	Connect 1/8” compressed air line tubing	Legris	3104 53 00
#28	1	Brooks Instrument power and control unit	Power and control Mass Flow Controllers	Brooks Instrument	5878
#29	1	Six-port two-position gas chromatography valve with Microelectric Valve Actuator	Release 50 µl ammonia from reactive gas feed into manifold via 1/16” connections	VICI	EH2C6WE
#30	2	1/16” Tee Union	Nitrogen line branches	Swagelok	SS-100-3
#31	1	1/16” Port Connector	Nitrogen line branches	Swagelok	SS-101-PC
#32	1	1/2” to 1/4” Butt Weld Reducing Union	Manifold reduction to gas input gland	Swagelok	316L-8TB7-6-4
#33	3	1/2” Butt Weld Union Tee	Manifold T pieces	Swagelok	6LV-8MW-3
#34	50cm	1/2” Stainless Steel tubing, wall thickness 0.035”	ALD manifold tubing	Swagelok	SS-T8-S-035-6ME
#35	1	1/2” Butt Weld Short VCR Gland	Manifold to VCR furnace coupling	Swagelok	6LV-8-VCR-3S-8TB3
#36	1	KF40 to 1/2” VCR Male	KF furnace coupling to 1/2” VCR adapter	Swagelok	JNWMVCR4050
#37	3	1/2” Butt Weld Long VCR Gland	Manifold to source line VCR couplings	Swagelok	6LV-8-VCR-3-8TB2
#38	4	1/2 in. Female Nut	Manifold VCR couplings	Swagelok	SS-8-VCR-1
#39	3	1/2” Male VCR to 1/4” VCR Male Reducing Union	VCR reduction from manifold to ALD valves	Swagelok	SS-8-VCR-6-DM-4
#40	6	Welded 1/4” Female VCR to 1/4” Tube Connector	Couple Source Reservoirs to 1/4“ feed lines and nitrogen lines to ALD actuators	Swagelok	SS-4-WVCR-6-400
#41	3	1/4” VCR Union Elbow Body	Couple nitrogen lines to ALD actuators	Swagelok	SS-4-VCR-9
#42	4m	1/16” Stainless steel tubing, wall thickness 0.014”	Tubing for inert and reactive gas feeds	Swagelok	SS-T1-S-014-6ME
#43	9m	1/8” Stainless steel tubing, wall thickness 0.028”	Tubing for compressed air feeds	Swagelok	SS-T2-S-028-6ME
#44	8	Brass 1/8” elbows, Male NPT Thread	Compressed air line coupling to actuators	Swagelok	B-200-2-2
#45	3	1/4” ALD valves with three female VCR ports	ALD source release valves with nitrogen purge connection	Swagelok	6LVV-ALD3G333P-C

Parts list continued on next page

Item	Qty.	Description	Function	Brand	Model / Part No
#46	1	VCR Union Tee	Couplers between ALD Valve pairs and port for larger precursor buffer volume	Swagelok	SS-4-VCR-T
#47	6	Male 1/4” VCR Union	Couplers between ALD Valve pairs	Swagelok	SS-4-VCR-6-DM
#48	3	1/4” ALD valves with two female VCR ports	ALD dose valves for three source lines	Swagelok	6LVV-ALD3FR4-P-CV
#49	5	1/4” Female VCR Diaphragm Valve	Source Shut off valves	Swagelok	6LVV-DPVFR4-P
#50	6m	1/4” Stainless steel tubing, wall thickness 0.035”	Tubing for ALD manifold and inert and reactive gas feeds	Swagelok	SS-T4-S-035-6ME
#51	1	VCR cap	Close open VCR tubes	Swagelok	SS-4-VCR-CP
#52	1	Elbow VCR female	Expand precursor buffer volume	Swagelok	6LV-4-WVCR-9-DF
#53	1	25ml cylinder with two male VCR ports	Larger buffer volume for Zr precursor	Swagelok	SS-4CD-TW-25
#54	2	25ml sample cylinder with one VCR port	Reserviors for zirconium compound and water	Swagelok	SS-4CS-TW-25
#55	1	Tetrakis(dimethylamido)zirconium(iv), 99.99+%, electronic grade	Precursor for zirconium nitride growth process	Aldrich	579211-5G
#56	1	Perforated Aluminium sheet with 6mm holes	Safety guard	Steelexpress	A065
#57	1	Hot air blower	Heat distribution	ebm-papst	R2K150-AC01-15
#58	2	Ceramic insul finned heater, 750W, 12”	Heater for oven	RS	829-788
#59	3	Bulkhead Union, 1/4”	Connects two 1/4” tubes through masterboard panel for optimum sealing between fitting and panel	Swagelok	SS-400-61
#60	14	Corner braces 50mm	Parts for ALD housing metal framework	B&Q	3211427
#61	34	Corner plates, 75mm	Parts for ALD housing metal framework	B&Q	3209356
#62	1	Diethylzinc reservoir	Precursor for zinc oxide (ZnO) growth process	SAFC HITEC	CAS 557-20-0
#63	1	Trimethylaluminium reservoir	Precursor for Al doped ZnO growth process	SAFC HITEC	CAS 75-24-1
#64	1	Titanium tetrachloride reservoir	Precursor for titanium dioxide growth process	SAFC HITEC	CAS 7550-45-0
#65	25ml	Deionized water outgased at low pressure and <273K	Precursor for all oxide growth processes	–	–
#66	2	2216e Eurotherm Temperature Controller with K-type thermocouple	Temperature controllers for oven heating elements and furnace band heaters	ICL Department Oxford	ICL-167
#67	2	Blank KF40 flange bored to internal diameter of furnace tube and welded by workshop	Connect furnace tube to ALD manifold	Swagelok	JNWB40
#68	1	1.25” Stainless Steel tubing	Furnace tubing	Swagelok	SS-T20-S-120-20
#69	2	Band heater, 42mm, 300W, 230V	Heating furnace tube	RS	353-4685

Parts list continued on next page

Item	Qty.	Description	Function	Brand	Model / Part No
#70	1	21cm long copper tube, outer diameter 42mm, inner diameter 1.25”	Distribute heat along furnace tube	custom-made	–
#71	>100g	Glass whool	Furnace heat insulator	–	Glass workshop stock item
#72	3	0.050” thick aluminium sheet	100mm wide encapsulation of furnace insulation and protection of masterboard panels	custom-made	–
#73	3	3mm thick aluminium sheet	Fixation of ALD manifold and furnace to housing	custom-made	–
#74	1	Pirani Vacuum Gauge	Pressure gauge	Edwards	PRM10
#75	1	Pirani gauge controller	Pressure gauge controller and display	Edwards	Controller 503
#76	1	KF10 Tee Union	Connect Pirani gauge and vent valve to furnace	Swagelok	JNW3T10
#77	1	KF10 to Swagelok 1/4” Tube Fitting	Connect vent valve to furnace tubing	Swagelok	JNWSWAG1014
#78	1	Integral Bonnet Needle Valve with 1/4” tube fittings	Manifold vent valve	Swagelok	SS-1RS4
#79	1	Copper piece with 15.5mm square pockets	Sample holder, see drawing of sample holder assembly in Figure 6.3 on page 116	custom-made	–
#80	1	KF10 Half Nipple Weld Flange, Stainless Steel	Furnace tubing	Swagelok	JNW1N10
#81	1	KF40 blank flange with handle and attached to sample holder	Seal of furnace, see schematic of sample holder assembly in Figure 6.3 on page 116	Swagelok	JNWB40
#82	1	KF25 Long Weld Flange, Stainless Steel	Furnace tubing	Swagelok	JNWFL25
#83	1	1” KF25 Speedivalve, SP25K, Fluoroelastomer Diaphram	Manually isolate furnace from vacuum pump	Edwards	C33355000
#84	2	90° KF25 elbow	Line to vacuum pump	Swagelok	JNW2E25
#85	1	4” KF25 long Nipple	Line to vacuum pump	Swagelok	JNW2N25
#86	1	Pneumatic single acting cylinder, spring return pipeline valve, PV25PKA B	Pneumatic vacuum isolation valve	Edwards	C41311000
#87	1	20” long 1” pipeline welded to two KF25 flanges	Line to vacuum pump	Swagelok	JNWB2510
#88	1	NW25 Flexible Pipeline 1000mm	Flexible line to vacuum pump	Edwards	C10514287
#89	1	Foreline trap	Prevents gas impurities in vacuum line	Edwards	FL20K
#90	1	Rotary vacuum pump	Vacuum pump	Edwards	RV8
#91	1	Adjustable Gas Ballast Oil Return Kit	Returns oil from mist filter to the pump	Edwards	A50523000

Parts list continued on next page

Item	**Qty.**	**Description**	**Function**	**Brand**	**Model / Part No**
#92	1	Oil mist filter	Collects oil vapour at pump exhaust	Edwards	EMF20
#93	1	KF25 Tee Union	Connect Pump and vent valve to vacuum line	Swagelok	JNW3T25
#94	1	KF25 to KF16 reducer	Connect vent valve to vacuum line	Swagelok	JNW2NRC2516
#95	1	KF 3/4" Speedivalve, SP16K, Nitrile Diaphragm	Manually vent KF tubing to furnace	Edwards	C33205000
#96	4	KF10 and KF16 Aluminium Clamp	Connect Pirani gauge and vent valve to furnace, and vent valve to vacuum line	Swagelok	JNWCP16
#97	3	KF10 Aluminium Centering Ring	Connect Pirani gauge and vent valve to furnace	Swagelok	JNWCRAB10
#98	1	KF16 Aluminium Centering Ring	Connect vent valve to vacuum line	Swagelok	JNWCRAB16
#99	13	KF25 Aluminium Clamp	Assemble line to vacuum pump	Swagelok	JNWCP25
#100	13	KF25 Aluminium Centering Ring	Assemble line to vacuum pump	Swagelok	JNWCRAB25
#101	2	KF40 Aluminium Clamp	Seal furnace and connect to manifold	Swagelok	JNWCP40
#102	2	KF40 Aluminium Centering Ring	Seal furnace and connect to manifold	Swagelok	JNWCRAB40
#103	1	Masterboard 9mm thick, size 2440mm × 1220mm	ALD housing side panels	Jewson	PMBB0984
#104	11.4m	Aluminium Equal Angles 1" × 1" × 1/8"	Parts for ALD housing metal framework	Clickmetal	AAE1001
#105	1	M4 Flat Washers	Parts for ALD housing metal framework	Screw Fix	14391
#106	5	M5 Penny Washers 5x25mm	Parts for ALD housing metal framework	Screw Fix	64837
#107	30	M5 Large Flat Washers	Parts for ALD housing metal framework	Screw Fix	64837
#108	302	M4 countersink Screws, 20mm long	Parts for ALD housing metal framework	Screw Fix	96085-0050
#109	302	M4 Hex Nuts	Parts for ALD housing metal framework	Screw Fix	74085
#110	1	60cm cont hinge	Hinge for oven door	B&Q	3208229
#111	1	90cm cont hinge	Hinge for precursor housing door	B&Q	3207352
#112	1	Self-adhesive EPDM Rubber P Strip 6mm × 20m	Gap seal for ALD oven door	Screw Fix	88076

D Van-der-Pauw Method

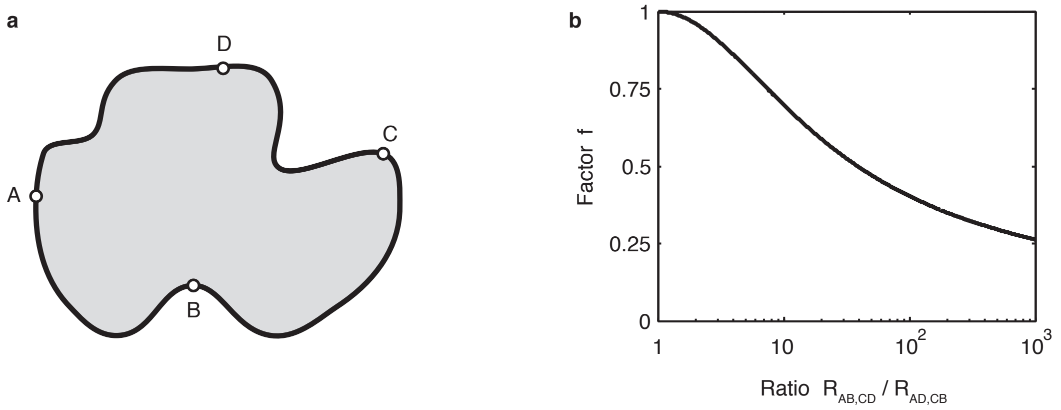

Figure 6.5: Four-point probe that measures the sheet resistance of a thin film (**a**). Function $f(R_{\mathrm{AB,CD}}/R_{\mathrm{AD,CB}})$ from Equations (6.2) and (6.3) (**b**).

The resistivity of ZnO:Al films was determined by measuring their sheet resistance with a Keithley Multimeter 2000 and a custom-made 4-point probe at four silver paint contacts at the periphery of the film. The Multimeter determines the sheet resistance $R_{\mathrm{AB,CD}} = V_{\mathrm{CD}}/i_{\mathrm{AB}}$ by sending a current i_{AB} from contact A to contact B and measuring the voltage V_{CD} between the contacts C and D (Figure 6.5 a). The resistivity was determined from the measured sheet resistance and film thickness d by utilizing the van-der-Pauw method. This technique works on arbitrary shapes with constant film thickness and requires measurement of two sheet resistances, $R_{\mathrm{AB,CD}}$ and $R_{\mathrm{AD,CB}}$, where one of the voltage contacts is swapped with a current contact [293]. According to van der Pauw [293], the resistivity is

$$\rho = \frac{\pi d}{\ln 2} \frac{R_{\mathrm{AB,CD}} + R_{\mathrm{AD,CB}}}{2} f \ , \tag{6.2}$$

where f is a function of the ratio $R_{\mathrm{AB,CD}}/R_{\mathrm{AD,CB}}$ and is determined from the relation

$$\cosh\left[\frac{R_{\mathrm{AB,CD}}/R_{\mathrm{AD,CB}} - 1}{R_{\mathrm{AB,CD}}/R_{\mathrm{AD,CB}} + 1} \frac{\ln 2}{f}\right] = \frac{1}{2} \exp \frac{\ln 2}{f} \tag{6.3}$$

(plotted in Figure 6.5 b).

E Solar Cell Device Fabrication

E.1 FTO substrate preparation

Scribing

Sheets of fluorine doped tin oxide (FTO) glass (Pilkington, TEC 15) were scribed with lines by using a glass cutter. These lines constituted a grid of 14 mm squares or 13-by-15 mm^2 oblongs for FTO substrates and counter electrodes respectively.

Sand-blasting Counter Electrodes

At this stage the FTO sheet for counter electrodes was protected with scotch tape. Approximately 1 mm wide holes were sand-blasted into each oblong of the FTO sheet. After sand-blasting, the FTO sheet was liberated from scotch tape so that it was ready for cleaning.

Cleaning and Breaking

All scribed FTO sheets were washed with a 2% solution of Hellmanex (Hellma-Analytics) in deionized water, rubbed with a toothbrush, rinsed with deionized water, air-dried, and kept for 10 min in an ultra-sonic bath of acetone. After this bath they were air-dried, rinsed with methanol, air-dried again, and finally oxygen plasma etched for 10 min at 200 W (Diener-electronic Pico). The cleaned FTO sheets were broken along the scribed lines on a wood handle of a cotton bud.

E.2 Iodine-iodide Electrolyte Recipe

The following ingredients composed the iodine-iodide electrolyte and shook for at least 3 hours at room temperature.

Amount	**Ingredient**
200 mg	1-butyl-3-methylimidazolium iodide
38 mg	iodine
66 mg	1-methyl benzimidizole
11.8 mg	guanidine thiacynate
1 ml	3-methoxypropionitrile

Acknowledgment

I am indebted to a number of people for their support during my DPhil. First of all I would like to thank Prof. Andrew Turberfield for supervising this exciting project. I am very grateful for his advice, the independence he gave me, always having time when help was needed, and his very helpful comments on the script. I appreciate his support for the UIMP Nanophotonic Summer School, the MRS Spring Meeting, and the Physics Meets Biology conference. I am also very thankful to Prof. Bob Denning for sharing his immense pool of knowledge. His advice on photoresists and guidance on building the ALD apparatus and establishing the ALD processes was invaluable. I thank David Sharp for the introduction to the holographic lithography technique in our lab and many precious discussions. Harpal Bharaj wrote the software program for the ALD apparatus and created the interface to the solenoid drivers. Thanks for this and various helpful discussions.

I thank Henry Snaith for the collaboration, his countless ideas, advice on solar cells, and sharing his laboratory. A number of people in Henry's group introduced me to various solar cell fabrication and device characterization techniques. For this I particularly thank Pablo Docampo, Mike Brown, James Ball, Mike Lee, Andy Hey, and Agnese Abrusci. I thank Robert Gunning for performing XRD measurements on ALD films.

The research workshop was of immeasurable value for building the ALD apparatus and many other devices. I am indebted to all the technicians of the mechanical workshop and particularly to Rob Harris, Simon Moulder, and Matt in the research workshop for their help and advice.

The following people at the Department of Chemistry shared their labs and offered helpful discussions for which I am very thankful. Robert Jacobs performed numerous ellipsometry measurements and provided access to his Surface Analysis Facility at the Chemistry Research Laboratory. Vladimir Kuznetsov allowed me to use his Hall measurement equipment and had important information on resistivity measurements of thin films. The reduction of ZnO:Al films was performed with a hydrogen furnace in Michael Hayward's lab.

I would like to thank the staff of the Materials Department: Steve Lett for his time and advice on using and modifying the argon ion mill in his sample preparation lab, Gabriella Chapman and Chris Salter for training on SEMs and sample preparation techniques, and Radka Chakalova for giving me access to the clean room and the reactive ion etcher in Begbroke.

I am deeply grateful to the Engineering and Physical Sciences Research Council (EPSRC), International Union for Vacuum Science Technique and Applications (IUVSTA), University of Oxford, and University College Oxford for their support.

During my time here in Oxfordshire I have made some truly good friends. In no particular order I am grateful to Kari and Rick Williamsons, Merav and Daniel Rotenberg, Ling Weng, Alex McGuire, Rabeea Assy, Susann and Christian Porth, Steph Egee, Tom Imison, Anne Robert, Gail Hayward and Chandra Sekar Ramanujan, Kate and Euan McCall, Gunnar Langfahl-Klabes, Meihua Zhang, Evangelos Syrigos, Paula Varela Tomasco, and Enrique González Villar for sharing plenty cheerful, comforting, inspiring, and supportive moments. I would also like to express my gratitude to Anne Kretzschmann and her family for their great support. Last but not least, I thank my parents Ingrid and Theo for their constant love and support, and inexhaustible cake supply.

Bibliography

[1] BP statistical review of world energy, `www.bp.com/statisticalreview`, 2012.

[2] Renewables 2012 global status report, `www.ren21.net`, 2012.

[3] O. Morton. Solar energy: A new day dawning?: Silicon valley sunrise. *Nature*, **443**:19–22, 2006.

[4] J. D. Joannopoulos, S. G. Johnson, J. N. Winn, and R. D. Meade. Photonic Crystals: Molding the Flow of Light (Second Edition). Princeton University Press, 2008.

[5] A. E. Becquerel. Mémoire sur les effets électriques produits sous l'influence des rayons solaires. *Comptes Rendus Acad. Sci. Paris*, **9**:561–570, 1839.

[6] J. Nelson. The physics of solar cells. Imperial College Press, 2003.

[7] P. Würfel. Physics of Solar Cells—From Principles to New Concepts. Wiley-VCH Verlag GmbH, 2005.

[8] G. Li, R. Zhu, and Y. Yang. Polymer solar cells. *Nat Photon*, **6**:153–161, 2012.

[9] W. Shockley and H. Queisser. Detailed balance limit of efficiency of p-n junction solar cells. *Journal of Applied Physics*, **32**:510–519, 1961.

[10] G. L. Araujo and A. Marti. Absolute limiting efficiencies for photovoltaic energy conversion. *Solar Energy Materials and Solar Cells*, **33**:213–240, 1994.

[11] Standard tables for reference solar spectral irradiances: Direct normal and hemispherical on 37 ° tilted surface. ASTM G173 - 03, 2003.

[12] `http://en.wikipedia.org/wiki/Solar_cell`, 2012.

[13] R. T. Ross and A. J. Nozik. Efficiency of hot-carrier solar energy converters. *Journal of Applied Physics*, **53**:3813–3818, 1982.

[14] P. Würfel. Solar energy conversion with hot electrons from impact ionisation. *Solar Energy Materials and Solar Cells*, **46**:43–52, 1997.

[15] D. M. Chapin, C. S. Fuller, and G. L. Pearson. A new silicon p-n junction photocell for converting solar radiation into electrical power. *Journal of Applied Physics*, **25**:676–677, 1954.

[16] J. Zhao, A. Wang, P. Altermatt, and M. A. Green. Twenty-four percent efficient silicon solar cells with double layer antireflection coatings and reduced resistance loss. *Applied Physics Letters*, **66**:3636–3638, 1995.

[17] J. Zhao, A. Wang, M. A. Green, and F. Ferrazza. 19.8% efficient "honeycomb" textured multicrystalline and 24.4% monocrystalline silicon solar cells. *Applied Physics Letters*, **73**:1991–1993, 1998.

[18] A. Goetzberger, C. Hebling, and H.-W. Schock. Photovoltaic materials, history, status and outlook. *Materials Science and Engineering: R: Reports*, **40**:1–46, 2003.

[19] E. A. Alsema. Energy pay-back time and co2 emissions of pv systems. *Progress in Photovoltaics: Research and Applications*, **8**:17–25, 2000.

[20] M. A. Green, K. Emery, Y. Hishikawa, W. Warta, and E. D. Dunlop. Solar cell efficiency tables (version 39). *Progress in Photovoltaics: Research and Applications*, **20**:12–20, 2012.

[21] `http://investor.firstsolar.com`, 2011.

[22] A. Barnett and A. Rothwarf. Thin-film solar cells: A unified analysis of their potential. *Electron Devices, IEEE Transactions on*, **27**:615–630, 1980.

[23] P. Jackson, D. Hariskos, E. Lotter, S. Paetel, R. Wuerz, R. Menner, W. Wischmann, and M. Powalla. New world record efficiency for Cu(In,Ga)Se_2 thin-film solar cells beyond 20%. *Progress in Photovoltaics: Research and Applications*, **19**:894–897, 2011.

[24] R. Venkatasubramanian, B. OQuinn, J. Hills, P. Sharps, M. Timmons, and J. Hutchby. 18.2% (AM1.5) efficient GaAs solar cell on optical-grade polycrystalline ge substrate. Conference Record of the Twenty Fifth IEEE Photovoltaic Specialists Conference, 1996, 31–36.

[25] `http://www.solarserver.com/solar-magazine.html`, 2012.

[26] `http://www.eia.gov/aer`, 2012.

[27] A. C. Mayer, S. R. Scully, B. E. Hardin, M. W. Rowell, and M. D. McGehee. Polymer-based solar cells. *Materials Today*, **10**:28–33, 2007.

[28] `http://www2.imec.be/be_en/press/imec-news/imecpolyerasolvayopv.html`, 2011.

[29] `http://www.technologyreview.com/energy/39763`, 2012.

[30] L. Forro, O. Chauvet, D. Emin, L. Zuppiroli, H. Berger, and F. Levy. High mobility n-type charge carriers in large single crystals of anatase (TiO_2. *Journal of Applied Physics*, **75**:633–635, 1994.

[31] K. Coakley and M. McGehee. Conjugated polymer photovoltaic cells. *Chemistry of Materials*, **16**:4533–4542, 2004.

[32] T. M. Clarke and J. R. Durrant. Charge photogeneration in organic solar cells. *Chemical Reviews*, **110**:6736–6767, 2010.

[33] B. A. Gregg, S.-G. Chen, and R. A. Cormier. Coulomb forces and doping in organic semiconductors. *Chemistry of Materials*, **16**:4586–4599, 2004.

[34] C. W. Tang. Multilayer organic photovoltaic elements. US patent 4, 164,431, 1979.

[35] C. W. Tang. Two-layer organic photovoltaic cell. *Applied Physics Letters*, **48**:183–185, 1986.

[36] S. Morita, A. A. Zakhidov, and K. Yoshino. Doping effect of buckminsterfullerene in conducting polymer: Change of absorption spectrum and quenching of luminescene. *Solid State Communications*, **82**:249–252, 1992.

[37] N. S. Sariciftci, L. Smilowitz, A. J. Heeger, and F. Wudl. Photoinduced electron transfer from a conducting polymer to buckminsterfullerene. *Science*, **258**:1474–1476, 1992.

[38] N. Sariciftci, L. Smilowitz, A. Heeger, and F. Wudl. Semiconducting polymers (as donors) and buckminsterfullerene (as acceptor): photoinduced electron transfer and heterojunction devices. *Synthetic Metals*, **59**:333–352, 1993.

[39] Y. Sun, C. J. Takacs, S. R. Cowan, J. H. Seo, X. Gong, A. Roy, and A. J. Heeger. Efficient, air-stable bulk heterojunction polymer solar cells using moox as the anode interfacial layer. *Advanced Materials*, **23**:2226–2230, 2011.

[40] F. Padinger, R. Rittberger, and N. Sariciftci. Effects of postproduction treatment on plastic solar cells. *Advanced Functional Materials*, **13**:85–88, 2003.

[41] `http://www.clevios.com`, 2011.

[42] M. Hiramoto, H. Fujiwara, and M. Yokoyama. p-i-n like behavior in three-layered organic solar cells having a co-deposited interlayer of pigments. *Journal of Applied Physics*, **72**:3781–3787, 1992.

[43] J. J. M. Halls, C. A. Walsh, N. C. Greenham, E. A. Marseglia, R. H. Friend, S. C. Moratti, and A. B. Holmes. Efficient photodiodes from interpenetrating polymer networks. *Nature*, **376**:498–500, 1995.

[44] G. Yu, J. Gao, J. C. Hummelen, F. Wudl, and A. J. Heeger. Polymer photovoltaic cells: Enhanced efficiencies via a network of internal donor-acceptor heterojunctions. *Science*, **270**:1789–1791, 1995.

[45] R. M. Beal, A. Stavrinadis, J. H. Warner, J. M. Smith, H. E. Assender, and A. A. R. Watt. The molecular structure of polymer,àífullerene composite solar cells and its influence on device performance. *Macromolecules*, **43**:2343–2348, 2010.

[46] S. E. Shaheen, C. J. Brabec, N. S. Sariciftci, F. Padinger, T. Fromherz, and J. C. Hummelen. 2.5% efficient organic plastic solar cells. *Applied Physics Letters*, **78**:841–843, 2001.

[47] T. Martens, J. D'Haen, T. Munters, Z. Beelen, L. Goris, J. Manca, M. D'Olieslaeger, D. Vanderzande, L. D. Schepper, and R. Andriessen. Disclosure of the nanostructure of mdmo-ppv:pcbm bulk hetero-junction organic solar cells by a combination of spm and tem. *Synthetic Metals*, **138**:243–247, 2003.

[48] H. Hoppe, M. Niggemann, C. Winder, J. Kraut, R. Hiesgen, A. Hinsch, D. Meissner, and N. S. Sariciftci. Nanoscale morphology of conjugated polymer/fullerene-based bulk- heterojunction solar cells. *Advanced Functional Materials*, **14**:1005–1011, 2004.

[49] D. Veldman, Ö. Opek, S. C. J. Meskers, J. Sweelssen, M. M. Koetse, S. C. Veenstra, J. M. Kroon, S. S. v. Bavel, J. Loos, and R. A. J. Janssen. Compositional and electric field dependence of the dissociation of charge transfer excitons in alternating polyfluorene copolymer/fullerene blends. *Journal of the American Chemical Society*, **130**:7721–7735, 2008.

[50] P. A. Quist, T. Martens, J. V. Manca, T. J. Savenije, and L. D. Siebbeles. Photo-induced charge separation and electron diffusion in mdmo–ppv:pcbm bulk heterojunctions. *Solar Energy Materials and Solar Cells*, **90**:362–378, 2006.

[51] M. M. Wienk, J. M. Kroon, W. J. H. Verhees, J. Knol, J. C. Hummelen, P. A. van Hal, and R. A. J. Janssen. Efficient methano[70]fullerene/MDMO-PPV bulk heterojunction photovoltaic cells. *Angewandte Chemie International Edition*, **42**:3371–3375, 2003.

[52] C. J. Brabec, S. E. Shaheen, C. Winder, N. S. Sariciftci, and P. Denk. Effect of LiF/metal electrodes on the performance of plastic solar cells. *Applied Physics Letters*, **80**:1288–1290, 2002.

[53] W. Ma, C. Yang, X. Gong, K. Lee, and A. J. Heeger. Thermally stable, efficient polymer solar cells with nanoscale control of the interpenetrating network morphology. *Advanced Functional Materials*, **15**:1617–1622, 2005.

[54] J. Peet, J. Y. Kim, N. E. Coates, W. L. Ma, D. Moses, A. J. Heeger, and G. C. Bazan. Efficiency enhancement in low-bandgap polymer solar cells by processing with alkane dithiols. *Nat Mater*, **6**:497–500, 2007.

[55] S. H. Park, A. Roy, S. Beaupre, S. Cho, N. Coates, J. S. Moon, D. Moses, M. Leclerc, K. Lee, and A. J. Heeger. Bulk heterojunction solar cells with internal quantum efficiency approaching 100%. *Nat Photon*, **3**:297–302, 2009.

[56] Y. Liang, Z. Xu, J. Xia, S.-T. Tsai, Y. Wu, G. Li, C. Ray, and L. Yu. For the bright future—bulk heterojunction polymer solar cells with power conversion efficiency of 7.4%. *Advanced Materials*, **22**:E135–E138, 2010.

[57] C. Groves, R. A. Marsh, and N. C. Greenham. Monte carlo modeling of geminate recombination in polymer-polymer photovoltaic devices. *The Journal of Chemical Physics*, **129**:114903, 2008.

[58] S. Shoaee, M. P. Eng, E. Espildora, J. L. Delgado, B. Campo, N. Martin, D. Vanderzande, and J. R. Durrant. Influence of nanoscale phase separation on geminate versus bimolecular recombination in p3ht:fullerene blend films. *Energy Environ. Sci.*, **3**:971–976, 2010.

[59] J. Y. Kim, S. H. Kim, H.-H. Lee, K. Lee, W. Ma, X. Gong, and A. J. Heeger. New architecture for high-efficiency polymer photovoltaic cells using solution-based titanium oxide as an optical spacer. *Advanced Materials*, **18**:572–576, 2006.

[60] M. S. White, D. C. Olson, S. E. Shaheen, N. Kopidakis, and D. S. Ginley. Inverted bulk-heterojunction organic photovoltaic device using a solution-derived ZnO underlayer. *Applied Physics Letters*, **89**:143517, 2006.

[61] H.-L. Yip, S. K. Hau, N. S. Baek, H. Ma, and A. K.-Y. Jen. Polymer solar cells that use self-assembled-monolayer-modified ZnO/metals as cathodes. *Advanced Materials*, **20**:2376–2382, 2008.

[62] J. Gilot, I. Barbu, M. M. Wienk, and R. A. J. Janssen. The use of ZnO as optical spacer in polymer solar cells: Theoretical and experimental study. *Applied Physics Letters*, **91**:113520, 2007.

[63] N. Blouin, A. Michaud, and M. Leclerc. A low-bandgap poly(2,7-carbazole) derivative for use in high-performance solar cells. *Advanced Materials*, **19**:2295–2300, 2007.

[64] D. Mühlbacher, M. Scharber, M. Morana, Z. Zhu, D. Waller, R. Gaudiana, and C. Brabec. High photovoltaic performance of a low-bandgap polymer. *Advanced Materials*, **18**:2884–2889, 2006.

[65] Y. Liang, Y. Wu, D. Feng, S.-T. Tsai, H.-J. Son, G. Li, and L. Yu. Development of new semiconducting polymers for high performance solar cells. *Journal of the American Chemical Society*, **131**:56–57, 2009.

[66] L. Dou, J. You, J. Yang, C.-C. Chen, Y. He, S. Murase, T. Moriarty, K. Emery, G. Li, and Y. Yang. Tandem polymer solar cells featuring a spectrally matched low-bandgap polymer. *Nat Photon*, **6**:180–185, 2012.

[67] C. J. Brabec and J. R. Durrant. Solution-processed organic solar cells. *MRS Bulletin*, **33**:670–675, 2008.

[68] C. G. Shuttle, B. O'Regan, A. M. Ballantyne, J. Nelson, D. D. C. Bradley, and J. R. Durrant. Bimolecular recombination losses in polythiophene: Fullerene solar cells. *Phys. Rev. B*, **78**:113201, 2008.

[69] J. Weickert, R. B. Dunbar, H. C. Hesse, W. Wiedemann, and L. Schmidt-Mende. Nanostructured organic and hybrid solar cells. *Advanced Materials*, **23**:1810–1828, 2011.

[70] S.-S. Sun. Design of a block copolymer solar cell. *Solar Energy Materials and Solar Cells*, **79**:257–264, 2003.

[71] M. Sommer, S. M. Lindner, and M. Thelakkat. Microphase-separated donor–acceptor diblock copolymers: Influence of homo energy levels and morphology on polymer solar cells. *Advanced Functional Materials*, **17**:1493–1500, 2007.

[72] M. Aryal, F. Buyukserin, K. Mielczarek, X.-M. Zhao, J. Gao, A. Zakhidov, and W. W. Hu. Imprinted large-scale high density polymer nanopillars for organic solar cells. Journal of Vacuum Science & Technology B, volume 26. AVS, 2008, volume 26, 2562–2566.

[73] J. S. Kim, Y. Park, D. Y. Lee, J. H. Lee, J. H. Park, J. K. Kim, and K. Cho. Poly(3-hexylthiophene) nanorods with aligned chain orientation for organic photovoltaics. *Advanced Functional Materials*, **20**:540–545, 2010.

[74] W. Zeng, K. S. L. Chong, H. Y. Low, E. L. Williams, T. L. Tam, and A. Sellinger. The use of nanoimprint lithography to improve efficiencies of bilayer organic solar cells based on p3ht and a small molecule acceptor. *Thin Solid Films*, **517**:6833–6836, 2009.

[75] W. Wiedemann, L. Sims, A. Abdellah, A. Exner, R. Meier, K. P. Musselman, J. L. MacManus-Driscoll, P. Muller-Buschbaum, G. Scarpa, P. Lugli, and L. Schmidt-Mende. Nanostructured interfaces in polymer solar cells. *Applied Physics Letters*, **96**:263109, 2010.

[76] X. He, F. Gao, G. Tu, D. Hasko, S. Hüttner, U. Steiner, N. C. Greenham, R. H. Friend, and W. T. S. Huck. Formation of nanopatterned polymer blends in photovoltaic devices. *Nano Letters*, **10**:1302–1307, 2010.

[77] X. He, F. Gao, G. Tu, D. G. Hasko, S. Hüttner, N. C. Greenham, U. Steiner, R. H. Friend, and W. T. S. Huck. Formation of well-ordered heterojunctions in polymer:pcbm photovoltaic devices. *Advanced Functional Materials*, **21**:139–146, 2011.

[78] K. M. Coakley and M. D. McGehee. Photovoltaic cells made from conjugated polymers infiltrated into mesoporous titania. *Applied Physics Letters*, **83**:3380–3382, 2003.

[79] K. Coakley, Y. Liu, M. McGehee, K. Frindell, and G. Stucky. Infiltrating semiconducting polymers into self-assembled mesoporous titania films for photovoltaic applications. *Advanced Functional Materials*, **13**:301–306, 2003.

[80] O. Jessensky, F. Muller, and U. Gosele. Self-organized formation of hexagonal pore arrays in anodic alumina. *Applied Physics Letters*, **72**:1173–1175, 1998.

[81] S. S. Williams, M. J. Hampton, V. Gowrishankar, I.-K. Ding, J. L. Templeton, E. T. Samulski, J. M. DeSimone, and M. D. McGehee. Nanostructured titania-polymer photovoltaic devices made using PFPE-based nanomolding techniques. *Chemistry of Materials*, **20**:5229–5234, 2008.

[82] K. Takanezawa, K. Hirota, Q.-S. Wei, K. Tajima, and K. Hashimoto. Efficient charge collection with ZnO nanorod array in hybrid photovoltaic devices. *The Journal of Physical Chemistry C*, **111**:7218–7223, 2007.

[83] G. K. Mor, O. K. Varghese, M. Paulose, and C. A. Grimes. Transparent highly ordered TiO_2 nanotube arrays via anodization of titanium thin films. *Advanced Functional Materials*, **15**:1291–1296, 2005.

[84] K. Shankar, G. K. Mor, H. E. Prakasam, S. Yoriya, M. Paulose, O. K. Varghese, and C. A. Grimes. Highly-ordered TiO_2 nanotube arrays up to 220 μm in length: use in water photoelectrolysis and dye-sensitized solar cells. *Nanotechnology*, **18**:065707, 2007.

[85] H. E. Prakasam, K. Shankar, M. Paulose, O. K. Varghese, and C. A. Grimes. A new benchmark for TiO_2 nanotube array growth by anodization. *The Journal of Physical Chemistry C*, **111**:7235–7241, 2007.

[86] T. R. B. Foong, Y. Shen, X. Hu, and A. Sellinger. Template-directed liquid ALD growth of TiO_2 nanotube arrays: Properties and potential in photovoltaic devices. *Advanced Functional Materials*, **20**:1390–1396, 2010.

[87] Y. Vaynzof, D. Kabra, L. Zhao, P. K. H. Ho, A. T.-S. Wee, and R. H. Friend. Improved photoinduced charge carriers separation in organic-inorganic hybrid photovoltaic devices. *Applied Physics Letters*, **97**:033309, 2010.

[88] D. C. Olson, S. E. Shaheen, M. S. White, W. J. Mitchell, M. F. A. M. van Hest, R. T. Collins, and D. S. Ginley. Band-offset engineering for enhanced open-circuit voltage in polymer–oxide hybrid solar cells. *Advanced Functional Materials*, **17**:264–269, 2007.

[89] L. E. Greene, M. Law, B. D. Yuhas, and P. Yang. ZnO-TiO_2 core-shell nanorod/P3HT solar cells. *The Journal of Physical Chemistry C*, **111**:18451–18456, 2007.

[90] K. M. Coakley, B. S. Srinivasan, J. M. Ziebarth, C. Goh, Y. Liu, and M. D. McGehee. Enhanced hole mobility in regioregular polythiophene infiltrated in straight nanopores. *Advanced Functional Materials*, **15**:1927–1932, 2005.

[91] M. Aryal, K. Trivedi, and W. W. Hu. Nano-confinement induced chain alignment in ordered P3HT nanostructures defined by nanoimprint lithography. *ACS Nano*, **3**:3085–3090, 2009.

[92] V. D. Mihailetchi, J. Wildeman, and P. W. M. Blom. Space-charge limited photocurrent. *Phys. Rev. Lett.*, **94**:126602, 2005.

[93] G. K. Mor, K. Shankar, M. Paulose, O. K. Varghese, and C. A. Grimes. High efficiency double heterojunction polymer photovoltaic cells using highly ordered TiO_2 nanotube arrays. *Applied Physics Letters*, **91**:152111, 2007.

[94] B. O'Regan and M. Grätzel. A low-cost, high-efficiency solar cell based on dye-sensitized colloidal TiO_2 films. *Nature*, **353**:737–740, 1991.

[95] G. Boschloo and A. Hagfeldt. Characteristics of the iodide/triiodide redox mediator in dye-sensitized solar cells. *Accounts of Chemical Research*, **42**:1819–1826, 2009.

[96] A. B. F. Martinson, T. W. Hamann, M. J. Pellin, and J. T. Hupp. New architectures for dye-sensitized solar cells. *Chemistry – A European Journal*, **14**:4458–4467, 2008.

[97] M. Ryan. Pgm highlights: Ruthenium complexes for dye sensitised solar cells. *Platinum Metals Review*, **53**:216–218, 2009.

[98] M. Grätzel. Solar energy conversion by dye-sensitized photovoltaic cells. *Inorganic Chemistry*, **44**:6841–6851, 2005.

[99] M. K. Nazeeruddin, F. De Angelis, S. Fantacci, A. Selloni, G. Viscardi, P. Liska, S. Ito, B. Takeru, and M. Grätzel. Combined experimental and DFT-TDDFT computational study of photoelectrochemical cell ruthenium sensitizers. *Journal of the American Chemical Society*, **127**:16835–16847, 2005.

[100] Y. Chiba, A. Islam, Y. Watanabe, R. Komiya, N. Koide, and L. Han. Dye-sensitized solar cells with conversion efficiency of 11.1%. *Japanese Journal of Applied Physics*, **45**:L638–L640, 2006.

[101] A. Yella, H.-W. Lee, H. N. Tsao, C. Yi, A. K. Chandiran, M. Nazeeruddin, E. W.-G. Diau, C.-Y. Yeh, S. M. Zakeeruddin, and M. Grätzel. Porphyrin-sensitized solar cells with cobalt (ii/iii)–based redox electrolyte exceed 12 percent efficiency. *Science*, **334**:629–634, 2011.

[102] E. Olsen, G. Hagen, and S. E. Lindquist. Dissolution of platinum in methoxy propionitrile containing LiI/I2. *Solar Energy Materials and Solar Cells*, **63**:267–273, 2000.

[103] Y. Bai, Y. Cao, J. Zhang, M. Wang, R. Li, P. Wang, S. M. Zakeeruddin, and M. Gratzel. High-performance dye-sensitized solar cells based on solvent-free electrolytes produced from eutectic melts. *Nat Mater*, **7**:626–630, 2008.

[104] S. A. Haque, E. Palomares, H. M. Upadhyaya, L. Otley, R. J. Potter, A. B. Holmes, and J. R. Durrant. Flexible dye sensitised nanocrystalline semiconductor solar cells. *Chem. Commun.*, 3008–3009, 2003.

[105] P. Wang, S. Zakeeruddin, M. Grätzel, W. Kantlehner, J. Mezger, E. Stoyanov, and O. Scherr. Novel room temperature ionic liquids of hexaalkyl substituted guanidinium salts for dye-sensitized solar cells. *Applied Physics A: Materials Science and Processing*, **79**:73–77, 2004.

[106] H. Wang, H. Li, B. Xue, Z. Wang, Q. Meng, and L. Chen. Solid-state composite electrolyte LiI/3-Hydroxypropionitrile/SiO_2 for dye-sensitized solar cells. *Journal of the American Chemical Society*, **127**:6394–6401, 2005.

[107] E. Stathatos, P. Lianos, A. Surca Vuk, and B. Orel. Optimization of a quasi-solid-state dye-sensitized photoelectrochemical solar cell employing a ureasil/sulfolane gel electrolyte. *Advanced Functional Materials*, **14**:45–48, 2004.

[108] M. Law, L. E. Greene, J. C. Johnson, R. Saykally, and P. Yang. Nanowire dye-sensitized solar cells. *Nat Mater*, **4**:455–459, 2005.

[109] D. Kuang, S. Ito, B. Wenger, C. Klein, J.-E. Moser, R. Humphry-Baker, S. M. Zakeeruddin, and M. Grätzel. High molar extinction coefficient heteroleptic ruthenium complexes for thin film dye-sensitized solar cells. *Journal of the American Chemical Society*, **128**:4146–4154, 2006.

[110] H. J. Snaith and M. Gratzel. Electron and hole transport through mesoporous TiO_2 infiltrated with spiro-meotad. *Advanced Materials*, **19**:3643–3647, 2007.

[111] N. Kopidakis, K. D. Benkstein, J. van de Lagemaat, and A. J. Frank. Transport-limited recombination of photocarriers in dye-sensitized nanocrystalline TiO_2 solar cells. *The Journal of Physical Chemistry B*, **107**:11307–11315, 2003.

[112] M. Law, L. E. Greene, A. Radenovic, T. Kuykendall, J. Liphardt, and P. Yang. ZnO-Al_2O_3 and ZnO-TiO_2 core-shell nanowire dye-sensitized solar cells. *The Journal of Physical Chemistry B*, **110**:22652–22663, 2006.

[113] E. Palomares, J. N. Clifford, S. A. Haque, T. Lutz, and J. R. Durrant. Control of charge recombination dynamics in dye sensitized solar cells by the use of conformally deposited metal oxide blocking layers. *Journal of the American Chemical Society*, **125**:475–482, 2003.

[114] J. R. Durrant, S. A. Haque, and E. Palomares. Towards optimisation of electron transfer processes in dye sensitised solar cells. *Coordination Chemistry Reviews*, **248**:1247–1257, 2004.

[115] F. Fabregat-Santiago, J. Garcia-Canadas, E. Palomares, J. N. Clifford, S. A. Haque, J. R. Durrant, G. Garcia-Belmonte, and J. Bisquert. The origin of slow electron recombination processes in dye-sensitized solar cells with alumina barrier coatings. *Journal of Applied Physics*, **96**:6903–6907, 2004.

[116] S. A. Haque, E. Palomares, B. M. Cho, A. N. M. Green, N. Hirata, D. R. Klug, and J. R. Durrant. Charge separation versus recombination in dye-sensitized nanocrystalline solar cells: the minimization of kinetic redundancy. *Journal of the American Chemical Society*, **127**:3456–3462, 2005.

[117] X. Feng, K. Shankar, M. Paulose, and C. A. Grimes. Tantalum-doped titanium dioxide nanowire arrays for dye-sensitized solar cells with high open-circuit voltage. *Angewandte Chemie International Edition*, **48**:8095–8098, 2009.

[118] A. Kumar, A. R. Madaria, and C. Zhou. Growth of aligned single-crystalline rutile TiO_2 nanowires on arbitrary substrates and their application in dye-sensitized solar cells. *The Journal of Physical Chemistry C*, **114**:7787–7792, 2010.

[119] N. Tétreault, E. Horváth, T. Moehl, J. Brillet, R. Smajda, S. Bungener, N. Cai, P. Wang, S. M. Zakeeruddin, L. Forró, A. Magrez, and M. Grätzel. High-efficiency solid-state dye-sensitized solar cells: Fast charge extraction through self-assembled 3D fibrous network of crystalline TiO_2 nanowires. *ACS Nano*, **4**:7644–7650, 2010.

[120] S. H. Ko, D. Lee, H. W. Kang, K. H. Nam, J. Y. Yeo, S. J. Hong, C. P. Grigoropoulos, and H. J. Sung. Nanoforest of hydrothermally grown hierarchical ZnO nanowires for a high efficiency dye-sensitized solar cell. *Nano Letters*, **11**:666–671, 2011.

[121] G. K. Mor, K. Shankar, M. Paulose, O. K. Varghese, and C. A. Grimes. Use of highly-ordered TiO_2 nanotube arrays in dye-sensitized solar cells. *Nano Letters*, **6**:215–218, 2006.

[122] A. B. F. Martinson, J. W. Elam, J. T. Hupp, and M. J. Pellin. ZnO nanotube based dye-sensitized solar cells. *Nano Letters*, **7**:2183–2187, 2007.

[123] K. Shankar, J. Bandara, M. Paulose, H. Wietasch, O. K. Varghese, G. K. Mor, T. J. LaTempa, M. Thelakkat, and C. A. Grimes. Highly efficient solar cells using TiO_2 nanotube arrays sensitized with a donor-antenna dye. *Nano Letters*, **8**:1654–1659, 2008.

[124] M. Nedelcu, J. Lee, E. J. W. Crossland, S. C. Warren, M. C. Orilall, S. Guldin, S. Huttner, C. Ducati, D. Eder, U. Wiesner, U. Steiner, and H. J. Snaith. Block copolymer directed synthesis of mesoporous TiO_2 for dye-sensitized solar cells. *Soft Matter*, **5**:134–139, 2009.

[125] E. J. W. Crossland, M. Kamperman, M. Nedelcu, C. Ducati, U. Wiesner, D. M. Smilgies, G. E. S. Toombes, M. A. Hillmyer, S. Ludwigs, U. Steiner, and H. J. Snaith. A bicontinuous double gyroid hybrid solar cell. *Nano Letters*, **9**:2807–2812, 2009.

[126] S. Guldin, S. Huttner, P. Tiwana, M. C. Orilall, B. Ulgut, M. Stefik, P. Docampo, M. Kolle, G. Divitini, C. Ducati, S. A. T. Redfern, H. J. Snaith, U. Wiesner, D. Eder, and U. Steiner. Improved conductivity in dye-sensitised solar cells through block-copolymer confined TiO_2 crystallisation. *Energy Environ. Sci.*, **4**:225–233, 2011.

[127] S. Guldin, P. Docampo, M. Stefik, G. Kamita, U. Wiesner, H. J. Snaith, and U. Steiner. Layer-by-layer formation of block-copolymer-derived TiO_2 for solid-state dye-sensitized solar cells. *Small*, **8**:432–440, 2012.

[128] A. B. F. Martinson, M. S. Góes, F. Fabregat-Santiago, J. Bisquert, M. J. Pellin, and J. T. Hupp. Electron transport in dye-sensitized solar cells based on ZnO nanotubes: Evidence for highly efficient charge collection and exceptionally rapid dynamics. *The Journal of Physical Chemistry A*, **113**:4015–4021, 2009.

[129] A. B. F. Martinson, J. W. Elam, J. Liu, M. J. Pellin, T. J. Marks, and J. T. Hupp. Radial electron collection in dye-sensitized solar cells. *Nano Letters*, **8**:2862–2866, 2008.

[130] M. Shvarts, O. Chosta, I. Kochnev, V. Lantratov, and V. Andreev. Radiation resistant AlGaAs/GaAs concentrator solar cells with internal Bragg reflector. *Solar Energy Materials and Solar Cells*, **68**:105 – 122, 2001.

[131] D. Johnson, I. Ballard, K. Barnham, D. Bishnell, J. Connolly, M. Lynch, T. Tibbits, N. Ekins-Daukes, M. Mazzer, R. Airey, G. Hill, and J. Roberts. Advances in Bragg stack quantum well solar cells. *Solar Energy Materials and Solar Cells*, **87**:169 – 179, 2005.

[132] P. Campbell and M. A. Green. Light trapping properties of pyramidally textured surfaces. *Journal of Applied Physics*, **62**:243–249, 1987.

[133] E. Yablonovitch and G. Cody. Intensity enhancement in textured optical sheets for solar cells. *Electron Devices, IEEE Transactions on*, **29**:300 – 305, 1982.

[134] C. Eisele, C. E. Nebel, and M. Stutzmann. Periodic light coupler gratings in amorphous thin film solar cells. *Journal of Applied Physics*, **89**:7722–7726, 2001.

[135] C. Heine and R. H. Morf. Submicrometer gratings for solar energy applications. *Appl. Opt.*, **34**:2476–2482, 1995.

[136] F. Llopis and I. Tobías. The role of rear surface in thin silicon solar cells. *Solar Energy Materials and Solar Cells*, **87**:481 – 492, 2005.

[137] R. B. Wehrspohn and J. Üpping. 3D photonic crystals for photon management in solar cells. *Journal of Optics*, **14**:024003, 2012.

[138] L. Zeng, Y. Yi, C. Hong, J. Liu, N. Feng, X. Duan, L. C. Kimerling, and B. A. Alamariu. Efficiency enhancement in si solar cells by textured photonic crystal back reflector. *Applied Physics Letters*, **89**:111111, 2006.

[139] Z. Yu, A. Raman, and S. Fan. Fundamental limit of nanophotonic light trapping in solar cells. *Proceedings of the National Academy of Sciences*, **107**:17491–17496, 2010.

[140] A. Raman, Z. Yu, and S. Fan. Dielectric nanostructures for broadband light trapping in organic solar cells. *Opt. Express*, **19**:19015–19026, 2011.

[141] S. Nishimura, N. Abrams, B. A. Lewis, L. I. Halaoui, T. E. Mallouk, K. D. Benkstein, J. van de Lagemaat, and A. J. Frank. Standing wave enhancement of red absorbance and photocurrent in dye-sensitized titanium dioxide photoelectrodes coupled to photonic crystals. *Journal of the American Chemical Society*, **125**:6306–6310, 2003.

[142] A. Mihi and H. Míguez. Origin of light-harvesting enhancement in colloidal-photonic-crystal-based dye-sensitized solar cells. *The Journal of Physical Chemistry B*, **109**:15968–15976, 2005.

[143] A. Mihi, H. Míguez, I. Rodríguez, S. Rubio, and F. Meseguer. Surface resonant modes in colloidal photonic crystals. *Phys. Rev. B*, **71**:125131, 2005.

[144] L. I. Halaoui, N. M. Abrams, and T. E. Mallouk. Increasing the conversion efficiency of dye-sensitized TiO_2 photoelectrochemical cells by coupling to photonic crystals. *The Journal of Physical Chemistry B*, **109**:6334–6342, 2005.

[145] S.-H. A. Lee, N. M. Abrams, P. G. Hoertz, G. D. Barber, L. I. Halaoui, and T. E. Mallouk. Coupling of titania inverse opals to nanocrystalline titania layers in dye-sensitized solar cells. *The Journal of Physical Chemistry B*, **112**:14415–14421, 2008.

[146] S. Guldin, S. Hüttner, M. Kolle, M. E. Welland, P. Müller-Buschbaum, R. H. Friend, U. Steiner, and N. Tétreault. Dye-sensitized solar cell based on a three-dimensional photonic crystal. *Nano Letters*, **10**:2303–2309, 2010.

[147] A. Mihi, C. Zhang, and P. V. Braun. Transfer of preformed three-dimensional photonic crystals onto dye-sensitized solar cells. *Angewandte Chemie International Edition*, **50**:5712–5715, 2011.

[148] A. Mihi, F. J. López-Alcaraz, and H. Míguez. Full spectrum enhancement of the light harvesting efficiency of dye sensitized solar cells by including colloidal photonic crystal multilayers. *Applied Physics Letters*, **88**:193110, 2006.

[149] A. Mihi, M. E. Calvo, J. A. Anta, and H. Miguez. Spectral response of opal-based dye-sensitized solar cells. *The Journal of Physical Chemistry C*, **112**:13–17, 2008.

[150] P. Bermel, C. Luo, L. Zeng, L. C. Kimerling, and J. D. Joannopoulos. Improving thin-film crystalline silicon solar cell efficiencies with photonic crystals. *Opt. Express*, **15**:16986–17000, 2007.

[151] A. Chutinan and S. John. Light trapping and absorption optimization in certain thin-film photonic crystal architectures. *Physical Review A (Atomic, Molecular, and Optical Physics)*, **78**:023825, 2008.

[152] T. Baba. Slow light in photonic crystals. *Nat Photon*, **2**:465–473, 2008.

[153] D. Duché, L. Escoubas, J.-J. Simon, P. Torchio, W. Vervisch, and F. Flory. Slow bloch modes for enhancing the absorption of light in thin films for photovoltaic cells. *Applied Physics Letters*, **92**:193310, 2008.

[154] C. L. Huisman, J. Schoonman, and A. Goossens. The application of inverse titania opals in nanostructured solar cells. *Solar Energy Materials and Solar Cells*, **85**:115–124, 2005.

[155] I. Rodriguez, P. Atienzar, F. Ramiro-Manzano, F. Meseguer, A. Corma, and H. Garcia. Photonic crystals for applications in photoelectrochemical processes: Photoelectrochemical solar cells with inverse opal topology. *Photonics and Nanostructures - Fundamentals and Applications*, **3**:148–154, 2005.

[156] C. H. Yip, Y.-M. Chiang, and C. C. Wong. Optical absorption in a finite three-dimensional photonic crystal thin film solar cell. *J. Opt. Soc. Am. B*, **27**:920–926, 2010.

[157] L. Liu, S. K. Karuturi, L. T. Su, and A. I. Y. Tok. TiO_2 inverse-opal electrode fabricated by atomic layer deposition for dye-sensitized solar cell applications. *Energy Environ. Sci.*, **4**:209–215, 2011.

[158] Y. G. Seo, K. Woo, J. Kim, H. Lee, and W. Lee. Rapid fabrication of an inverse opal TiO_2 photoelectrode for DSSC using a binary mixture of TiO_2 nanoparticles and polymer microspheres. *Advanced Functional Materials*, **21**:3094–3103, 2011.

[159] M. Peters, J. C. Goldschmidt, and B. Bläsi. Angular confinement and concentration in photovoltaic converters. *Solar Energy Materials and Solar Cells*, **94**:1393 – 1398, 2010.

[160] H. Hinterberger and R. Winston. Efficient light coupler for threshold Čerenkov counters. *Review of Scientific Instruments*, **37**:1094–1095, 1966.

[161] R. Winston. Light collection within the framework of geometrical optics. *J. Opt. Soc. Am.*, **60**:245–247, 1970.

[162] A. Garcia-Botella, A. A. Fernandez-Balbuena, and E. Bernabeu. Elliptical concentrators. *Appl. Opt.*, **45**:7622–7627, 2006.

[163] J. Yoon, A. J. Baca, S.-I. Park, P. Elvikis, J. B. Geddes, L. Li, R. H. Kim, J. Xiao, S. Wang, T.-H. Kim, M. J. Motala, B. Y. Ahn, E. B. Duoss, J. A. Lewis, R. G. Nuzzo, P. M. Ferreira, Y. Huang, A. Rockett, and J. A. Rogers. Ultrathin silicon solar microcells for semitransparent, mechanically flexible and microconcentrator module designs. *Nat Mater*, **7**:907–915, 2008.

[164] J. Tseng, Y. Chen, C. Pan, T. Wu, and M. Chung. Application of optical film with micro-lens array on a solar concentrator. *Solar Energy*, **85**:2167 – 2178, 2011.

[165] A. Lingley, B. Otis, T. Shen, and B. Parviz. A contact lens with integrated micro solar cells. *Microsystem Technologies*, **18**:453–458, 2012.

[166] M. Peters, J. C. Goldschmidt, and B. Bläsi. Efficiency limit and example of a photonic solar cell. *Journal of Applied Physics*, **110**:043104, 2011.

[167] S. Fahr, C. Ulbrich, T. Kirchartz, U. Rau, C. Rockstuhl, and F. Lederer. Rugate filter for light-trapping in solar cells. *Opt. Express*, **16**:9332–9343, 2008.

[168] M. Peters, J. C. Goldschmidt, T. Kirchartz, and B. Bläsi. The photonic light trap—improved light trapping in solar cells by angularly selective filters. *Solar Energy Materials and Solar Cells*, **93**:1721 – 1727, 2009.

[169] J. Upping, A. Bielawny, P. T. Miclea, and R. B. Wehrspohn. 3D photonic crystals for ultra-light trapping in solar cells. Photonics for Solar Energy Systems II, volume 7002, edited by A. Gombert. SPIE, 2008, volume 7002, 70020W.

[170] C. Ulbrich, S. Fahr, J. Üpping, M. Peters, T. Kirchartz, C. Rockstuhl, R. Wehrspohn, A. Gombert, F. Lederer, and U. Rau. Directional selectivity and ultra-light-trapping in solar cells. *Physica Status Solidi A*, **205**:2831–2843, 2008.

[171] V. Berger, O. Gauthier-Lafaye, and E. Costard. Fabrication of a 2D photonic bandgap by a holographic method. *Electronics Letters*, **33**:425–426, 1997.

[172] T. F. Krauss and R. M. D. L. Rue. Photonic crystals in the optical regime – past, present and future. *Progress in Quantum Electronics*, **23**:51–96, 1999.

[173] M. Campbell, D. N. Sharp, M. T. Harrison, R. G. Denning, and A. J. Turberfield. Fabrication of photonic crystals for the visible spectrum by holographic lithography. *Nature*, **404**:53–56, 2000.

[174] S. Shoji and S. Kawata. Photofabrication of three-dimensional photonic crystals by multibeam laser interference into a photopolymerizable resin. *Applied Physics Letters*, **76**:2668–2670, 2000.

[175] C. T. Chan, K. M. Ho, and C. M. Soukoulis. Photonic band gaps in experimentally realizable periodic dielectric structures. *EPL (Europhysics Letters)*, **16**:563, 1991.

[176] C. Chan, S. Datta, K. Ho, and C. Soukoulis. $A7$ structure: A family of photonic crystals. *Phys. Rev. B*, **50**:1988–1991, 1994.

[177] D. Sharp. The fabrication and assessment of three dimensional photonic crystals. Ph.D. thesis, Clarendon Laboratory, Department of Physics, University of Oxford, 2001.

[178] D. C. Meisel, M. Diem, M. Deubel, F. Pérez-Willard, S. Linden, D. Gerthsen, K. Busch, and M. Wegener. Shrinkage precompensation of holographic three-dimensional photonic-crystal templates. *Advanced Materials*, **18**:2964–2968, 2006.

[179] D. Sharp, M. Campbell, E. Dedman, M. Harrison, R. Denning, and A. Turberfield. Photonic crystals for the visible spectrum by holographic lithography. *Optical and Quantum Electronics*, **34**:3–12, 2002.

[180] S. Yang, M. Megens, J. Aizenberg, P. Wiltzius, P. M. Chaikin, and W. B. Russel. Creating periodic three-dimensional structures by multibeam interference of visible laser. *Chemistry of Materials*, **14**:2831–2833, 2002.

[181] Y. V. Miklyaev, D. C. Meisel, A. Blanco, G. von Freymann, K. Busch, W. Koch, C. Enkrich, M. Deubel, and M. Wegener. Three-dimensional face-centered-cubic photonic crystal templates by laser holography: fabrication, optical characterization, and band-structure calculations. *Applied Physics Letters*, **82**:1284–1286, 2003.

[182] I. Divliansky, T. S. Mayer, K. S. Holliday, and V. H. Crespi. Fabrication of three-dimensional polymer photonic crystal structures using single diffraction element interference lithography. *Applied Physics Letters*, **82**:1667–1669, 2003.

[183] V. Tondiglia, L. Natarajan, R. Sutherland, D. Tomlin, and T. Bunning. Holographic formation of electro-optical polymer–liquid crystal photonic crystals. *Advanced Materials*, **14**:187–191, 2002.

[184] C. K. Ullal, M. Maldovan, E. L. Thomas, G. Chen, Y.-J. Han, and S. Yang. Photonic crystals through holographic lithography: Simple cubic, diamond-like, and gyroid-like structures. *Applied Physics Letters*, **84**:5434–5436, 2004.

[185] R. G. Denning, C. F. Blanford, H. Urban, H. Bharaj, D. N. Sharp, and A. J. Turberfield. The control of shrinkage and thermal instability in SU-8 photoresists for holographic lithography. *Advanced Functional Materials*, **21**:1593–1601, 2011.

[186] J. Shaw, J. Gelorme, N. LaBianca, W. Conley, and S. Holmes. Negative photoresists for optical lithography. *IBM Journal of Research and Development*, **41**:81–94, 1997.

[187] Electron imaging with scanning electron microscope JEOL JSM-840F, field emission gun, acceleration voltage of 3 kV, electron beam current of 20 pA, secondary electron detection at 15 mm working distance, DISS 5 digital image acquisition, specimen prepared with 3 nm thick Pt layers by using Cressington Turbo Sputter Coater 208 HR. EM Facility Begbroke, Materials Department, Oxford, 2011.

[188] M. Gu and X. S. Gan. Fresnel diffraction by circular and serrated apertures illuminated with an ultrashort pulsed-laser beam. *J. Opt. Soc. Am. A*, **13**:771–778, 1996.

[189] H. Bharaj. Recorded laser pulse profile with a CCD camera. Clarendon Laboratory, Oxford, 2006.

[190] C. C. Riccardi, H. E. Adabbo, and R. J. J. Williams. Curing reaction of epoxy resins with diamines. *Journal of Applied Polymer Science*, **29**:2481–2492, 1984.

[191] J. C. Patterson-Jones and D. A. Smith. The thermal degradation of an amine-cured epoxide resin at temperatures between 200 °C and 310 °C. *Journal of Applied Polymer Science*, **12**:1601–1620, 1968.

[192] H. Kim. Atomic layer deposition of metal and nitride thin films: Current research efforts and applications for semiconductor device processing. *Journal of Vacuum Science and Technology B*, **21**:2231–2261, 2003.

[193] M. Ritala, M. Leskelä, J.-P. Dekker, C. Mutsaers, P. J. Soininen, and J. Skarp. Perfectly conformal TiN and Al_2O_3 films deposited by atomic layer deposition. *Chemical Vapor Deposition*, **5**:7–9, 1999.

[194] D. Hausmann, J. Becker, S. Wang, and R. G. Gordon. Rapid vapor deposition of highly conformal silica nanolaminates. *Science*, **298**:402–406, 2002.

[195] C. Brinker and G. Scherer. Sol-gel science: the physics and chemistry of sol-gel processing. Academic Press, 1990.

[196] G. Mallory, J. Hajdu, A. Electroplaters, and S. F. Society. Electroless plating: fundamentals and applications. Noyes Publications/William Andrew Publishing, LLC, 1990.

[197] F. Lowenheim and A. E. Society. Electroplating. McGraw-Hill, 1978.

[198] K. Reichelt and X. Jiang. The preparation of thin films by physical vapour deposition methods. *Thin Solid Films*, **191**:91–126, 1990.

[199] A. Cho and J. Arthur. Molecular beam epitaxy. *Progress in Solid State Chemistry*, **10, Part 3**:157–191, 1975.

[200] H. Pierson. Handbook of chemical vapor depostion (CVD): principles, technology, and applications. Materials science, process technology and semiconductors. Noyes Publications/William Andrew Pub., 1999.

[201] J. Park and T. Sudarshan. Chemical vapor deposition. Surface engineering series. ASM International, 2001.

[202] D. Smith. Thin-film deposition: principles and practice. McGraw-Hill, 1995.

[203] D. T. Read and A. A. Volinsky. Thin films for microelectronics and photonics: Physics, mechanics, characterization, and reliability. Micro- and Opto-Electronic Materials and

Structures: Physics, Mechanics, Design, Reliability, Packaging, edited by E. Suhir, Y. C. Lee, and C. P. Wong, Springer US, 135–180, 2007.

[204] R. L. Puurunen. Surface chemistry of atomic layer deposition: A case study for the trimethylaluminum/water process. *Journal of Applied Physics*, **97**:121301, 2005.

[205] R. Gordon, D. Hausmann, E. Kim, and J. Shepard. A kinetic model for step coverage by atomic layer deposition in narrow holes or trenches. *Chemical Vapor Deposition*, **9**:73–78, 2003.

[206] G. M. Sundaram, E. W. Deguns, R. Bhatia, M. J. Dalberth, M. J. Sowa, and J. S. Becker. Thin films for 3D: ALD for non-planar topographies. *Solid State Technology*, **52**:12+, 2009.

[207] S. O. Kucheyev, J. Biener, T. F. Baumann, Y. M. Wang, A. V. Hamza, Z. Li, D. K. Lee, and R. G. Gordon. Mechanisms of atomic layer deposition on substrates with ultrahigh aspect ratios. *Langmuir*, **24**:943–948, 2008.

[208] S. M. George. Atomic layer deposition: An overview. *Chemical Reviews*, **110**:111–131, 2010.

[209] A. M. Shevjakov, G. N. Kuznetsova, and V. B. Aleskovskii. Chemistry of high-temperature materials. Proceedings of the Second USSR Conference on High-Temperature Chemistry of Oxides. Leningrad, USSR, 1965 (Nauka, Leningrad, USSR, 1967), in Russian, 149–155.

[210] A. Malygin. The molecular layering nanotechnology: Basis and application. *Journal of Industrial and Engineering Chemistry*, **12**:1–11, 2006.

[211] T. Suntola and J. Antson. Finnish patent no. 52395 and us patent no. 4058430, 1974 and 1977 respectively.

[212] T. Suntola and J. Hyvarinen. Atomic layer epitaxy. *Annual Review of Materials Science*, **15**:177–195, 1985.

[213] Y. Nicolau. Solution deposition of thin solid compound films by a successive ionic-layer adsorption and reaction process. *Applications of Surface Science*, **22-23, Part 2**:1061–1074, 1985.

[214] S. Lindroos, T. Kanniainen, and M. Leskelä. Growth of zns thin films by liquid-phase atomic layer epitaxy (lpale). *Applied Surface Science*, **75**:70–74, 1994.

[215] B. W. Gregory, D. W. Suggs, and J. L. Stickney. Conditions for the deposition of cdte by electrochemical atomic layer epitaxy. *Journal of The Electrochemical Society*, **138**:1279–1284, 1991.

[216] T. L. Wade, L. C. Ward, C. B. Maddox, U. Happek, and J. L. Stickney. Electrodeposition of inas. *Electrochemical and Solid-State Letters*, **2**:616–618, 1999.

[217] J. S. King. Fabrication of Opal-Based Photonic Crystals Using Atomic Layer Deposition. Ph.D. thesis, Georgia Institute of Technology, 2004.

[218] A. Ott, J. Klaus, J. Johnson, and S. George. Al_2O_3 thin film growth on Si(100) using binary reaction sequence chemistry. *Thin Solid Films*, **292**:135–144, 1997.

[219] W. Besling, E. Young, T. Conard, C. Zhao, R. Carter, W. Vandervorst, M. Caymax, S. D. Gendt, M. Heyns, J. Maes, M. Tuominen, and S. Haukka. Characterisation of ALCVD Al_2O_3-ZrO_2 nanolaminates, link between electrical and structural properties. *Journal of Non-Crystalline Solids*, **303**:123–133, 2002.

[220] E. Gusev, C. C. Jr., M. Copel, C. D'Emic, and M. Gribelyuk. Ultrathin HfO_2 films grown on silicon by atomic layer deposition for advanced gate dielectrics applications. *Microelectronic Engineering*, **69**:145–151, 2003.

[221] D. B. Farmer and R. G. Gordon. ALD of high-κ dielectrics on suspended functionalized SWNTs. *Electrochemical and Solid-State Letters*, **8**:G89–G91, 2005.

[222] A. S. Cavanagh, C. A. Wilson, A. W. Weimer, and S. M. George. Atomic layer deposition on gram quantities of multi-walled carbon nanotubes. *Nanotechnology*, **20**:255602, 2009.

[223] C. Argile and G. Rhead. Adsorbed layer and thin film growth modes monitored by Auger electron spectroscopy. *Surface Science Reports*, **10**:277–356, 1989.

[224] M. Copel, M. Gribelyuk, and E. Gusev. Structure and stability of ultrathin zirconium oxide layers on Si(001). *Applied Physics Letters*, **76**:436–438, 2000.

[225] C. A. Wilson, R. K. Grubbs, and S. M. George. Nucleation and growth during Al_2O_3 atomic layer deposition on polymers. *Chemistry of Materials*, **17**:5625–5634, 2005.

[226] D. Bradley. New metallo-organic precursors for surface processing. *Applied Surface Science*, **46**:1–4, 1990.

[227] J. Dendooven, D. Deduytsche, J. Musschoot, R. L. Vanmeirhaeghe, and C. Detavernier. Conformality of Al_2O_3 and AlN deposited by plasma-enhanced atomic layer deposition. *Journal of The Electrochemical Society*, **157**:G111–G116, 2010.

[228] S. B. S. Heil, P. Kudlacek, E. Langereis, R. Engeln, M. C. M. van de Sanden, and W. M. M. Kessels. In situ reaction mechanism studies of plasma-assisted atomic layer deposition of al2o3. *Applied Physics Letters*, **89**:131505, 2006.

[229] J. W. Lim and S. J. Yun. Electrical properties of alumina films by plasma-enhanced atomic layer deposition. *Electrochemical and Solid-State Letters*, **7**:F45–F48, 2004.

[230] S. M. George, B. Yoon, and A. A. Dameron. Surface chemistry for molecular layer deposition of organic and hybrid organic‚àíinorganic polymers. *Accounts of Chemical Research*, **42**:498–508, 2009.

[231] M. E. Alf, A. Asatekin, M. C. Barr, S. H. Baxamusa, H. Chelawat, G. Ozaydin-Ince, C. D. Petruczok, R. Sreenivasan, W. E. Tenhaeff, N. J. Trujillo, S. Vaddiraju, J. Xu, and K. K. Gleason. Chemical vapor deposition of conformal, functional, and responsive polymer films. *Advanced Materials*, **22**:1993–2027, 2010.

[232] T. Yoshimura, R. Ebihara, and A. Oshima. Polymer wires with quantum dots grown by molecular layer deposition of three source molecules for sensitized photovoltaics. *Journal of Vacuum Science and Technology A*, **29**:051510, 2011.

[233] A. Mohammadi, M.-A. Hasan, B. Liedberg, I. Lundström, and W. Salaneck. Chemical vapour deposition (CVD) of conducting polymers: Polypyrrole. *Synthetic Metals*, **14**:189–197, 1986.

[234] A. Asatekin, M. C. Barr, S. H. Baxamusa, K. K. Lau, W. Tenhaeff, J. Xu, and K. K. Gleason. Designing polymer surfaces via vapor deposition. *Materials Today*, **13**:26–33, 2010.

[235] S. G. Im and K. K. Gleason. Systematic control of the electrical conductivity of poly(3,4-ethylenedioxythiophene) via oxidative chemical vapor deposition. *Macromolecules*, **40**:6552–6556, 2007.

[236] S. G. Im, K. K. Gleason, and E. A. Olivetti. Doping level and work function control in oxidative chemical vapor deposited poly (3,4-ethylenedioxythiophene). *Applied Physics Letters*, **90**:152112, 2007.

[237] M. Ritala, M. Leskelä, E. Nykänen, P. Soininen, and L. Niinistö. Growth of titanium dioxide thin films by atomic layer epitaxy. *Thin Solid Films*, **225**:288–295, 1993.

[238] J. Aarik, A. Aidla, T. Uustare, and V. Sammelselg. Morphology and structure of TiO_2 thin films grown by atomic layer deposition. *Journal of Crystal Growth*, **148**:268–275, 1995.

[239] J. Aarik, A. Aidla, V. Sammelselg, H. Siimon, and T. Uustare. Control of thin film structure by reactant pressure in atomic layer deposition of TiO_2. *Journal of Crystal Growth*, **169**:496–502, 1996.

[240] E. B. Yousfi, B. Weinberger, F. Donsanti, P. Cowache, and D. Lincot. Atomic layer deposition of zinc oxide and indium sulfide layers for cu(in,ga)se2 thin-film solar cells. *Thin Solid Films*, **387**:29–32, 2001.

[241] J. Lim and C. Lee. Effects of substrate temperature on the microstructure and photoluminescence properties of ZnO thin films prepared by atomic layer deposition. *Thin Solid Films*, **515**:3335–3338, 2007.

[242] C. H. Liu and R. P. H. Chang. Theoretical and experimental study of impact of electric field on the atomic layer epitaxy of ZnO on Al_2O_3 surface. *Journal of Chemical Physics*, **116**:8139–8143, 2002.

[243] V. Lujala, J. Skarp, M. Tammenmaa, and T. Suntola. Atomic layer epitaxy growth of doped zinc oxide thin films from organometals. *Applied Surface Science*, **82-83**:34–40, 1994.

[244] J. Becker, E. Kim, and R. Gordon. Atomic layer deposition of insulating hafnium and zirconium nitrides. *Chemistry of Materials*, **16**:3497–3501, 2004.

[245] L. H. Dubois, B. R. Zegarski, and G. S. Girolami. Infrared studies of the surface and gas phase reactions leading to the growth of titanium nitride thin films from tetrakis(dimethylamido)titanium and ammonia. *Journal of The Electrochemical Society*, **139**:3603–3609, 1992.

[246] J. A. Prybyla, C. ,. Chiang, and L. H. Dubois. Investigations of the growth of TiN thin films from $Ti(NMe_2)_4$ and ammonia. *Journal of The Electrochemical Society*, **140**:2695–2702, 1993.

[247] J. Elam, M. Schuisky, J. Ferguson, and S. George. Surface chemistry and film growth during TiN atomic layer deposition using TDMAT and NH3. *Thin Solid Films*, **436**:145–156, 2003.

[248] Y. Xu and C. B. Musgrave. Atomic layer deposition of hafnium nitrides using ammonia and alkylamide precursors. *Chemical Physics Letters*, **407**:272 – 275, 2005.

[249] J. C. F. Rodríguez-Reyes and A. V. Teplyakov. Surface transamination reaction for tetrakis(dimethylamido)titanium with NH_X-terminated Si(100) surfaces. *The Journal of Physical Chemistry C*, **111**:16498–16505, 2007.

[250] B.-C. Kan, J.-H. Boo, I. Lee, and F. Zaera. Thermal chemistry of tetrakis(ethylmethylamido)titanium on Si(100) surfaces. *The Journal of Physical Chemistry A*, **113**:3946–3954, 2009.

[251] R. G. Denning. Organized all parts and planned the layout of the ALD manifold in analogy to the design from ref. [244]. he installed the solenoid drivers and modified their power supply. Inorganic Chemistry, Department of Chemistry, Oxford, 2011.

[252] H. Bharaj. Produced the software that enabled remote control of the ALD apparatus and created the electronic interface between computer and solenoid drivers. Clarendon Laboratory, 2011.

[253] P. W. Atkins and J. De Paula. Atkins' Physical chemistry. Oxford University Press, New York, 2006.

[254] B. Cordero, V. Gomez, A. E. Platero-Prats, M. Reves, J. Echeverria, E. Cremades, F. Barragan, and S. Alvarez. Covalent radii revisited. *Dalton Transactions*, 2832–2838, 2008.

[255] R. P. Netterfield, P. J. Martin, and D. R. McKenzie. Properties of ZrN_x prepared by ion-assisted deposition. *Journal of Materials Science Letters*, **9**:972–974, 1990.

[256] Q. H. Li, D. Zhu, W. Liu, Y. Liu, and X. C. Ma. Optical properties of Al-doped ZnO thin films by ellipsometry. *Applied Surface Science*, **254**:2922–2926, 2008.

[257] R. Jacobs. Performed ellipsometry measurements and analysis. Surface Analysis Facility, Department of Chemistry, Oxford, 2011.

[258] R. G. Denning. Performed infrared spectroscopy measurements on the ammonia precursor. Inorganic Chemistry, Department of Chemistry, Oxford, 2011.

[259] R. Gunning. Performed and analyzed X-ray diffraction measurements. Clarendon Laboratory, Oxford, 2011.

[260] S. H. Yoon. Growth and characterization of zinc oxide and PZT films for micromachined acoustic wave devices. Ph.D. thesis, Auburn University, 2009.

[261] J. M. Jensen, A. B. Oelkers, R. Toivola, D. C. Johnson, J. W. Elam, and S. M. George. X-ray reflectivity characterization of ZnO/Al_2O_3 multilayers prepared by atomic layer deposition. *Chemistry of Materials*, **14**:2276–2282, 2002.

[262] S.-H. K. Park, C.-S. Hwang, H. Y. Jeong, H. Y. Chu, and K. I. Cho. Transparent ZnO-TFT arrays fabricated by atomic layer deposition. *Electrochemical and Solid-State Letters*, **11**:H10–H14, 2008.

[263] J.-S. Na, G. Scarel, and G. N. Parsons. In situ analysis of dopant incorporation, activation, and film growth during thin film ZnO and ZnO:Al atomic layer deposition. *The Journal of Physical Chemistry C*, **114**:383–388, 2010.

[264] K. Ellmer and G. Vollweiler. Electrical transport parameters of heavily-doped zinc oxide and zinc magnesium oxide single and multilayer films heteroepitaxially grown on oxide single crystals. *Thin Solid Films*, **496**:104–111, 2006.

[265] T. Koida, H. Fujiwara, and M. Kondo. Structural and electrical properties of hydrogen-doped films fabricated by solid-phase crystallization. *Journal of Non-Crystalline Solids*, **354**:2805–2808, 2008.

[266] S. Calnan and A. Tiwari. High mobility transparent conducting oxides for thin film solar cells. *Thin Solid Films*, **518**:1839–1849, 2010.

[267] H. J. Snaith. Provided access to his research facilities that allowed fabrication and characterization of solar cell devices. Clarendon Laboratory, University of Oxford, 2011.

[268] P. Docampo. Established the apparatus and recording LabVIEW program for power converion efficiency and fill factor measurements of solar cell devices. Clarendon Laboratory, University of Oxford, 2011.

[269] G. Schlichthörl, S. Y. Huang, J. Sprague, and A. J. Frank. Band edge movement and recombination kinetics in dye-sensitized nanocrystalline TiO_2 solar cells: A study by intensity modulated photovoltage spectroscopy. *The Journal of Physical Chemistry B*, **101**:8141–8155, 1997.

[270] N. Kopidakis, E. A. Schiff, N.-G. Park, J. van de Lagemaat, and A. J. Frank. Ambipolar diffusion of photocarriers in electrolyte-filled, nanoporous TiO_2. *The Journal of Physical Chemistry B*, **104**:3930–3936, 2000.

[271] P. Docampo. Established the apparatus and recording LabVIEW program for photocarrier transport measurments of solar cell devices. Clarendon Laboratory, University of Oxford, 2011.

[272] P. Docampo, S. Guldin, M. Stefik, P. Tiwana, M. C. Orilall, S. Hüttner, H. Sai, U. Wiesner, U. Steiner, and H. J. Snaith. Control of solid-state dye-sensitized solar cell performance by block-copolymer-directed TiO_2 synthesis. *Advanced Functional Materials*, **20**:1787–1796, 2010.

[273] A. J. Frank, N. Kopidakis, and J. van de Lagemaat. Electrons in nanostructured TiO_2 solar cells: transport, recombination and photovoltaic properties. *Coordination Chemistry Reviews*, **248**:1165–1179, 2004.

[274] J. van de Lagemaat and A. J. Frank. Nonthermalized electron transport in dye-sensitized nanocrystalline TiO_2 films: Transient photocurrent and random-walk modeling studies. *The Journal of Physical Chemistry B*, **105**:11194–11205, 2001.

[275] M. Skompska. Hybrid conjugated polymer/semiconductor photovoltaic cells. *Synthetic Metals*, **160**:1–15, 2010.

[276] M. Brown and J. Ball. Established the apparatus and LabVIEW program for spectral response measurements of solar cell devices. Clarendon Laboratory, University of Oxford, 2011.

[277] A. Hagfeldt and M. Grätzel. Molecular photovoltaics. *Accounts of Chemical Research*, **33**:269–277, 2000.

[278] K. Suresh. Volume of a surface triangulation: Given a surface triangulation, compute the volume enclosed using divergence theorem, File ID #26982. File Exchange at MathWorks MATLAB-Central, 2010.

[279] H. J. Snaith. Measurements show that the roughness factor of a 1μm thick nano-particulate dye-sensitized solar cell device is $\approx$100. Clarendon Laboratory, 2011.

[280] P. Docampo. According to communication with Pablo, the porosity of nano-particulate films was determined in Ecole Polytechnique Federale de Lausanne and University of Cambridge. Clarendon Laboratory, University of Oxford, 2011.

[281] H. J. Snaith. Crystallite size of 20 nm in nanocrystalline TiO_2 films determined by X-ray diffraction measurments. Clarendon Laboratory, University of Oxford, 2011.

[282] N. Hirata, J.-J. Lagref, E. J. Palomares, J. R. Durrant, M. K. Nazeeruddin, M. Gratzel, and D. Di Censo. Supramolecular control of charge-transfer dynamics on dye-sensitized nanocrystalline TiO_2 films. *Chemistry – A European Journal*, **10**:595–602, 2004.

[283] H. M. Nguyen, D. N. Nguyen, and N. Kim. Improved performance of dye-sensitized solar cells by tuning the properties of ruthenium complexes containing conjugated bipyridine ligands. *Advances in Natural Sciences: Nanoscience and Nanotechnology*, **1**:025001, 2010.

[284] S. Ito, P. Chen, P. Comte, M. K. Nazeeruddin, P. Liska, P. Péchy, and M. Grätzel. Fabrication of screen-printing pastes from TiO_2 powders for dye-sensitised solar cells. *Progress in Photovoltaics: Research and Applications*, **15**:603–612, 2007.

[285] A. A. R. Watt. Generously provided the PEDOT:PSS dispersions Clevios P-VP-AI-4083 and Clevios PH-500. Department of Materials, University of Oxford, 2011.

[286] A. Luque and S. Hegedus. Handbook of Photovoltaic Science and Engineering. John Wiley & Sons Ltd., 2011.

[287] Z. Yang, S. Gao, W. Li, V. Vlasko-Vlasov, U. Welp, W.-K. Kwok, and T. Xu. Three-dimensional photonic crystal fluorinated tin oxide (FTO) electrodes: Synthesis and optical and electrical properties. *ACS Applied Materials & Interfaces*, **3**:1101–1108, 2011.

[288] M. A. Aouaj, R. Diaz, A. Belayachi, F. Rueda, and M. Abd-Lefdil. Comparative study of ITO and FTO thin films grown by spray pyrolysis. *Materials Research Bulletin*, **44**:1458 – 1461, 2009.

[289] J. Heo, A. S. Hock, and R. G. Gordon. Low temperature atomic layer deposition of tin oxide. *Chemistry of Materials*, **22**:4964–4973, 2010.

[290] G. E. Johnson, Q. Hu, and J. Laskin. Soft landing of complex molecules on surfaces. *Annual Review of Analytical Chemistry*, **4**:83–104, 2011.

[291] P. Kovacik, G. Sforazzini, A. G. Cook, S. M. Willis, P. S. Grant, H. E. Assender, and A. A. R. Watt. Vacuum-deposited planar heterojunction polymer solar cells. *ACS Applied Materials & Interfaces*, **3**:11–15, 2011.

[292] J. P. Lock, S. G. Im, and K. K. Gleason. Oxidative chemical vapor deposition of electrically conducting poly(3,4-ethylenedioxythiophene) films. *Macromolecules*, **39**:5326–5329, 2006.

[293] L. J. van der Pauw. A method of measuring the resistivity and hall coefficient on lamellae of arbitrary shape. *Philips Technical Review*, **20**:220–224, 1958.